Dynamics of Vortices on the Solar Photosphere

Yasir Aljohani

Supervisors:
Dr. Istvan Ballai
Dr. Gary Verth
Prof. Viktor Fedun

The University Of Sheffield.

University of Sheffield

School of Mathematics and Statistics

A thesis submitted in partial fulfilment of the requirements for the degree of

Doctor of Philosophy

May, 2022

I would like to dedicate my thesis to my parents for their continuous encouragement and support.

Acknowledgements

To begin, I extend my heartfelt gratitude to God. I would like to convey my profound appreciation and gratitude to my supervisors, Drs. Istvan Ballai, Gary Verth and Prof. Viktor Fedun for their encouragement and direction during my Ph.D. I overcame many obstacles and successfully accomplished this research with their scientific, unique, and insightful direction; it was an enormous pleasure and privilege for me to work under the supervision of Drs. Istvan Ballai, Gary Verth and Prof. Viktor Fedun.

I would like to express my gratitude to the several individuals who provided support and guidance in order for this thesis to be successfully completed.

I want to express my deep gratitude to my advisor, Dr. Ashley Willis, for his encouragement, continued support, and academic pieces of advice that he has provided. It was his encouragement and advice supportive of accomplishing this work. Additionally, I would like to express my gratitude to Dr. Koji Ohkitani, my previous advisor, for the academic advice he provided me throughout my first and second years.

I also like to thank Dr. Suzana S. A. Silva for sharing her expertise on vortex identification with me.

I would also like to extend my deepest gratitude to Dr. Sergiy Shelyag, for providing me with the necessary data for part of this work (Chapter 3).

From the bottom of my heart, I thank my parents, who have been instrumental in encouraging me to complete my Ph.D. and have always believed in me that I can accomplish this work. I thank them for all the love, giving, and support over the past years. Without you, none of this would have been possible.

I want to thank The University Sheffield for all support and funding for AGU meeting. I want to thank the Saudi Government, , the Royal Embassy, the Saudi Cultural Bureau, and the Ministry of Higher Education for my scholarship and for supporting my study.

Declaration of Authorship

I hereby declare that, except where clear reference is made to the work of others, the contents of this dissertation are original and have not, in whole or in part, been submitted to this or any other university for consideration for any other degree or qualification. This dissertation is my own work and contains nothing which is the outcome of work done in collaboration with others, except as specified in the text and Acknowledgements.

Yasir Aljohani
March 2022

Abstract

The majority of studies on multi-scale vortex motions employ a two-dimensional geometry by using a variety of observational and numerical data. This approach limits the understanding of the nature of physical processes responsible for vortex dynamics. Here we develop a new methodology to extract essential information from the boundary surface of vortex tubes. 3D high-resolution magnetoconvection MURaM numerical data has been used to analyse photospheric intergranular velocity vortices. The Lagrangian Averaged Vorticity Deviation (LAVD) technique was applied to define the centers of vortex structures and their boundary surfaces based on the advection of fluid elements. These surfaces were mapped onto a constructed envelope grid that allows the study of the key plasma parameters as functions of space and time. Physical quantities that help in the understanding of plasma dynamics were also identified. Our results suggest that, while density and pressure have a rather global behaviour, the other physical quantities undergo local changes, with their magnitude and orientation changing in space and time. At the surface, the mixing in the horizontal direction is not efficient, leading to appearance of localized regions with higher/lower temperatures. In addition, the analysis of the MHD Poynting flux confirms that the majority of the energy is directed in the horizontal direction. Our findings also indicate that the pressure and magnetic forces that drive the dynamics of the plasma on vortex surfaces are unbalanced and therefore the vortices do not rotate as a rigid body.

Next, we investigate the signatures of waves that might propagate via vortices. The objective of this study is to construct basic rotating magnetic flux tubes and then to analyse the existence and signature of local and global waves travelling through solar vortex tubes. The Proper Orthogonal Decomposition (POD) technique was used to analyse the wave morphology.

List of Publications

This Thesis is based on the following publications:

- New approach for analysing dynamical processes on the surface of photospheric vortex tubes (Aljohani et al., 2022) published in The Astrophysical Journal.

- Waves on vortex surfaces, Yasir Aljohani, Viktor Fedun, Istvan Ballai, and Gary Verth (In preparation).

Contents

List of Figures

List of Tables

CHAPTER 1
Introduction

1.1 The Sun

The study of the Sun is crucial for many reasons, paramount being that the Sun is the closest star that can be studied in great detail and because of its role in maintaining and supporting life on Earth. Thanks to the high-resolution of observations of the last few decades provided by a myriad of space satellites and ground-based telescopes such as SoHO, TRACE, HiNODE, STEREO, SDO, BBSO, SST, DKIST, etc., the solar physics has entered in a new golden age. The new results are revolutionising the way we understand and model the structure and evolution of the Sun. Therefore, our Sun presents an unique opportunity to investigate the stellar properties in detail.

Another crucial feature of the Sun is that its activity can have a significant effect on our highly technological society. The solar atmosphere's outermost layer is constantly expanding and transporting magnetic fields and energetic particles. Thereby, storm conditions can be transported from the sun to Earth, affecting ground-based technological devices, telecommunication satellites. Thus, it is critical to understand the main mechanisms driving energetic solar activity events in order to prevent hazardous effects in our technology. In other words, the study of the solar atmosphere enables a deeper understanding of the mechanism that influences space weather events and the conditions of near-Earth space.

Studying the Sun also provides valuable information on physical mechanisms that are able to sustain a million Kelvin upper atmosphere in sun-like stars. The current Thesis focuses on the study of dynamical processes as vortices and waves which are believed to play an essential role in heating up the solar atmosphere. The beginning of this Chapter is devoted to a detailed overview of the Sun, its structure and magnetic features. Finally, a brief introduction into vortices in the solar plasma is presented.

In the present section, the bulk of the material has been derived from Priest (2014), and it should be used as a source unless otherwise specified.

1.2 The Structure of the Sun and its Physical Properties

The Sun is very inhomogeneous and has a complex composition. For the most part, the Sun is largely comprised of hydrogen (about 92% of its mass) and helium (approximately 8% of its mass), with just small quantities of other heavier elements, such as oxygen, carbon, and nitrogen. The Sun can be divided into two major and distinct parts: the solar interior and the solar atmosphere. As the interior of the Sun is not directly observed, its properties are described using mathematical models of helioseismology. On the other hand, current high-resolution/cadence observations from the ground and space provide valuable information to investigate different parts of the solar atmosphere. Figure 1.1 depicts a visual representation of the solar interior and atmosphere as well as several additional features occurring in the solar atmosphere that will be discussed later.

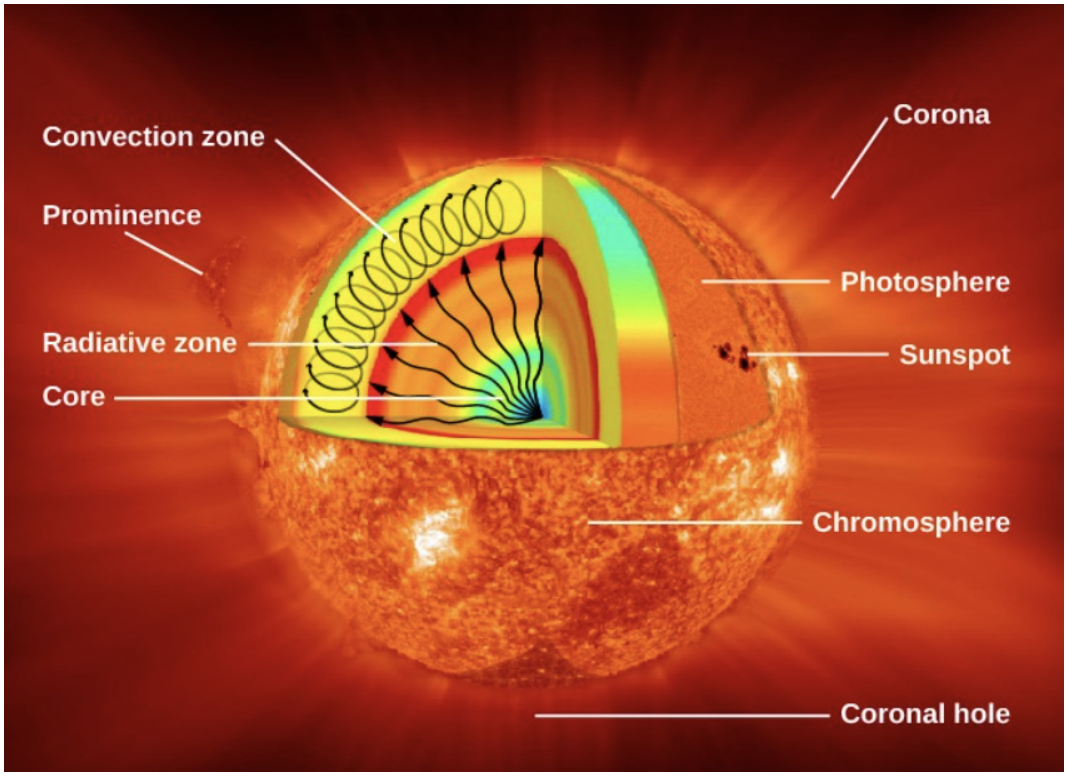

Figure 1.1: A schematic representation of the structure of the Sun, together with several features in the solar atmosphere. Credit: modification of work by NASA/Goddard.

1.2.1 The solar interior

Since the Sun does not have a solid surface, the delimitation of the upper boundary of the solar interior is taken conventionally as the height beyond which the solar plasma becomes optically thin and energy is radiated outward and spectral lines are formed. The regions of the internal part of the Sun are defined as regions that have a dominant physical mechanism driving its evolution. Information about the solar interior can be obtained only indirectly and this information was used to construct a standard solar model. The model for the solar interior assumes that half of the solar mass is concentrated in its core and that the temperature, density, and pressure diminishes as function of the radial distance from the center.

The centre of the Sun is occupied by the solar core, which is the hottest and densest region of the Sun and it extends to approximately 0.25 $R_{\odot}$. It has a temperature of around 15.7 million degrees Kelvin (K) and a density of 150 grammes per cubic centimetre (g/cm^3), which is up to 150 times higher than the density of water. Half of the Sun's mass is contained inside a volume that is just one-fiftieth of its total size, yet the core is responsible for 99.9% of the Sun's total energy production. The majority of this energy originates from two types of fusion reactions: the proton-proton chain reaction and the CNO (carbon-nitrogen-oxygen) cycle. The result of these fusion processes is the release of all of the Sun's energy. The results of thermonuclear reactions are photons and neutrinos that are able to leave the core and travel towards the surface of the Sun. Due to the weak interaction with matter, neutrinos travel through the solar interior practically unaffected with nearly the speed of light, taking about 5 seconds to reach the solar surface. On the other hand, the highly collisional medium inside the Sun causes photons to spend millions of years in the solar interior as they are transported through different layers

of the solar interior.

The radiative zone extends from the top of the solar core to about 70% of the solar radius. As one moves up from the bottom of the radiative zone to its top, the density of this layer decreases from 20 g/cm^3 to 0.2 g/cm^3. The photons created in the core are progressively transported across this layer by radiation and conduction. Since photons cannot travel a long distance without hitting with another particle, the density of the substance in this area prohibits photons from travelling for a long distance without changing direction and releasing some energy. In particular, the large number of collisions that photons encounter during this period have a significant impact, namely, increasing the wavelength of the high-energy -rays that emerge from the core, resulting in visible light at the solar surface.

On top of the radiative region we have the convective region, where the energy is transported via convection. The convection zone enables the convective transmission of heat and light. It is approximately 200,000 kilometres deep and transmits energy from the radiation region's edge to the Sun's surface. Bubbles emerge in the burning plasma at the bottom and lose heat to space as they rise to the top. The bottom plasma is very hot, and bubbles grow until they reach the top, when they lose their heat to space. As the plasma cools, it falls back toward the bottom of this layer. Between the radiative and convection zones, Spiegel and Zahn (1992) suggested a thin layer called tachocline, that presumably plays an important role in the creation of the solar magnetic field by a dynamo mechanism. In the tachocline, the uniform rotation of the radiative zone changes to a differential rotation in the convective zone, leading to intense shear flows. Thereby, the main dynamo models assumes that the magnetic field lines are stretched by the flows and the magnetic field is intensified in the tachocline before emerging due to plasma instabilities.

1.2.2 The solar atmosphere

The solar atmosphere is defined as the region of the Sun where photons may immediately escape and features may become visible. The atmosphere is divided into four distinct zones, each with its own set of physical characteristics.

The photosphere is a thin layer of plasma approximately 500 kilometres thick and it is the densest part of the solar atmosphere. It also is optically thick and opaque, and it absorbs the majority of solar light. The photosphere hosts the first visible manifestations of solar magnetism, where fields of different strengths emerge from the solar interior and form structures as sunspots, pores, plages, etc. The other important feature that can be seen in high resolution observations are the granular structure of the solar surface. The granules are the top of the convective cells just beneath the surface. Therefore, granulation covers practically the whole solar surface, resulting in several million granules of random forms being present at any one moment (see Figure 1.2). In each granule, the central region is shining because it is made up of hot, rising (with speeds of 0.5 to 1.5 km s^{-1}), horizontally outflowing plasma, while the 0.3 Mm-wide edges (or intergranular lanes) are dark because they are made up of cold, falling material (with speeds of 0.5 to 1.5 km s^{-1}). In magnetic areas close to the limb, granules seem brighter, allowing one to see deeper layers of a granule. Granules have an average lifespan of around 5 to 10 minutes, with a range of 1 to 20 minutes: the granules with the longest lifetime are the biggest and have the lowest random horizontal velocities, while those with shorter lifetimes are the smallest and largest.

In addition to these small-scale granulation patterns, there is the so called supergranular scale motion. Hart (1956) was the first to reported large scales horizontal velocities in the Equatorial region. Further analysis by Leighton et al. (1962) using Doppler photographs of the Sun revealed that such large

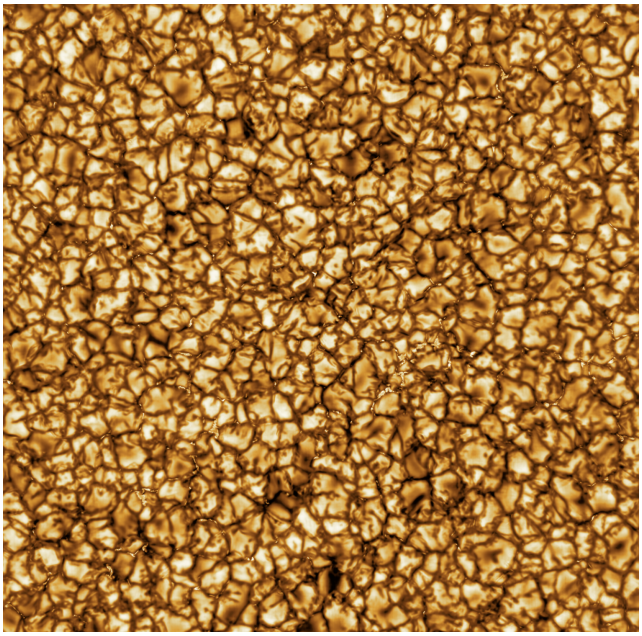

Figure 1.2: The granular structure of the solar photosphere. The granulation is a result of convective motions of bubbles of hot gas that rise from the solar interior. When these bubbles reach the surface, the gas cools and flows down again in the darker lanes between the bright cells (also called intergranular lanes). Credit: The Daniel K. Inouye Solar Telescope (DKIST).

scale motions cover the whole sun. The most common sizes of supergranules are 30 Mm, however they may be anywhere from 20 to 70 Mm (Rieutord and Rincon, 2010). Every supergranule cell has its own unique plasma flow pattern. Plasma rises in the centre of each supergranule cell, flows horizontally outward at around 350 m s^{-1}, and then lowers at the cell's edges (Hathaway et al., 2002; Rieutord et al., 2010).

The next layer above the photosphere the solar chromosphere, which is more transparent and has a thickness of approximately 2 Mm. Here the temperature rises steadily so that at the top of this region the temperature reaches a few ten of thousands of degrees K. It is optically thin in the near-ultraviolet, visible, and near-infrared ranges, but thick in strong spectral lines. The magnetic field becomes more inclined forming the magnetic network that is responsible for the existence of several phenomena in the chromosphere such as prominences and spicules. Above the solar limb prominences are luminous

ionised gas eruptions that may stretch thousands of kilometres from the chromosphere to the corona. On the solar disk these magnetic features are seen as dark regions and they are called fibrils. Spicules are defined as dynamic jets that stretch from the photosphere to the chromosphere (Foukal, 1971; De Pontieu et al., 2007; Pietarila et al., 2009). The chromosphere is also a very dynamic layer, where the plasma is changing from being partially ionised to fully ionised, it is the location where the plasma dynamics changes from being pressure force dominated to magnetic field dominated and flows are observed on all temporal and spatial scales (Martínez-Sykora et al., 2015).

The Transition Region lies between the corona and the chromosphere, featuring high temperature gradients and a small height width. In its lower part, the network structure resembles the one found in the chromosphere whereas the plasma features in the upper part tends to be more similar to the corona.

The solar corona is the uppermost part of the Sun's atmosphere and extends millions of kilometres outwards into the heliosphere. Given its very low density, the corona appears significantly less luminous than the Sun's surface. During eclipses, the corona is seen as a pale halo of low density and high temperature. The layer of the atmosphere shows a very strong magnetic structuring into coronal loops of different lengths and thicknesses. Coronal loops are described as magnetic structures that originate and terminate in active regions on the solar surface (see Figure 1.3). The length of the coronal loops varies over a very large scale: small active-region loops have a length in the range of 1 Mm to 10 Mm, the length of the standard active-region loops is 100 Mm, and it extends to 1,000 Mm for giant loops. Flaring loops have temperatures up to 10 MK, while active region loops have a temperature of about 2-3 MK.

The corona is also location of many very energetic phenomena, such as flares and coronal mass ejections (CMEs) generated by interconnecting magnetic fields of different polarity, or magnetic reconnection. Each reconnection implies

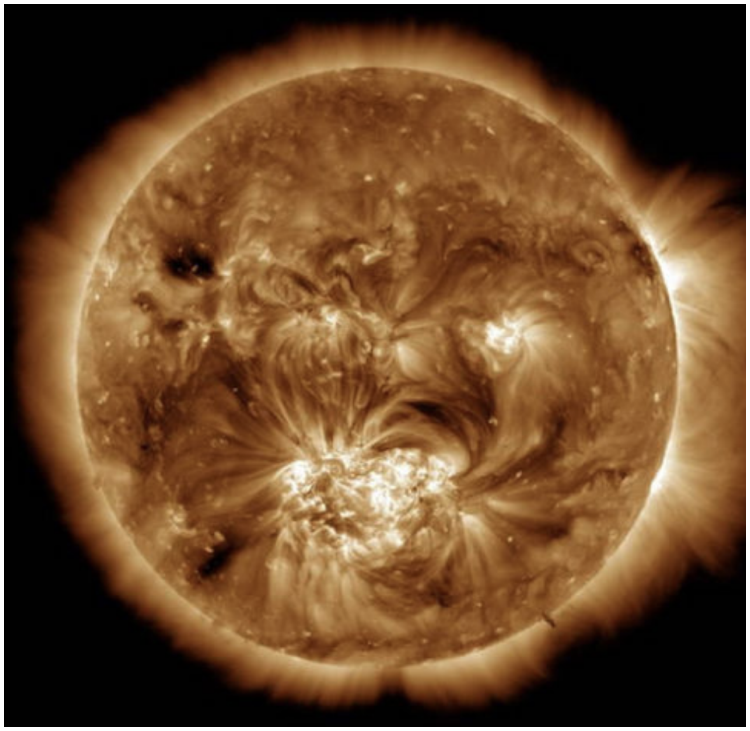

Figure 1.3: Magnetic structures in the solar corona seen in Extreme Ultraviolet wavelengths. The white/dark regions show very hot/cool plasma. Coronal loops appear as brigth arcades connecting two active regions. Credit: Solar Dynamics Observatory (SDO, NASA).

the transformation of magnetic energy into kinetic and thermal energy, with particles released into the interplanetary space.

The variation of various physical parameters (temperature, number density, pressure, etc.) in the solar atmosphere can be determined with the help of spectroscopic analysis that allows scientists to construct solar atmospheric models that are the foundation of many investigations. Figure 1.4 depicts variation of temperature and mass density with height according to the model developed by Vernazza et al. (1981), also known as the VAL model. The temperature of the photosphere drops with height by around thousand degrees Kelvin and reaching the minimum temperature of about 4400 K (see Figure 1.4).

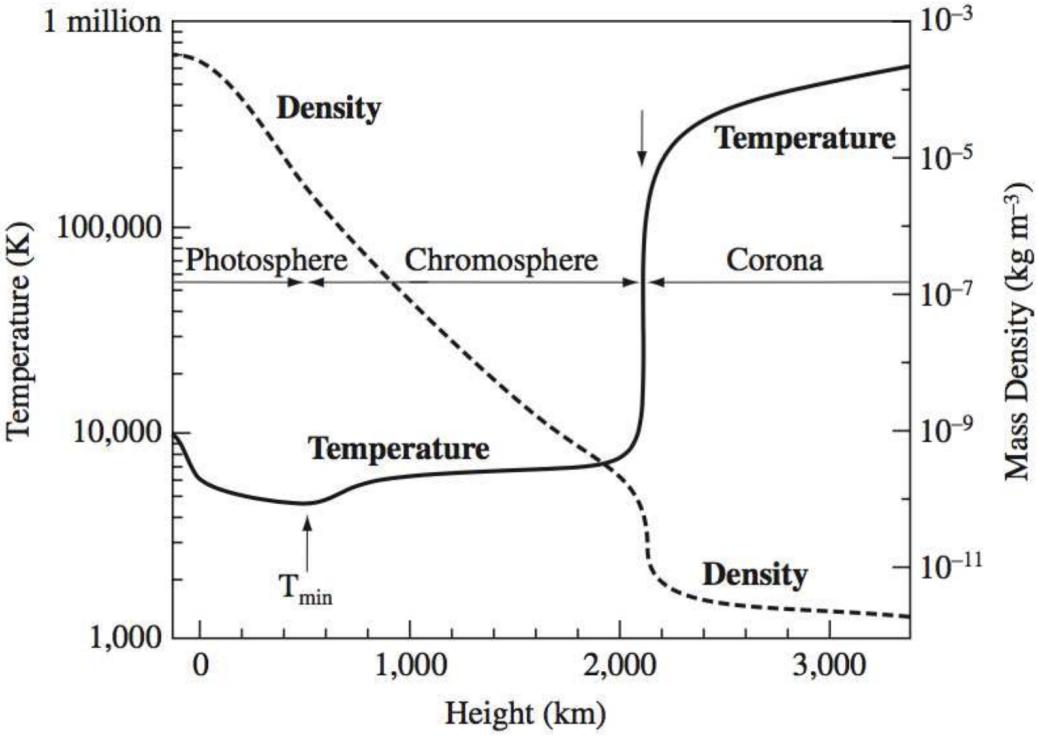

Figure 1.4: The variation of temperature and mass density with height according to the VAL model (Vernazza et al., 1981)

In many parts of the atmosphere, the one-dimensional VAL model accurately describes the changes of physical parameters. This model predicts a rapid increase in temperature from a chromospheric value of 25 000 K to over

1 MK in the corona in a very narrow transition region. The factors responsible for this sudden rise in temperature are still a mystery, and research into them is currently in progress. Research in this area addresses the famous coronal heating problem (Kuperus et al., 1981; Zirker, 1993; Erdélyi and Ballai, 2007; Parnell and De Moortel, 2012), etc.

Nowadays it is accepted that the heating of the upper part of the solar atmosphere is provided by alternating currents (AC) manifested as waves that transfer kinetic energy into heat or direct currents (DC) thanks to the interconnecting magnetic fields of different polarity that convert magnetic energy into heat. Recent observations have put many constraints of these processes in order to be viable mechanism able to compensate the radiative loss of the chromosphere and corona. As the solar environment is very dynamic, both sorts of events are likely to occur. To a great extent, wave-based heating processes have gone full circle since they were initially proposed as a means of providing the solar atmosphere with the required energy input (Parnell and De Moortel, 2012). One key aspect of wave-based heating problem is how waves are generated and how they propagate to the upper part of the atmosphere. In this respect solar photospheric swirling motions received increased attention because they have the ability to excite a broad variety of magnetohydrodynamic (MHD) waves, including slow and rapid magneto-acoustic as well as Alfvén waves (Fedun et al., 2011). Later in this Thesis, we will examine the physical mechanisms behind vortex dynamics.

The most widely acknowledged differentiation between solar phenomena is the division of areas on the surface of the Sun into two categories: quiet and active regions. The Sun's active regions are more dynamic than the quiet regions, allowing for a higher variety of transient events to occur. Sunspots, prominences, flares, and coronal mass ejections are all examples of transitory occurrences in active areas. Compared to active areas, the quiet Sun regions

are less dynamic and have a weaker magnetic field.

1.3 Vortices in the solar atmosphere

Vortices are dynamic features appearing in solar plasmas as a result of complex interplay of various conditions. They are ideal environments for energy transport, contributing to the energisation of the solar upper atmosphere. The present Thesis deals with the properties of these structures and the morphology of waves that can propagate on the surface of vortices.

1.3.1 Vortices in the solar photosphere

The solar photospheric plasma hosts a diverse range of dynamics and flows observed on all spatial and time scales. This environment is kept under continuous shuffling by the granular motion, where magnetic structures in the intergranular lanes are buffeted by granular cells, imposing translation or shearing motion that could end up as rotation.

Vortex motions, in particular, are a distinguishing characteristic of photospheric plasma fluxes. Nordlund (1985) initially observed the formation of plasma vortices in simulations based on convective motion. Using high-resolution observations of granulation taken with the SST, Brandt et al. (1988) evidenced vortex structures which visibly dominated the motion of the granules in their neighbourhood. Their research revealed that these structures had an average lifespan of around 1.5 hours. Moreover, it has been postulated that such vortices, which are a common characteristic of the solar convective zone, might serve as a key mechanism for the heating of solar/stellar chromospheres and coronae by twisting the imprints of magnetic flux tubes. Bonet et al. (2008) established that the vortices seen in the solar photosphere emerge in areas of cooled plasma downflows and that they can track the supergranulation

and the mesogranulation well using the motion of bright points (BPs). On the solar disk, the number of vortices is determined to be around 0.9×10^{-2} per Mm^2 (Bonet et al., 2008). According to Wedemeyer et al. (2016), as a fundamental physical process in the solar atmosphere, magnetic vortex flows occur when a magnetic field structure is swept into a vortex flow in an intergranular lanes at the solar surface (see Figure 1.5).

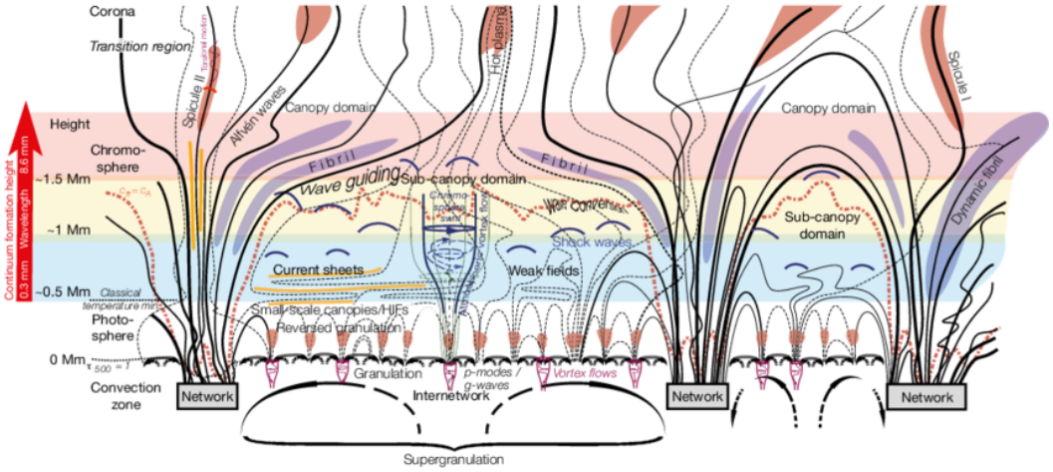

Figure 1.5: A schematic representation of the magnetic structure of the solar quiet Sun lower atmosphere. In this diagram, the magnetic field lines are shown by thick lines, whereas field lines with footpoints in the internetwork are depicted by thin dashed lines. The big arrows reflect large-scale convective fluxes while the small arrows denote flows on lower spatial scales (Wedemeyer-Böhm et al., 2009)

.

Vortices have been observed in the solar atmosphere in a wide range of temporal and spatial scale, from granular (e.g. 0.1-1 Mm in diameter) (Giagkiozis et al., 2018) to meso- and supergranular scales (e.g. 5-10 Mm in diameter) (Bonet et al., 2010; Requerey et al., 2018; Chian et al., 2019). Depending on the analysed scale, vortices will display different lifetimes. For granular scales, Giagkiozis et al. (2018) applied Fourier Local Correlation Tracking (FLCT) (Fisher and Welsch, 2008) to intensity maps and obtained a mean lifetime around 16.5 seconds and maximum duration around 100 seconds. In contrast, supergranular vortices can last for a couple of hours (Requerey et al., 2018;

Chian et al., 2019, 2020). In the photosphere, the evolution of magnetic elements that co-exist with rotational motion is strongly correlated with those vortices which act to stabilize the magnetic flux (Requerey et al., 2018).

1.3.2 Vortices in chromosphere

The rotation of photospheric magnetic footpoints is transmitted into the atmosphere above, where plasma is compelled to follow the spinning field structure (Wedemeyer and Steiner, 2014). This process generates a visible mark in the chromosphere, known as a chromospheric swirl (Wedemeyer-Böhm and van der Voort, 2009). The study by Wedemeyer and Steiner (2014), used SST and Solar Dynamic Observatory (SDO) observations to reveal rotating magnetic field structures, called magnetic tornadoes, extending from the solar surface into the chromosphere and the corona. These structures are detected as rings or spirals of rotating plasma in the Ca II 854.2 nm line core (also known as chromospheric swirls). Their analysis also showed that the observed chromospheric plasma motion is caused by the rotation of magnetic field structures, which again, are driven by photospheric vortex flows at their footpoints. Two vortex flow systems could be coupled and they are situated on top of each other. The intergranular vortex flow (IVF) is situated in the lower part of the system and it extends from the low photosphere into the convection zone. Once a magnetic field structure is co-located with an IVF, the rotation is mediated into the upper atmospheric layers and an atmospheric vortex flow (AVF, or magnetic tornado) is generated. Figure 1.6 illustrates the two forms of vortex flow.

Each AVF is triggered by an IVF, yet it is possible for IVFs to occur in the absence of a matching AVF. In quiet Sun regions, the upper convection zone has a high ratio of thermal gas pressure to magnetic pressure, which is

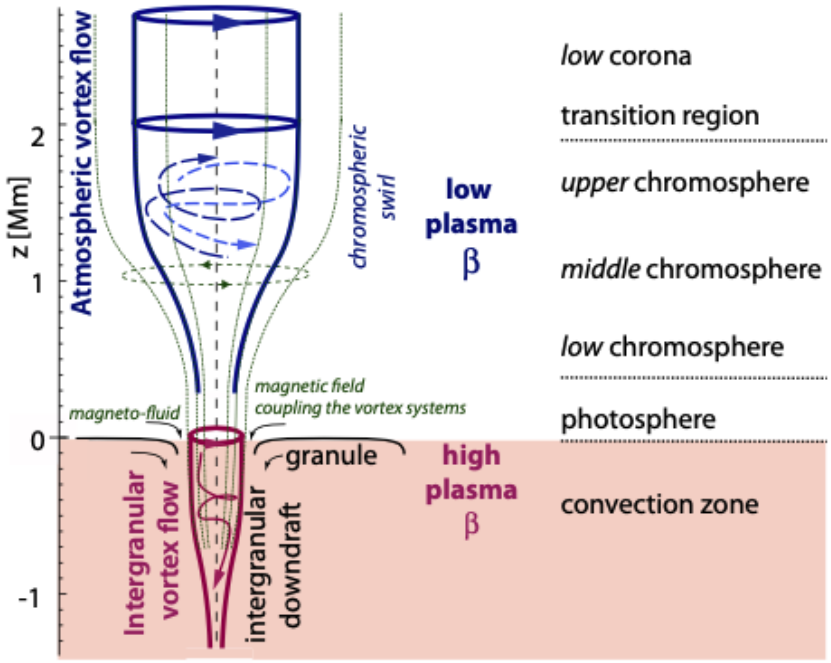

Figure 1.6: Diagram of the double nature of vortex flows. As discussed by Wedemeyer-Böhm et al. (2012), an atmospheric vortex flow (AVF), commonly known as a "magnetic tornado," may occur on top of a photospheric intergranular vortex flow (IVF), which extends into the upper convective zone and pushes the AVF above. The virtual borders of both vortex flows can be seen with strong solid lines to represent their virtual bounds. Plasma can flow up and down in the AVF (thin lines with arrows), but in the IVF it sinks. Low plasma-β conditions are required for the formation of the AVF, whereas higher plasma-β conditions are required for the formation of the IVF. The magnetic field connects the two vortices (thin line). Image adapted from Wedemeyer and Steiner (2014).

referred to as plasma-β that can be written as

$$\beta = \frac{nk_BT}{B^2/\mu_0}, \tag{1.1}$$

where $\mu_0 = 4\pi \times 10^7$ N A^{-2} is the magnetic permeability of free space, $k_B \approx 1.38 \times 10^{-23}$ J K^{-1} is the Boltzmann constant, T is the temperature, and n is the total number density. This parameter is one of the most important quantities in plasma physics, as its value compared to unity will denote dynamics of different nature. Figure 1.7 displays the plasma-β as function of height. For plasma-$\beta > 1$ the dynamics is mostly driven by pressure forces, while the regime corresponding to plasma-$\beta < 1$ means that the dynamics is driven mostly by magnetic forces. It is customary to consider that the plasma in the photosphere and lower chromosphere has plasma-$\beta > 1$, while in the upper chromospere, solar corona and solar wind the value of the plasma parameter is always smaller than 1.

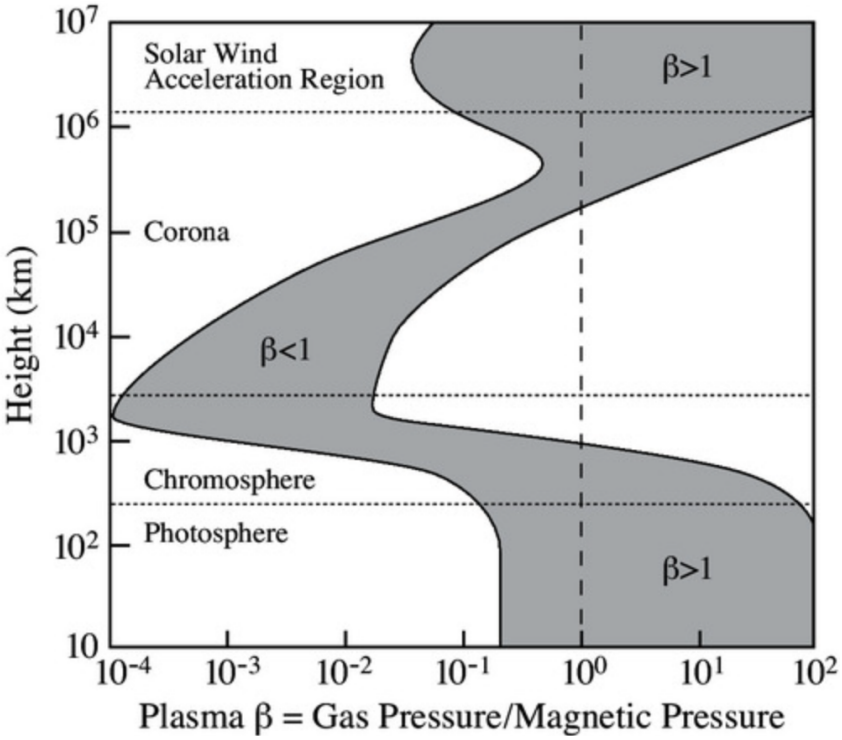

Figure 1.7: Plasma-β, the ratio of gas pressure to magnetic pressure, is shown as a function of height. Image adapted from Lang (2000).

In the solar convection zone the gas is significantly ionized so that the magnetic field is essentially frozen-in and is advected with the convective flows. As a consequence, the magnetic field is forced to spin in synchronised way with the plasma flow within an IVF, resulting in the rotation of the magnetic footpoint and, as a result, the rotation of the whole magnetic field structure. (Wedemeyer and Steiner, 2014).

The differentiation between IVFs and AVFs may also be understood in terms of the varied plasma conditions in which they take place. IVFs are created at the boundary between the dense upper convection zone and the photosphere, where the value of plasma-β is high. Here, the magnetic field is dragged along by the plasma, which has taken control. Alternatively, an AVF occurs in the atmosphere due to a driving IVF below, in a low plasma-β environment. This area is dominated by a magnetic field, which pulls the plasma along. The spatial extent of both vortex systems is shown in Figure 1.6 by the thick solid lines. The structure of the magnetic field is more complicated than shown in this simplified diagram (Figure 1.6), because plasma and its accompanying magnetic field may join or depart at any moment.

Recently, Shetye et al. (2019) suggested that the chromospheric swirl is a flux tube that extends above a magnetic concentration region in the photosphere. This idea is in accordance with the scenario proposed by Wedemeyer-Böhm et al. (2012), where the chromospheric swirls and the photospheric vortices are part of the same solar vortex tube. In the chromosphere, swirls have a lifetime of around 200-300 seconds (Tziotziou et al., 2018) and are dominated by transverse and rotational motions (Tziotziou et al., 2019).

According to the study by Yadav et al. (2020) the enormous vortices detected in the chromosphere region are most likely groups of many smaller vortices that have not yet been resolved by observations. They demonstrated that when appropriate spatial resolution declines, the vertical Poynting flux

drops fast and is carried mostly by horizontal plasma movements rather than vertical flows. Yadav et al. (2021) observed that vortices in the chromosphere have greater densities and temperatures than average values at the same spatial height.

In a recent study Silva et al. (2020) identified 3D vortices in numerical simulation data that were dispersed in intergranular zones from the photosphere to the low chromosphere. They were able to calculate average radial profiles of various physical parameters and analysed the dynamics across the vortical flows at various altitude levels. They found that vorticity growth is influenced by the magnetic field. The study by Silva et al. (2021) demonstrated that there are two sorts of vortex tubes: magnetic and kinetic vortices. The intergranular downflow is the preferred place for these two forms of vortices, however although magnetic vortices are typically found in limited regions where plasma-$\beta > 1$, rotating flow patterns, or kinetic vortices, have been observed in sites where plasma-$\beta < 1$. In this Thesis, we are going to focus on the kinetic vortex only.

Thesis focusses on the identification of vortices in numerical simulations and the determination of physical properties of vortices and the associated dynamics. We are also going to investigate the morphology of waves that are able to propagate on the surface of magnetic cylinders that mimic the rotational properties of vortices.

1.4 Thesis Outline

The main aim of this study is to understand of the nature of physical processes responsible for vortex dynamics, the interplay of various forces that drive the dynamics on the surface of vortices, but also on the signatures of waves that could propagate on vortices, here modelled as simple rotating magnetic flux

tubes. The current Thesis is a summary of my research and it is structured as:

Chapter 2 discusses the methods employed for vortex identification in numerical simulations and the theoretical foundations of guided MHD waves. Since one of the primary objectives of this Thesis is to gain a better understanding of the nature of the physical mechanisms that cause vortex dynamics, the very first step in their study is a review of the techniques used to detect vortices and their geometrical structures. As a consequence, in this Chapter, we will discuss the various approaches that are currently in use for the identification of vortices, with an emphasis on the their advantages and disadvantages. In order to qualitatively and quantitatively describe the MHD waves in vortex structures we will present the set of ideal MHD equations. These equations will be employed to discuss the nature and properties of MHD waves in a uniform unbounded magnetized plasma. Later, we will present the properties of guided MHD waves, i.e. waves constrained to propagate in a geometrically well defined structure such as a magnetic cylinder, as a first approximation needed to carry out the interpretation of presented results. This Chapter will also contain a description of wave identification techniques from observations, their advantages and limitations.

Chapter 3 is devoted to the understanding of the nature of physical processes responsible for vortex dynamics. Here we develop a new methodology to extract essential information from the boundary surface of vortex tubes. 3D high-resolution magnetoconvection MURaM numerical data has been used to analyse photospheric intergranular velocity vortices. The Lagrangian Averaged Vorticity Deviation (LAVD) technique was applied to define the centres of vortex structures and their boundary surfaces based on the advection of fluid elements. These surfaces were mapped onto a constructed envelope grid that allows the study of the key plasma parameters as functions of space and time.

Quantities that help in understanding the dynamics of the plasma, e.g. Lorentz force, pressure force, plasma-β were also determined. Our results suggest that, while density and pressure have a rather global behaviour, the other physical quantities undergo local changes, with their magnitude and orientation changing in space and time. At the surface, the mixing in the horizontal direction is not efficient, leading to appearance of localized regions with higher/colder temperatures. In addition, the analysis of the MHD Poynting flux confirms that the majority of the energy is directed in the horizontal direction. Our findings also indicate that the pressure and magnetic forces that drive the dynamics of the plasma on vortex surfaces are unbalanced and therefore the vortices do not rotate as a rigid body.

Chapter 4 focuses on the identification of morphology of waves propagating on the surface of a rotating magnetic cylinder that mimics the dynamics of a vortex. The signature of waves is studied by employing the same projection technique as presented in Chapter 3. The nature and properties of waves is studied using the Proper Orthogonal Decomposition (POD) technique on the surface of flux tube to identify various MHD modes.

In Chapter 5 we will summarise our key results and discuss the implications of our investigations. Here we will also draft a few directions of future research that could stem from our analysis.

CHAPTER 2

Theoretical foundations of plasma vortices and MHD waves

The main goal of this Thesis is to obtain a better understanding of the nature of the physical mechanisms associated with vortices in the solar atmosphere. As the current observational capabilities are not at the suitable level for detailed and systematic detection, their properties can be investigated in an indirect way. Instead, we can use realistic numerical simulations of the dynamics of the solar atmosphere to detect these vortices and study their evolution and properties. In section 2.1, we are going to discuss several approaches currently in use for the identification of vortices in numerical data, with an emphasis on their advantages and disadvantages. Secondly, this thesis also aims to study the morphology of waves and oscillations that can appear in connection to vortices. The wave modes that can propagate on the surface of these structures will be identified by means of the Proper Orthogonal Decomposition (POD) technique applied in connection with a cylindrical flux that mimics the true motion of a vortex. To understand the properties of waves recovered this way, we are going to discuss the properties of MHD waves propagating in a magnetic flux tube.

2.1 Vortex identification methods

An automated methodology to identify vortices relies on a precise mathematical and physical definition of what constitutes a vortex in the flow. However, there is still no universal definition for a vortex in the current literature (Haller et al., 2016). Thereby, distinct methodologies are based on different definitions of vortex.

2.1.1 Theory of fluid descriptions

Flows in fluids can be described using two different approaches: the Eulerian and Lagrangian methods. In the Eulerian description of fluid flow, individual fluid particles are not identified. Instead, a control volume is defined. In this description the fluid parameters that are function of space and time (pressure, velocity, acceleration, etc.) are described as fields within the control volume. In this description we are not interested in the location or velocity of any particular particle, instead the focus is on the velocity, acceleration, etc. of particles that are at a particular location of interest at a particular time. Since fluid flow is a continuum phenomenon, at least down to the molecular level, the Eulerian description is usually preferred in fluid mechanics. This approach also means that physical laws such as Newton's laws and the laws of conservation of mass and energy require a reformulation in this framework.

In contrast, in the Lagrangian description of flows in fluids individual fluid particles are tracked and their positions, velocities, etc. are described as a function of time. The physical laws, such as Newton's laws and conservation of mass and energy, apply directly to each particle. Given that a fluid is a system that has very high number of constituent particles, the use of the Lagrangian description is often too complex. Mathematically, the material derivative (the total derivative or substantial derivative) bridges the Lagrangian and Eulerian

descriptions.

2.1.1.1 Eulerian methods

In many cases, the Eulerian vortex criteria are applied. These criteria are derived from the spatial derivatives of the velocity or field, and include features such as closed spiralling streamlines, iso-vorticity surfaces, pressure minima, and so on. A coherent structure is identified by the Eulerian criteria as concentrated areas of high vorticity, and it typically contains the key properties of the flow caused by a vortex filament (McWilliams, 1984; Hussain, 1986; Chakraborty et al., 2005). These Eulerian procedures construct a function that may be evaluated point-by-point and then categorise each point as either within or outside a vortex based on the point values of the function. The majority of criteria for identifying local vortices are derived from the velocity gradient tensor (or Jacobian), which makes them Galilean invariant, that is, invariant under constant speed translation of the underlying coordinate system (Post et al., 2003; Günther et al., 2015). The most often employed local criteria are: the Q-criterion (Hunt et al., 1988), the λ-criterion (Jeong and Hussain, 1995), the Δ-criterion (Chong et al., 1990), and the whirling strength, λ_{ci}-criterion (Chong et al., 1990).

2.1.1.2 Lagrangian methods

For Lagrangian techniques, a vortex is often seen as a developing region with a high degree of material invariance (Chakraborty et al., 2005; Haller, 2005). Every Lagrangian technique is built around the flow map, which is a vector quantity that maps fluid paths from their beginning positions in space to their end locations in space after an integration time is taken into account. With the help of experimental and numerical flow data, the Lagrangian approaches are able to uncover repelling, attracting, and shear material surfaces. This allows

for a more simplified understanding of the overall flow geometry, as well as precise quantification of material transport, which results in a powerful prediction of vortical features in the flow (Haller, 2015). There have been a number of Lagrangian techniques presented throughout the past two decades (Peacock and Dabiri, 2010; Peacock et al., 2015; Haller, 2015; Shadden, 2011; Allshouse and Peacock, 2015). The Lagrangian coherent structures (LCS) analysis was pioneered by Haller (2001), and it comprises a set of Lagrangian techniques that determine quantities by observing the relative behaviour of fluid particle trajectories. As research in LCS analysis progresses, it is inevitable that the scope of the area expands. Recently, Haller (2011, 2015) developed a stretching-based mathematical technique to find Lagrangian vortical structures from complicated geophysical flow data using the geodesic theory. The concept of rotationally coherent vortices, as impermeable tubular material areas with a high concentration of vorticity throughout a limited time period, was introduced most recently by Farazmand and Haller (2016). In this manner, Haller et al. (2016) use the Lagrangian Averaged Vorticity Deviation (LAVD) to identify rotationally coherent vortices, whose constituents display identical mean material rotation.

These new methodologies to identify LCS were developed in order to give objective (material invariant) vortex extraction methods for LCS analysis. To be objective, vortex identification systems must provide invariant findings when subjected to Euclidean coordinate changes of the form (Truesdell and Noll, 2004),

$$y = Q(t)x + p(t), \tag{2.1}$$

where $Q(t)$ denotes a time-dependent proper orthogonal tensor and $p(t)$ denotes a time-dependent translation. As a result, the Lagrangian vortex is described objectively in this manner, indicating the development of matter regardless of the observer's perspective (Gurtin, 1982). In recent years, La-

grangian techniques have risen in favour as a new vortex identification strategy, thanks to their objective nature, i.e. the fact that they are frame invariant under any smooth translation and rotation of the coordinate system (Günther et al., 2015).

2.1.2 A Description of Detection Techniques

2.1.2.1 The Γ_1 and Γ_2 method

The study by Graftieaux et al. (2001) suggested the use of the Γ_1 and Γ_2 functions to determine the locations of the vortex centres and boundaries, respectively. According to this study the scalar function Γ_1 can be defined by employing the topology of streamlines to locate the centre of the vortex core in two-dimensional (2D) flow. When the velocity field is sampled at discrete spatial locations in a rectangular domain S of fixed size and geometry centred on P, the function Γ_1 is calculated as (Graftieaux et al., 2001)

$$\Gamma_1(P) = \frac{1}{N} \sum_S \frac{(\mathbf{PM} \times \mathbf{U}_M) \cdot \mathbf{z}}{||\mathbf{PM}|| \cdot ||\mathbf{U}_M||} = \frac{1}{N} \sum_S sin(\theta_M). \tag{2.2}$$

where N is the number of points M inside S, $\mathbf{z}$ denotes the unit vector normal to the measuring plane, θ_M represents the angle between the velocity vector $\mathbf{U}_M$ and the radius vector $\mathbf{PM}$. In this context, the parameter N serves as a spatial filter, although it only has a little impact on the position of the maximum of Γ_1 function's peak. In order to address this problem, the preceding Γ_1 algorithm was modified to include a local function, Γ_2, that takes into consideration a local convection velocity $\tilde{\mathbf{U}}_P$ in the vicinity of P and, therefore, it is Galilean invariant in nature. The Γ_2 function is defined as (Graftieaux et al., 2001)

$$\Gamma_2(P) = \frac{1}{N} \sum_S \frac{[\mathbf{PM} \times (\mathbf{U}_M - \tilde{\mathbf{U}}_P)] \cdot \mathbf{z}}{||\mathbf{PM}|| \cdot ||\mathbf{U}_M - \tilde{\mathbf{U}}_P||}, \tag{2.3}$$

where $\tilde{\mathbf{U}}_P = \frac{1}{S}\int_S \mathbf{U} dS$. The study conducted by Graftieaux et al. (2001) has shown that the magnitude of Γ_2 is greater than $2/\pi$ inside a vortex's inner core. Flows with values of $\Gamma_2 < 2/\pi$ are dominated by strain, while flows corresponding to $\Gamma_2 = 2/\pi$ are dominated by pure shear.

This method produces poor vortex boundaries, which makes it difficult to properly isolate the structure and investigate the physical parameters at the surface of the vortex. The other difficulty with the Γ-method is that it performs the identification on the basis of the topological streamline of velocity fields, which is not an objective quantity (Haller et al., 2016). This may lead to false vortex detection (see, e.g. Silva et al., 2018), as well as high dependence on corrections made to remove satellite motion from observational data (Günther and Theisel, 2018).

2.1.2.2 Δ- criterion

Vortices are defined by the Δ criterion as a region where the velocity gradient tensor $\nabla\mathbf{v}$ has a pair of complex conjugate eigenvalues and a real eigenvalue, as opposed to other regions (Perry and Chong, 1987). If λ_1, λ_2, and λ_3 are the eigenvalues of the 3×3 matrix of $\nabla\mathbf{v}$, then the characteristic equation may be written as

$$\lambda^3 + I_1\lambda^2 + I_2\lambda + I_3 = 0, \tag{2.4}$$

The I_1, I_2, and I_3 are invariants of the characteristic equation (2.4), and their values can be given in terms of Viéte's relations as

$$I_1 = (\lambda_1 + \lambda_2 + \lambda_3) = tr(\nabla\mathbf{v}) \tag{2.5}$$

$$I_2 = \lambda_1\lambda_2 + \lambda_2\lambda_3 + \lambda_3\lambda_1 - \frac{1}{2}[tr(\nabla\mathbf{v}^{\mathbf{2}} - tr(\nabla\mathbf{v})^2)] \tag{2.6}$$

$$I_3 = \lambda_1\lambda_2\lambda_3 = det(\nabla\mathbf{v}) \tag{2.7}$$

According to Equation (2.5), the discriminant of the characteristic is given by

$$\Delta = \left(\frac{\tilde{Q}}{3}\right)^3 + \left(\frac{\tilde{R}}{2}\right)^2, \tag{2.8}$$

where $\tilde{Q} = I_2 - I_3^2$ and $\tilde{R} = -I_3 - \frac{1}{3}I_1^2$. If $\Delta \leq 0$ is a real number, all three eigenvalues of the characteristic equation are real, however, if $\Delta \geq 0$, the characteristic equation has one real and two conjugate complex eigenvalues.

The disadvantage of this approach is that it will not provide us with information about the boundaries of the vortex tube, i.e. will not fulfill the purpose we would like to pursue here.

2.1.2.3 Vorticity

It has been more than 150 years since Helmholtz first introduced the term vorticity. For a fluid with velocity $\mathbf{U}(x, y, z)$, the vorticity vector can be defined as the curl of its velocity, $\omega = \nabla \times \mathbf{U}$. A vortex line or vorticity line is a line which is everywhere tangent to the local vorticity vector. Vortex lines are defined by the relation

$$\frac{dx}{\omega_x} = \frac{dy}{\omega_y} = \frac{dz}{\omega_z}, \tag{2.9}$$

where ω_x, ω_y and ω_z are the three components of the vorticity vector ω in Cartesian coordinate system.

A vortex tube is defined as the surface in the continuum formed by all vortex lines passing through a given closed curve in the continuum. The vortex flux is the integral of the vorticity across a cross-section of the tube, and is the same everywhere along the tube. As a consequence, the vorticity may be utilised to immediately detect vortices without the need for further information. This approach has the disadvantage of being unable to discriminate between whirling movements and shearing motions, which is a problem in certain situations (Kida and Miura, 1998). The vorticity of a fluid may be

easily seen by visualising isosurfaces ($|\omega|$) of the fluid (Holmén, 2012). This may be troublesome, though, since various thresholds can produce geometrical formations with varying properties.

2.1.3 Lagrangian Averaged Vorticity Deviation (LAVD)

The Lagrangian-averaged vorticity deviation was defined by Haller et al. (2016) as an objective criteria for defining vortices. The velocity in fluid mechanics is defined as

$$\dot{\mathbf{x}} = \mathbf{u}(\mathbf{x}(\mathbf{x}_0, t_0, t), t), \tag{2.10}$$

where $\mathbf{x}_0$ represents the starting location of the fluid particle at time t_0, $(\mathbf{x}_0, t_0, t)$ represents the journey of a fluid particle starting from the point $\mathbf{x}_0$ and moving in time between t_0 and t.

LAVD is defined as the trajectory integral of the normal vorticity deviation from its spatial mean around as certain location in space $\mathbf{x_0}$ from time t_0 to t, as

$$LAVD^t_{t_0}(\mathbf{x}_0) = \int_{t_0}^{t} |\boldsymbol{\omega}(\mathbf{x}(s, \mathbf{x}_0), s) - \bar{\boldsymbol{\omega}}(s)| ds. \tag{2.11}$$

where $\bar{\boldsymbol{\omega}}$ denotes the spatial mean of vorticity and $\boldsymbol{\omega}(\mathbf{x}(s, \mathbf{x_0}), s)$ denotes the vorticity along a material trajectory. According to Haller et al. (2016), a rotationally coherent Lagrangian vortex may be described as a nested collection of outward decreasing tubular level sets of Lagrangian vortex dynamics. The boundary of a Lagrangian vortex is characterised as the most convex member of a nested tube family that meets the convexity deficiency and arc length standards.

Later, in Chapter 3, we use the LAVD approach to detect vortex flows, namely the centre of circulation and the boundary of the vortex flow. The LAVD approach, in combination with MURaM magneto-convection simulation

data, is used to find and follow the development of 3D vortex tubes in the solar photosphere.

2.2 The plasma

Plasma is considered to be the fourth state of matter and it makes up 99% of the visible universe. A plasma is a hot ionized gas consisting of approximately equal numbers of positively charged ions, negatively charged electrons and neutral atoms (if temperatures are not high enough for a full ionisation). The characteristics of plasmas are significantly different from those of ordinary neutral gases as the interaction between their constituent particles are controlled by electromagnetic forces. In addition, the dynamics of particles is also controlled and driven by the electromagnetic field. In the magnetohydrodynamics (MHD) approximation although the amalgam of charged particles is made up from different charges, the plasma can be considered as quasi-neutral as deviations from charge neutrality occur, in general, over very short distances (also known as the Debye length). The charge neutrality is equivalent to the condition that the number densities of positively and negatively charged particles is approximately equal. Deviations from quasi-neutrality usually are small since the moment an imbalance occurs, large electric fields are produced that act to restore the charge neutrality.

Plasmas can be produced by heating an ordinary gas to such high temperatures that the kinetic energy of particles exceed the ionisation energy. Thanks to collisions, some of the electrons from atoms become free, forming a mixture of charged (positive and negative) particles. These plasmas need high temperatures, for instance a hydrogen gas becomes a plasma for temperature of the order of a few thousand degrees Kelvin. On the other hand, a gas can also become a plasma when its atoms or molecules are exposed to energetic

photons (e.g. ultraviolet light or X-rays).

Plasmas can be categories in two broad classes: natural and laboratory-made plasmas. Usually natural plasmas are the space plasmas that include our Sun, other stars, planetary upper atmospheres, and a large portion of the interstellar and interplanetary space.

Nowadays the study of plasmas was made easier by studying the formation and evolution of such environments in laboratories and other plasma devices. One of the most important of these is human-kind's attempt to obtain controlled thermonuclear fusion. To achieve that high temperatures are needed (of the order of 10^7 K) to overcome the Coulomb repulsion between nuclei. Since a fusion plasma would be rapidly cooled by the external walls of any ordinary device, huge efforts were invested in containing the plasma by magnetic fields, using the "magnetic-bottle" principle. The effort to find a technological configuration that is also economical to confine the dense and hot plasma remains one of the main challenges of fusion research. Other laboratory-related plasma devices include magnetohydrodynamic generators of electricity from high temperature plasma jets, ion engines for spacecraft propulsion, surface treatment processes involving the injection of ions on metal surfaces, etc.

2.3 Theory of magnetohydrodynamic waves

The MHD description of dynamics in plasmas can be considered as a precursor of the modern plasma physics. MHD considers the plasma as a conducting fluid, where temporal and spatial scales are well above the scales that involve collisions between particles. As such, the traditional MHD approximation is a macroscopic approach that does not take into account collisional effects, however any modification of equations due to non-ideal effects is due to microscopic effects (e.g. viscosity, conductivity, thermal conduction, etc.). The governing

equations of MHD are adapted from fluid mechanics with appropriate modifications to consider for electromagnetic forces that act between electrically charged particles. A full set of equations includes the definition of currents, as function of the applied electric field and this was accomplished by using the a linear form of Ohm's law. Since the plasma (in the first approximation) can be considered as electrically neutral, the net charge density is assumed to be negligible. Since the fluid motions tend to be slower than the characteristic time scales of the plasma, the displacement currents are also neglected. These assumptions, together with an appropriate equation of state (assuming the plasma as an ideal gas) fully describe the behaviour and dynamics of plasmas.

MHD operates with a set of coupled nonlinear PDEs that describe the spatial and temporal evolution of the plasma, magnetic field and their interaction. These vectorial and scalar equations can contain non-ideal terms (describing, e.g. transport mechanisms such as viscosity, electrical resistivity, thermal conductivity, etc.), however these create an unnecessary complexity that can be neglected when studying the nature of possible waves in plasmas. That is why we are going to assume that here we are dealing with an ideal environment, where the characteristic wavelength are much shorter than any characteristic length involved in non-ideal processes. Non-ideal effects will affect the temporal evolution of waves' amplitude causing a damping of waves.

2.3.1 The ideal MHD equations

The set of ideal MHD equations expresses conservation laws (mass, momentum and energy), which are universal laws for physical systems. Although the plasma contains a mixture of particles (here we assume that the plasma is fully ionised), we consider that they have a collective motion and their dynamics can be described with the help of macroscopic quantities. Accordingly, the set

of ideal MHD equations is (Aschwanden, 2006):

$$\frac{d\rho}{dt} = -\rho\nabla \cdot \mathbf{v}, \tag{2.12}$$

$$\rho\frac{d\mathbf{v}}{dt} = -\nabla p + \rho\mathbf{g} + \frac{1}{\mu_0}[(\nabla \times \mathbf{B}) \times \mathbf{B}], \tag{2.13}$$

$$\frac{d}{dt}\left(\frac{p}{\rho^\gamma}\right) = 0, \tag{2.14}$$

$$\nabla \times (\mathbf{v} \times \mathbf{B}) = \frac{\partial \mathbf{B}}{\partial t}, \tag{2.15}$$

$$\nabla \cdot \mathbf{B} = 0, \tag{2.16}$$

where

$$\frac{d}{dt} = \frac{\partial}{\partial t} + \mathbf{v} \cdot \nabla, \tag{2.17}$$

is the convective operator, γ, μ_0, ρ, p, $\mathbf{v}$, and $\mathbf{B}$ are the adiabatic index, permeability of free space, density, pressure, velocity field, and induction of the magnetic field, respectively and $\mathbf{g}$ is gravity.

Equation (2.12) is the mass conservation equation and expresses that in a system that is closed to all transfers of matter and energy, the mass of the system must remain constant over time, as the system's mass cannot change. This equation is one of the most fundamental relations relevant not only to fluid dynamics, but also chemistry, electromagnetism (with mass density and velocity replaced by charged density and current density), quantum mechanics (conservation of probability), chemistry, etc.

Equation (2.13) describes the equilibrium of forces and it can be derived from Newton's second law. Accordingly, the movement of a plasma element of unit volume is driven by pressure forces (∇p), gravitational force ($\rho\mathbf{g}$), and the Lorentz force ($(\nabla \times \mathbf{B}) \times \mathbf{B}/\mu_0$). Possible additional forces (e.g. Coriolis force, viscous forces, etc.) are all neglected.

Equation (2.14) connects the thermodynamical quantities of pressure (p)

and density (ρ) and describes the conservation of energy in an adiabatic process. The zero on the right-hand side of this equation specifies that there are no additional sinks or sources of energy in the system.

The next equation (2.15) is the induction equation that can be derived from Ohm's law taking into account Ampére's law and it connects the magnetic field ($\mathbf{B}$) and fluid velocity. In this approximation the field and plasma are tightly coupled, being frozen into each other.

The last equation of the above system (2.16) is the solenoidal condition that stipulates that there are no magnetic monopoles and the magnetic field lines are closed.

Using the fact that the processes we are interested in are adiabatic, in Equation (2.13) we can replace pressure term using the relation $\nabla p = c_S^2 \nabla \rho$, where $c_S = \sqrt{\gamma p/\rho}$ is the adiabatic sound speed. Using standard vector identities we can include the last equation of the above system to rewrite the set of ideal MHD equations into (Aschwanden, 2006):

$$\frac{d\rho}{dt} = -\rho \nabla \cdot \mathbf{v}, \tag{2.18}$$

$$\rho \frac{d\mathbf{v}}{dt} = -c_S^2 \nabla \rho + \rho \mathbf{g} + \frac{1}{\mu_0} \left[\left(-\frac{1}{2} \nabla \mathbf{B}^2 \right) + (\mathbf{B} \cdot \nabla) \mathbf{B} \right], \tag{2.19}$$

$$\frac{\partial \mathbf{B}}{\partial t} = -\mathbf{B}(\nabla \cdot \mathbf{v}) + (\mathbf{B} \cdot \nabla)\mathbf{v} - (\mathbf{v} \cdot \nabla)\mathbf{B}. \tag{2.20}$$

The last term of Equation (2.19) was derived by writing the Lorentz force as the sum of its projection in the parallel and perpendicular direction to the magnetic field. In this form the first term describes the magnetic pressure, while the second one describes the magnetic tension.

2.3.1.1 Linearised MHD equations

One of the difficulties in solving the system of MHD equations is that it contains highly nonlinear (quadratic and cubic) terms. However, this difficulty can be surpassed by considering the linearised version of the system. Accordingly we will assume that in the equilibrium the system is stationary and all forces are balanced. Next, we consider *small* perturbations of physical quantities and write all physical quantities as the sum between an equilibrium value (denoted by an index 0) and a small perturbation (denoted by an index 1), which means that in the original system of equations all terms containing the product or square of perturbations can be neglected. In order to simplify the discussion we are going to assume that the wavelengths we will operate are much sorter than the gravitational scale-height (the distance over which gravitational stratification is defined), therefore, the gravitational restoring force can be neglected.

Accordingly, let us write all physical quantities as

$$\mathbf{B}(\mathbf{r},t) = \mathbf{B_0} + \mathbf{B}_1(\mathbf{r},t), \quad \mathbf{v}(\mathbf{r},t) = \mathbf{v_0} + \mathbf{v_0}(\mathbf{r},t) = 0 + \mathbf{v}_1(\mathbf{r},t),$$

$$\rho(\mathbf{r},t) = \rho_0 + \rho_1(\mathbf{r},t), \quad p(\mathbf{r},t) = p_0 + \rho_1(\mathbf{r},t).$$

Next we substitute these quantities into the set of ideal MHD equations. Taking into account the simplifications mentioned above, we obtain

$$\frac{d\rho_1}{dt} = -\rho_0 \nabla \cdot \mathbf{v}_1 \tag{2.21}$$

$$\rho_0 \frac{d\mathbf{v}_1}{dt} = -c_S^2 \nabla \rho_1 + \frac{1}{\mu_0}[-\nabla(\mathbf{B_0} \cdot \mathbf{B}_1) + (\mathbf{B}_0 \cdot \nabla)\mathbf{B}_1] \tag{2.22}$$

$$\frac{\partial \mathbf{B}_1}{\partial t} = -\mathbf{B}_0(\nabla \cdot \mathbf{v}_1) + (\mathbf{B}_0 \cdot \nabla)\mathbf{v}_1 \tag{2.23}$$

This set of equations are known as linearised MHD equations. These coupled

equations will be used in the next Chapter to discuss the properties of waves in homogeneous and structured plasmas.

2.3.1.2 Wave in an unbounded and homogeneous plasma

The simplest configuration in which waves can be studied is when the plasma is unbounded and the equilibrium is static, stationary and homogeneous, i.e. the equilibrium quantities do not have any temporal and spatial dependence. That is why we assume that the homogeneous magnetic field points in the z-direction, so we can write $\mathbf{B}_0 = (0, 0, B_0)$. Waves will propagate with wave vector $\mathbf{k} = (0, k_y, k_z)$ in the $y - z$ plane. The wave propagation in such media has been discussed extensively by many authors (e.g. Cowling (1976), Roberts (1981a), Priest (2014), etc).

Combining Equations (2.21)- (2.23), we can derive relation that describes the evolution of the compressibility factor ($\Delta = \nabla \cdot \mathbf{v}_1$) as

$$\frac{\partial^4 \Delta}{\partial t^4} - (c_S^2 + v_A^2)\frac{\partial^2}{\partial t^2}\nabla^2\Delta + c_S^2 v_A^2 \frac{\partial^2}{\partial z^2}\nabla^2\Delta = 0, \tag{2.24}$$

where $v_A^2 = B_0^2/\mu_0\rho_0$ is the square of the Alfvén speed. Next we Fourier decompose the above equation and write $\Delta = \hat{\Delta} e^{\imath(\omega t + k_y y + k_z z)}$, where ω is the real frequency of waves. The above relation will be used in what follows to derive the dispersion relation of waves.

The simplest limit in which the dispersion relation can be derived is the incompressible case that corresponds to $\nabla \cdot \mathbf{v}_1 = 0$. In this case the wavevector is perpendicular to the velocity perturbation, meaning that we are dealing with a transversal wave that is purely a magnetic wave, also known as the Alfvén wave. In this limit the governing equation (2.24) reduces to the very simple dispersion relation

$$\omega^2 = v_A^2 k^2 \cos^2(\theta) \quad \text{or} \quad v_{ph}^2 = v_A^2 \cos^2(\theta), \tag{2.25}$$

where $v_{ph} = \omega/k$ is the phase speed of waves and θ is the angle between the wavevector and the background magnetic field. This dispersion relation describes the non-dispersive Alfvén wave (often called shear Alfvén wave) whose only restoring force is the magnetic tension. We should note that these waves propagate faster along the field, but do not propagate normal to the field.

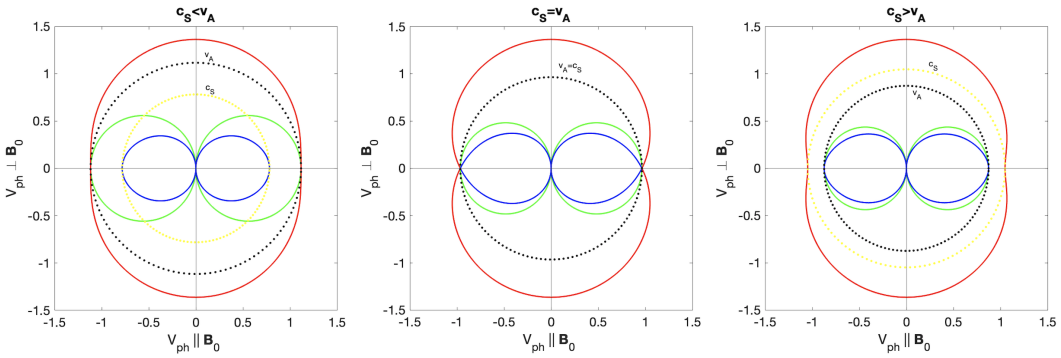

Figure 2.1: Friedrichs diagram showing the variation of the phase speed of the three modes depending on the inclination angle of the wavevector compared to the direction of the equilibrium magnetic field (here assumed to be along the horizontal direction). The phase speed of slow (v_{slow}), Alfvén (v_{Alfvn}) and fast (v_{fast}) waves are shown in blue, green, and red lines, respectively. For reference we also plot the magnitude of the sound (c_S) and Alfvén (v_A) speeds in yellow and black dashed lines.

In the compressible case, both the magnetic force and pressure gradients are important. Using Equation (2.25) we can obtain the dispersion relation of magneto-acoustic modes (the fast and slow modes) as given by

$$v_{ph}^4 - (c_S^2 + v_A^2)v_{ph}^2 + c_S^2 v_A^2 \cos^2(\theta) = 0. \tag{2.26}$$

Clearly, Equation (2.26) describes propagation of a pair of waves travelling in opposite directions, whose phase speeds are given by

$$v_{ph} = \pm\sqrt{\frac{1}{2}(c_S^2 + v_A^2) + \frac{1}{2}(c_S^4 + v_A^4 - 2c_S^2 v_A^2 \cos(2\theta))^{1/2}}, \tag{2.27}$$

$$v_{ph} = \pm\sqrt{\frac{1}{2}(c_S^2 + v_A^2) - \frac{1}{2}(c_S^4 + v_A^4 - 2c_S^2 v_A^2 \cos(2\theta))^{1/2}}. \tag{2.28}$$

The two magnetoacoustic modes can be seen as a sound wave modified by the magnetic field and an Alfvén wave modified by the gas pressure. In the case of vanishing magnetic field the slow wave disappears, and the fast wave becomes a sound wave.

The properties of these three modes can be clearly seen in a polar diagram (also known as Friedrich diagram) shown in Figure 2.1). The discussion of these properties depends very much on the value of plasma-β and we can distinguish between two distinct situations corresponding to photospheric ($\beta \gg 1$) or coronal ($\beta \ll 1$) limits. In all cases slow and Alfvén waves cannot propagate across the field. The only mode that can propagate across the field is the fast mode and its phase speed will be $(c_S^2 + v_A^2)^{1/2}$. For slow modes, the phase speed is in the range of $0 \leq v_{ph} \leq min(c_S, v_A)$, however, the phase speed of the fast mode is in the range of $max(c_S, v_A) \leq v_{ph} \leq (c_S^2 + v_A^2)$.

2.3.2 Dispersion relations of MHD waves in structured plasmas

In reality the solar magnetic field is not diffuse, instead it tends to accumulate in magnetic entities that can take various forms (e.g. sunspots, spicules, prominences, coronal loops, coronal plumes, etc), meaning that some sort of finite size structuring takes place. The simplest configuration mimicking structuring is the magnetic interface, similar to the density interface in fluids. In this model the magnetic field is parallel to the separating interface and there will be a jump in the value of the magnetic field across the interface. Of course, this is an ideal configuration, as sudden jumps (or true discontinuities) do not exist in reality, instead the magnetic field has a smooth transition from one region to another one. As a possible extension of a single interface case we will study the dispersion relation of waves in a magnetic slab and later in a magnetic cylinder. The last two examples are unique because by considering

guided waves we explore the dispersive character of these waves, i.e. their propagation speed will depend on the wavelength of waves. The structuring of the magnetic field can be considered as an extreme inhomogeneity that still allow us to derive dispersion relations.

2.3.2.1 Wave propagation in magnetic interface

There are several examples in the solar atmosphere where we can consider that two regions of different properties are separated by an interface along which surface waves can propagate, e.g. edges of sunspots or prominences, various discontinuities in the coronal hole and solar wind, etc. To model the properties of waves, for simplicity, we will assume that the magnetic field is parallel to the interface. Therefore, the separating interface can be considered as a tangential discontinuity. The method of finding the dispersion relation is similar to the technique that is so well known in fluid mechanics: we are going to solve the MHD equations on both sides of the interface and the solutions will be matched at the interface taking into account kinematic and dynamic boundary conditions: the normal component of the velocity and total pressure (kinetic plus magnetic) are continuous across the interface. In addition we impose that the wave stays localised on the interface, meaning that in the transversal direction waves are evanescent (their amplitude decays exponentially with distance)

The problem of surface wave propagation along an interface and the effect of compressibility on these waves was studied first by Wentzel (1979), who focussed on the energy carried by a surface wave. The dispersion relation for isothermal disturbance derived by Wentzel (1979) was fully understood following the study by Roberts (1981a), who showed that in fact there are two surface waves that can propagate in a sharply structured plasma, and the existence of these waves depends very much on the particular values of the magnetic field. The dispersion relation of waves propagating at an interface

separating two regions of densities ρ_i and ρ_e was derived by Roberts (1981a) and it reads

$$\rho_i(k^2v_{Ai}^2-\omega^2)(m_e^2+\ell^2)^{\frac{1}{2}}+\rho_e(k^2v_{Ae}^2-\omega^2)(m_i^2+\ell^2)^{\frac{1}{2}}=0, \tag{2.29}$$

where

$$m_i^2=\frac{(k^2c_{Si}^2-\omega^2)(k^2v_{Ai}^2-\omega^2)}{(c_{Si}^2+v_{Ai}^2)(k^2c_{Ti}^2-\omega^2)} \tag{2.30}$$

$$m_e^2=\frac{(k^2c_{Se}^2-\omega^2)(k^2v_{Ae}^2-\omega^2)}{(c_{Se}^2+v_{Ae}^2)(k^2c_{Te}^2-\omega^2)} \tag{2.31}$$

are the two magnetoacoustic parameters, and

$$c_{Ti}^2=\frac{c_{Si}^2v_{Ai}^2}{c_{Si}^2+v_{Ai}^2}, \quad c_{Te}^2=\frac{c_{Se}^2v_{Ae}^2}{c_{Se}^2+v_{Ae}^2} \tag{2.32}$$

are the two tube (cusp) speeds. In Equation (2.29) k and ℓ are the components of the wavevector along the x and y directions and the indices i and e refer to the two regions.

Roberts (1981a) found that the interface supports the propagation of two surface waves (slow and fast surface waves), however, the slow surface wave will propagate only when one region is field-free. In the case of the slow surface wave, the phase speed is in the range $v_{ph} < min(c_{Se}, c_{Ti})$. On the other hand, the propagation of the fast surface wave may occur when the fluid in the magnetic region is cooler than the field-free plasma. The range of phase speed for fast surface wave is $c_{Si} < v_{ph} < min(c_{Se}, v_{Ai})$.

2.3.2.2 Wave propagation in magnetic slab

Magnetic slabs can be considered as a pair of magnetic interfaces separated by a constant distance x_0, where the slab is parallel to the z-axis. It is well known that once we restrict the wave propagation by plasma structuring, the wave becomes dispersive and the degree dispersion is determined by the rel-

ative ratio between the size of the waveguide and the wavelength of waves. Although in real life we are not going to meet such a situation, it provides a natural extension to a single interface and qualitatively gives us the behaviour of waves in such structures. Parker (1979) discussed the propagation of waves in magnetic slabs in the limit of incompressible plasma. The effect of compressibility was considered later by Cram and Wilson (1975) and they concluded that the propagation of the fast wave is not a free vibration. Later, the study by Roberts (1981b) explained that the fast wave is not a free vibration only if the slab is warmer than its field free environment. Since we are dealing with two interfaces, similar boundary conditions have to be imposed as in the case of a single interface. Denoting the environment inside the slab by an index i and the external regions by an index e, the equilibrium state is described by

$$p_0(x), \rho_0(x), B_0(x) = \begin{cases} p_i, \rho_i, B_i, & |x| < x_0, \\ p_e, \rho_e, B_e, & |x| > x_0. \end{cases} \tag{2.33}$$

The continuity of the total pressure in equilibrium requires that

$$p_i + \frac{B_i^2}{2\mu_0} = p_e + \frac{B_e^2}{2\mu_0}. \tag{2.34}$$

Using the expressions of the sound speed and Alfvén speeds in the two regions, the above expression can be also written as

$$\frac{\rho_e}{\rho_i} = \frac{2c_{Si}^2 + \gamma v_{Ai}^2}{2c_{Se}^2 + \gamma v_{Ae}^2}. \tag{2.35}$$

Since the plasma is now separated into two uniform regions, the slab interior and its environment, different governing equations can be written for each region and the solutions of the governing equations must be matched at the boundaries of the slab.

Accordingly, inside the slab the equation describing the variation of the transversal component of the velocity becomes

$$\frac{d^2\hat{v}_x}{dx^2} - m_i^2\hat{v}_x = 0 \tag{2.36}$$

where the quantity m_i^2 has been defined earlier in equation (2.30). In addition, the relation that connects the total pressure $\hat{P}_T$ and the transversal component of the velocity becomes

$$\hat{P}_T = \frac{i\rho_i(c_{Si}^2 + v_{Ai}^2)}{\omega}\frac{k^2c_{Ti}^2 - \omega^2}{k^2c_{Si}^2 - \omega^2}\frac{d\hat{v}_x}{dx}. \tag{2.37}$$

A similar set of equations can be derived for the outside region ($x > |x_0|$) of the magnetic slab. All plasma quantities in this case will be indicated with an index e. Since waves are guided and propagate within the magnetic slab, it is natural to impose the condition that in the outside regions perturbations are evanescent.

As a result, the solutions for the transversal component of velocity becomes

$$\hat{v}_x(x) = \begin{cases} \alpha_e e^{-m_e(x-x_0)}, & x > x_0, \\ \alpha_i \cosh m_i x + \beta_i \sinh m_i x, & -x_0 < x < x_0, \\ \beta_e e^{m_e(x+x_0)}, & x < -x_0. \end{cases} \tag{2.38}$$

Where α_e, β_e, α_i and β_i are arbitrary constants that can be determined by imposing the boundary conditions at $x = \pm x_0$ and the expression of m_e which has been defined earlier. For laterally evanescent waves we require that m_e is a positive quantity.

After imposing the continuity of the transversal component of velocity and total pressure at the boundaries of the waveguide, the dispersion relation in a magnetic slab becomes surrounded by a magnetic environment and can be

written as (Roberts, 1981b)

$$\rho_e(k^2v_{Ae}^2-\omega^2)m_i\left\{\begin{matrix}\tanh\\ \coth\end{matrix}\right\}m_ix_0+\rho_i(k^2v_{Ai}^2-\omega^2)m_e=0. \tag{2.39}$$

Before discussing the implications of this dispersion relation, we need to introduce the terminology that helps us classify the possible wave solutions of the dispersion relation. According to the criteria introduced by Roberts (1981a), solutions corresponding to $m_i^2 > 0$ and $m_i^2 < 0$ correspond to surface and body waves, respectively. This classification is connected to the type of the behaviour of modes inside the waveguide. Surface modes are evanescent inside the slab and attain their maximum amplitude at the boundary of the slab (see Fig. 2.2(b)). In contrast, body waves are oscillatory inside the slab (see Fig. 2.2(c)). A further classification arises from the even (tanh) and odd

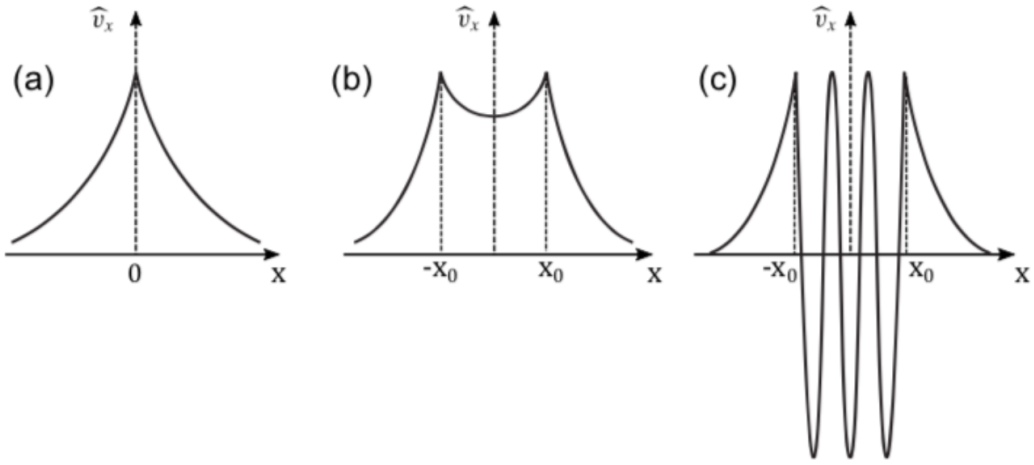

Figure 2.2: A schematic representation of the distribution of the velocity amplitude for (a) guided waves along an interface; (b) surface waves in a slab; and (c) body waves in a slab. Imaged adapted from Priest (2014).

(coth) solutions of (2.39) that are referred to as sausage and kink oscillations respectively (see Fig. 2.3). Sausage modes (often called symmetric or pulsating) propagate such that the symmetry axis of the slab is not perturbed. In contrast, kink modes oscillate such that the symmetry axis is oscillating. A

schematic representation of these waves is shown in Figure 2.3. The relative

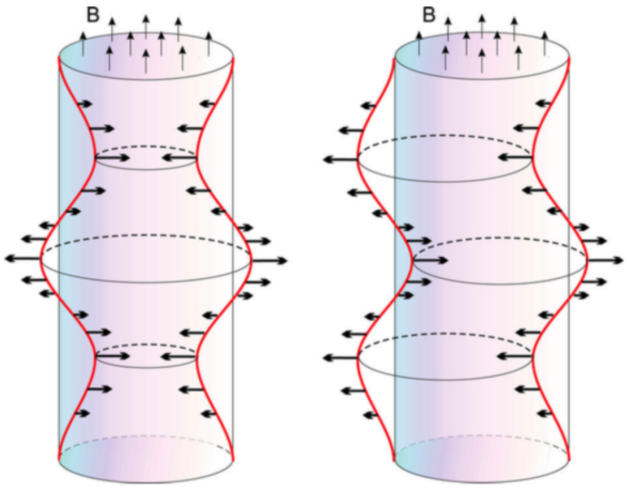

Figure 2.3: The longitudinal (sausage, left panel) and transversal (kink, right panel) modes propagating along a cylindrical magnetic waveguide are shown with red lines. The sausage wave is characterised by periodic stretching and squeezing of the magnetic field, while the kink wave corresponds to a displacement of the symmetry axis magnetic flux tube. The thick arrows represent the amplitudes of the velocity perturbations, while the thin arrows represent the direction of the background magnetic field. Image taken from Morton et al. (2012)

relationship between the characteristic speeds inside and outside the slab will determine whether the wave will be a slow or fast wave. The solutions of the dispersion relation (2.39) are represented in Figure 2.4 for photospheric conditions ($\beta \gg 1$) and coronal ($\beta \ll 1$) conditions, respectively. According to the dispersion diagrams, fast waves are strongly dispersive and propagate slower for smaller wavelengths. Slow waves, in turn, are dispersive and these waves will propagate faster for smaller wavelengths. There are a few important conclusions that can be drawn from the dispersion relation (2.39). First of all, surface waves ($m_i^2 > 0$) appear only when the phase speed of waves (ω/k) lies between the two Alfvén speeds, i.e. $min(v_{Ai}, v_{Ae}) < \omega/k < max(v_{Ai}, v_{Ae})$.

Since we are interested in laterally evanescent solutions, the requirement that $m_e^2 > 0$ implies that (see Equation 2.31) the possible phase speed has to be either smaller than the external cusp speed, c_{Te}, or situated in the interval

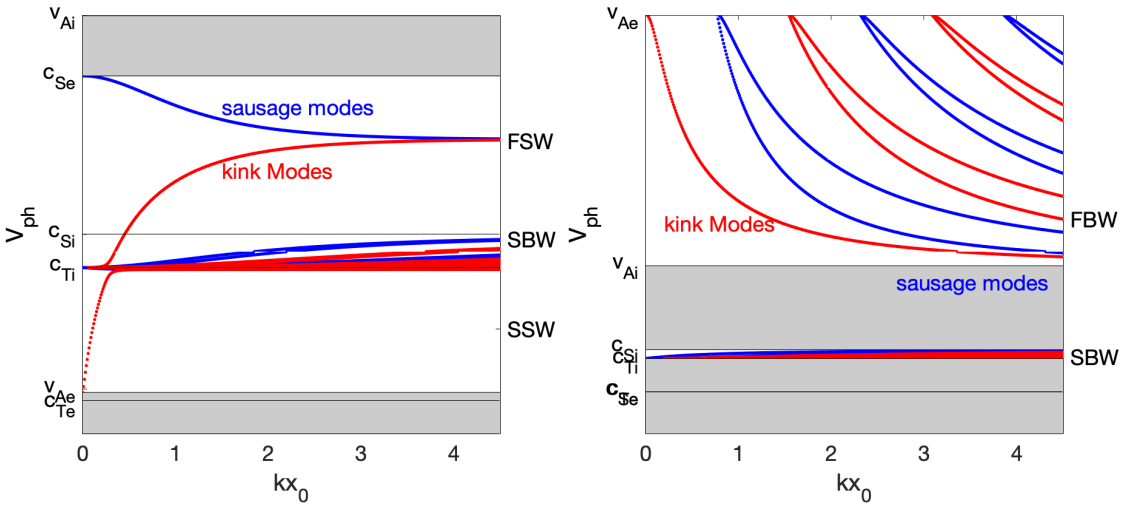

Figure 2.4: The solution of the dispersion relation for magnetic slab under photospheric (left panel) and coronal (right panel) condition. SSW, FSW, SBW and FBW stand for slow surface waves, fast surface waves, slow body waves, fast body waves, respectively. The grey regions correspond to domains where waves cannot propagate.

$min(v_{Ae}, c_{Se}) < \omega/k < max(v_{Ae}, c_{Se})$.

Furthermore, the dispersion relation (2.39) reveals that although $\omega/k = \pm v_{Ae}$ and $\omega/k = \pm v_{Ai}$ are solutions of the dispersion relation, these are degenerate solutions, since such a choice for the phase speed results in vanishing eigenvectors. The same degeneracy of the system can be obtained when $c_{Si} = c_{Se}$ (in which case pure sound waves propagate without disturbing the magnetic field), or when $v_{Ae} = v_{Ai}$ (Roberts, 1981b).

One way to simplify the dispersion relation (2.39) is to consider the limits is slender or wide waveguide. These limits correspond to the conditions that the wavelength of any disturbance is much greater (or much smaller) than the transversal geometrical size of the slab, i.e. $|kx_0| \ll 1$ and $|kx_0| \gg 1$, respectively (in fluid mechanics these conditions correspond to the cases of shallow and deep water limits). In these situations the hyperbolic functions in the dispersion relation take simpler forms, meaning that analytical expressions can be derived for the frequency of waves.

2.3.2.3 Wave propagation in a magnetic cylinder

Modelling a magnetic structure in a cylindrical geometry is certainly more appropriate for many applications in solar physics, for example, for photospheric flux tubes (including vortices) and coronal loops. In solar physics, there have been several investigations of dynamics in cylindrical waveguides (Roberts and Webb, 1978; Wilson, 1979; Roberts and Webb, 1979; Parker, 1979; Wentzel, 1979; Webb, 1980; Spruit, 1981, 1982; Edwin and Roberts, 1983) which provided a complex array of waves in such media. In this Thesis we are going to present the key findings of the study by Edwin and Roberts (1983).

Let us consider that the plasma is permeated by a homogeneous magnetic field inside and outside the magnetic flux tube and the magnetic field is oriented along the longitudinal axis of the cylinder, i.e. $\mathbf{B}_i = B_i\hat{z}$ and $\mathbf{B}_e\hat{z} = B_e\hat{z}$. The discontinuity occurs at the boundary of the tube situated at $r = r_a$, where r_a is the radius of the magnetic flux tube.

The plasma in equilibrium state is considered homogeneous and, as before, the quantities inside the flux tube will be labelled by an index i, while quantities outside the flux tube will be described by the index e.

Using the linearised equations presented in Section 2.3.1.2, we can derive a single equation that describes the temporal and spatial evolution of the compressibility in cylindrical geometry (Lighthill, 1960; Cowling, 1976; Roberts, 1981a; Aschwanden, 2006)

$$\frac{\partial^4 \Delta}{\partial t^4} - (c_S^2 + v_A^2)\frac{\partial^2}{\partial t^2}\nabla^2\Delta + c_S^2 v_A^2 \frac{\partial^2}{\partial z^2}\nabla^2\Delta = 0, \tag{2.40}$$

where $\Delta = \nabla \cdot \mathbf{v}$ is the compressibility of the plasma and the Laplace operator is expressed in the cylindrical coordinate system (r, θ, z) as

$$\nabla^2 = \frac{\partial^2}{\partial r^2} + \frac{1}{r}\frac{\partial}{\partial r} + \frac{1}{r^2}\frac{\partial^2}{\partial \theta^2} + \frac{\partial^2}{\partial z^2}. \tag{2.41}$$

Since the equilibrium is homogeneous in the azimuthal and longitudinal direction,we can write that

$$\Delta = R(r)exp(\imath(\omega t + n\theta + kz)), \tag{2.42}$$

where n and k denote the wavenumber in the azimuthal and longitudinal directions, ω is the angular frequency, and $R(r)$ specifies the r-dependent amplitude of compressibility.

After plugging Equation (2.42) into Equation (2.40), we obtain

$$\frac{d^2R}{dr^2} + \frac{1}{r}\frac{dR}{dr} - (m_i^2 + \frac{n^2}{r^2})R = 0, \tag{2.43}$$

where the expression of m_i has been defined by Equation (2.30).

Equation (2.43) is a Bessel-type differential equation that admits solutions of the form

$$R(r) = \begin{cases} A_0 I_n(m_i r) + A_1 K_n(m_i r), & m_i^2 > 0, \\ A_0 J_n(n_i r) + A_1 Y_n(n_i r), & m_i^2 = -n_i^2 < 0. \end{cases} \tag{2.44}$$

where the constants A_0 and A_1 must be determined for each mode number n, I_n, K_n, J_n, and Y_n are Bessel functions. Clearly, a similar solution can be written for the external region.

Imposing the conditions that solutions are bounded at $r = 0$ and the variables are evanescent in the external region, solutions of the governing differential equation reduces to

$$R(r) = A_0 \begin{cases} I_n(m_i r), & m_i^2 > 0, \\ J_n(n_i r), & m_i^2 = -n_i^2 < 0. \end{cases} \tag{2.45}$$

for the inside region ($r < r_a$) and

$$R(r) = A_2 K_n(m_e r) \tag{2.46}$$

for the external region ($r > r_a$).

Applying similar boundary conditions as in the case of a magnetic slab (continuity of the total pressure and normal component of velocity) results in the dispersion relations (Edwin and Roberts, 1983)

$$\rho_i(k^2 v_{Ai}^2 - \omega^2) m_e \frac{K_n'(m_e r_a)}{K_n'(m_e r_a)} = \rho_e(k^2 v_{Ae}^2 - \omega^2) m_i \frac{I_n'(m_i r_a)}{I_n(m_i r_a)}, \tag{2.47}$$

for surface waves ($m_i^2 > 0$), and

$$\rho_i(k^2 v_{Ai}^2 - \omega^2) m_e \frac{K_n'(m_e r_a)}{K_n'(m_e r_a)} = \rho_e(k^2 v_{Ae}^2 - \omega^2) n_i \frac{J_n'(m_i r_a)}{J_n(m_i r_a)}, \tag{2.48}$$

for body waves ($m_i^2 = -n_i^2 < 0$). In the above expressions the dash denotes the derivatives of the Bessel functions with respect to their argument.

Based on the forms of the function R(r), the expressions of various variables can be given as (see, e.g Spruit (1982)),

$$v_z = -iA \frac{k c_S^2}{\omega^2} \Re_n, \tag{2.49}$$

$$v_r = A \frac{\omega^2 - k c_S^2}{\omega^2 m_i^2} \frac{d}{dr} \Re_n, \tag{2.50}$$

$$v_\theta = iA \frac{\omega^2 - k c_S^2}{\omega^2 m_i^2} \frac{n}{r} \Re_n, \tag{2.51}$$

$$b_z = iAB_i \frac{\omega^2 - k c_S^2}{\omega^3} \Re_n, \tag{2.52}$$

$$b_r = -B_i \frac{k}{\omega} v_r, \tag{2.53}$$

$$b_\theta = B_i \frac{k}{\omega} v_\theta, \tag{2.54}$$

$$p = iA\rho_i \frac{c_S^2}{\omega} \Re_n, \tag{2.55}$$

$$P_T = -i\frac{\rho_i}{\omega^3}(c_S^2 + v_A^2)(\omega^2 - k^2 c_T^2)\Re_n, \tag{2.56}$$

where A denotes an arbitrary amplitude, and $\Re_n$ is the corresponding Bessel function.

The dispersion relation admits a rich spectrum of MHD waves under the photospheric ($\beta \gg 1$) and coronal ($\beta \ll 1$) conditions. The variation of the phase velocity with the parameter kr_a given for these two limits is shown in Figure (2.5). For a slender tube $kr_a \to 0$ and it is assumed that in this limit

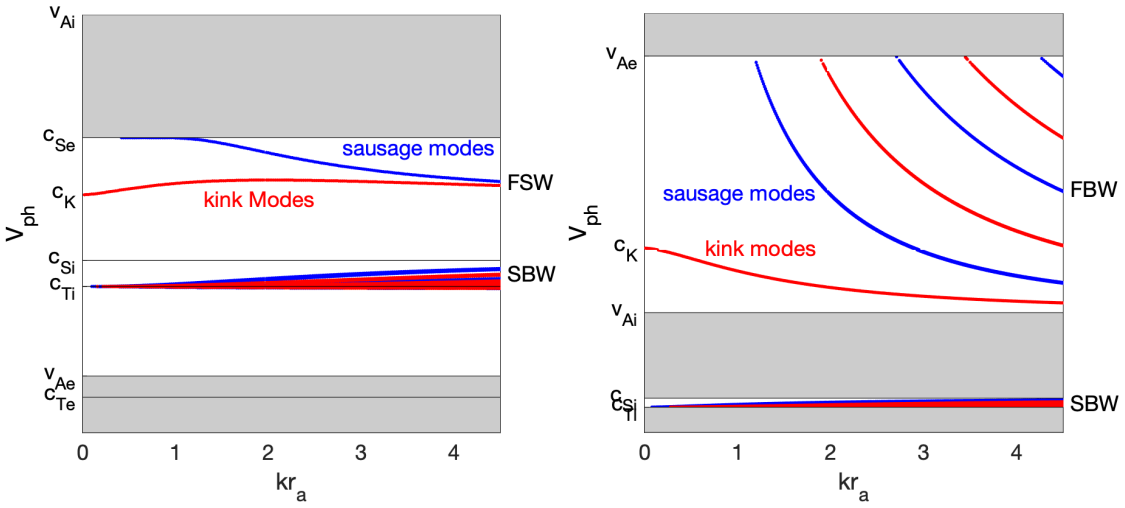

Figure 2.5: The same as in Figure 2.4, but here we plot the dispersion diagram of waves propagating in a magnetic cylinder of radius r_a.

both, $m_i r_a$ and $m_e r_a$, tend to zero. As a result the Bessel functions simplify to

$$I_0(m_i r_a) \sim 1, \quad I_1(m_i r_a) \sim \frac{1}{2} m_i r_a, \tag{2.57}$$

$$K_0(m_e r_a) \sim \ln(m_e r_a), \quad K_1(m_e r_a) \sim (m_e r_a)^{-1}. \tag{2.58}$$

In this case the dispersion relation for surface waves becomes

$$\frac{\rho_e r_a^2}{4}(k^2 v_{Ae}^2 - \omega^2)(k^2 c_{Si}^2 - \omega^2)\ln(m_e^2 r_a^2) = \rho_i (c_{Si}^2 + v_{Ai}^2)(k^2 c_{Ti}^2 - \omega^2). \tag{2.59}$$

This equation gives rise to two symmetric modes that have the approximative phase velocity

$$\frac{\omega}{k} \approx \left[c_{Ti}^2 - \frac{\rho_e (v_{Ae}^2 - c_{Ti}^2)(c_{Si}^2 - c_{Ti}^2) k^2 r_a^2 \ln(k^2 r_a^2)}{4\rho_i (c_{Si}^2 + v_{Ai}^2) c_{Ti}^2} \right]^{1/2}, \tag{2.60}$$

and

$$\frac{\omega}{k} \approx \left\{ c_e^2 - \frac{(c_{Te}^2 - c_{Se}^2)(c_{Se}^2 + v_{Ae}^2)}{k^2 r_a^2 (v_{Ae}^2 - c_{Se}^2)} \exp\left[- \frac{4\rho_i (c_{Si}^2 + v_{Ai}^2)(c_{Se}^2 - c_{Ti}^2)}{\rho_e k^2 r_a^2 (c_{Se}^2 - v_{Ae}^2)(c_{Se}^2 - c_{Si}^2)} \right] \right\}^{1/2}, \tag{2.61}$$

which are valid provided $c_{Se} > c_{Si}$ and $c_{Se} > v_{Ae}$ or $c_{Ti} < c_{Se} < c_{Si}$ and $c_{Se} < v_{Ae}$. These relations show that for a slender slab symmetric modes propagate with almost identical phase speeds as their counterparts in magnetic slabs, i.e. sausage modes propagate with the phase speeds close to c_{Ti} and c_{Se}, respectively.

In contrast, kink modes present a different behaviour. For illustrative purposes we are going to concentrate only on the $n = 1$ case, and the above statement can be shown to be true for the $n \geq 1$ modes. When $n = 1$ we can consider that $m_i r_a \to 0$ and $m_e r_a \to 0$, so the dispersion relation reduces to

$$\frac{\omega}{k} = c_K \approx \left(\frac{\rho_i v_{Ai}^2 + \rho_e v_{Ae}^2}{\rho_i + \rho_e} \right)^{1/2}. \tag{2.62}$$

Kink waves have played a key role in seismological methods developed in the last decades (Aschwanden et al., 1999; Nakariakov et al., 1999; Arregui et al., 2005, 2007; Pascoe, 2014). When the radius of the cylinder is large compared to the wavelength of waves, we are dealing with a wide tube and the dispersion relation for both sausage and kink modes becomes

$$\rho_i m_e (k^2 v_{Ai}^2 - \omega^2) + \rho_e m_i (k^2 v_{Ae}^2 - \omega^2) = 0. \tag{2.63}$$

This dispersion equation is similar to the dispersion relation we would obtain in a wide slab or a single interface (this conclusion is rather normal since for wide waveguides the waves would not sense the boundary of the tube, therefore, they will become non-dispersive).

In the case of body modes propagating in a slender magnetic cylinder it can be shown that the only possible way to obtain waves is by supposing that when $kr_a \to 0$ corresponds to $n_i r_a \to \nu$, a non-zero finite value. For $n_i r_a J_1(n_i r_a)$ to be finite, $n_i r_a$ must tend to the roots of $J_1(n_i r_a) = 0$, i.e. $n_i r_a \to j_q$, for $q = 1, 2, \ldots$, and j_q denotes the zeroes of the Bessel function J_1. As a result

$$n_i^2 r_a^2 \approx \frac{k^2(c_{Si}^2 - c_{Ti}^2)(v_{Ai}^2 - c_{Ti}^2)r_a^2}{(c_{Si}^2 + v_{Ai}^2)c_{Ti}^2\nu} = j_q^2 \tag{2.64}$$

and the modes corresponding to $kr_a \ll 1$ are given by

$$\frac{\omega}{k} \approx c_{Ti}\left[1 + \frac{k^2 r_a^2 c_{Ti}^2}{(c_{Si}^2 + v_{Ai}^2)j_q^2}\right]^{1/2}, \quad q = 1, 2, \ldots \tag{2.65}$$

Therefore in a slender tube there are an infinite number of modes given by Equation (2.65).

In the case of body kink modes the dispersion relation reduces to the dispersion relation given by Equation (2.63), therefore in a slender tube the body and surface kink modes are indistinguishable, i.e. they are independent on m_i and/or n_i.

Finally, in a wide tube the solutions of the dispersion relation for sausage modes are given by

$$\tan(n_i r_a - \pi/4) = \frac{\rho_i(k^2 v_{Ai}^2 - \omega^2)}{\rho_e(k^2 v_{Ae}^2 - \omega^2)}\frac{m_e}{n_i}, \tag{2.66}$$

while kink modes are characteristics of kink modes can be recovered as solu-

tions of the relation

$$\tan(n_i r_a - \pi/4) = -\frac{\rho_e(k^2 v_{Ae}^2 - \omega^2)}{\rho_i(k^2 v_{Ai}^2 - \omega^2)} \frac{n_i}{m_e}, \tag{2.67}$$

2.3.3 Numerical method for solving dispersion relations

Since the dispersion relation presented earlier contains hyperbolic or Bessel functions, a closed analytical solution can be obtained only for the particular limits of slender and wide waveguides. However, these limits do not cover the whole spectrum of solutions. That is why solutions of dispersion relations have to be obtained using a numerical approach. As an illustration we will present the numerical steps undertaken to study the solutions of the dispersion relation (2.39), describing the propagation of waves in a magnetic slab.

The solutions of the dispersion relations have been obtained graphically after solving numerically these relations using the bisection method. For illustration we describe the method for a magnetic slab and the method necessary to plot the solution of the dispersion relation for a magnetic cylinder would be analogous.

First of all, we rewrite Equation (2.39) in terms of the phase speed and normalizing the phase speed with the internal sound speed

$$\rho_e \left(\frac{v_{Ae}^2}{c_{Si}^2} - V^2 \right) \tilde{m}_i \left\{ \begin{matrix} \tanh \\ \coth \end{matrix} \right\} (\tilde{m}_i k x_i) + \rho_i \left(\frac{v_{Ai}^2}{c_{Si}^2} - V^2 \right) \tilde{m}_e = 0, \tag{2.68}$$

where the normalised magnetoacoustic parameters are

$$\tilde{m}_i = \sqrt{\frac{(k^2 - \frac{\omega^2}{c_{Si}}) - (k^2 V^2 - \frac{\omega^2}{c_{Si}^2})}{(1+V^2)(\frac{k^2 c_{Ti}^2}{c_{Si}^2} - \frac{\omega^2}{c_{Si}^2})}}, \tag{2.69}$$

$$\tilde{m}_e = \sqrt{\frac{(k^2 - \frac{\omega^2}{c_{Si}}) - (k^2V^2 - \frac{\omega^2}{c_{Si}^2})}{(\frac{c_{Se}^2}{c_{Si}^2} + V^2)(\frac{k^2c_{Te}^2}{c_{Si}^2} - \frac{\omega^2}{c_{Si}^2})}}. \tag{2.70}$$

Here $V = v_{ph}/c_i$ is normalized phase speed with the internal sound speed. Next, we divide the normalized phase speeds into small subintervals, each with a lower and upper boundaries, denoted by V_{L_i}, V_{U_i}. The range of the wavenumber (displayed on the horizontal axis) is also discretised and it is denoted by kx_i. Table 2.1 explains how the method works.

Table 2.1: The numerical background used to find solutions to the dispersion relation of guided waves.

kx_i	V_{L_i}	$V_{U_i} = V_{L_i} + \epsilon$	$F_i(V_{L_i}, kx_i)$	$F_i(V_{U_i}, kx_i)$	$F_i(V_{L_i}, kx_i) * F_i(V_{U_i}, kx_i)$
kx_1	V_{L_1}	V_{U_1}	$F_1(V_{L_1}, kx_1)$	$F_1(V_{U_1}, kx_1)$	$F_1(V_{L_1}, kx_1) * F_1(V_{U_1}, kx_1)$
kx_1	V_{L_2}	V_{U_2}	$F_2(V_{L_2}, kx_1)$	$F_2(V_{U_2}, kx_1)$	$F_2(V_{L_1}, kx_1) * F_2(V_{U_1}, kx_1)$
kx_1	V_{L_3}	V_{U_3}	$F_3(V_{L_3}, kx_1)$	$F_3(V_{U_3}, kx_1)$	$F_3(V_{L_3}, kx_1) * F_3(V_{U_3}, kx_1)$
$\vdots$	$\vdots$	$\vdots$	$\vdots$	$\vdots$	$\vdots$
kx_2	V_{L_1}	V_{U_1}	$F_1(V_{L_1}, kx_2)$	$F_1(V_{U_1}, kx_2)$	$F_1(V_{L_1}, kx_2) * F_1(V_{U_1}, kx_2)$
kx_2	V_{L_2}	V_{U_2}	$F_2(V_{L_2}, kx_2)$	$F_2(V_{U_2}, kx_2)$	$F_2(V_{L_2}, kx_2) * F_2(V_{U_2}, kx_2)$
$\vdots$	$\vdots$	$\vdots$	$\vdots$	$\vdots$	$\vdots$
kx_3	V_{L_1}	V_{U_1}	$F_1(V_{L_1}, kx_3)$	$F_1(V_{U_1}, kx_3)$	$F_1(V_{L_1}, kx_3) * F_1(V_{U_1}, kx_3)$
$\vdots$	$\vdots$	$\vdots$	$\vdots$	$\vdots$	$\vdots$
$\vdots$	$\vdots$	$\vdots$	$\vdots$	$\vdots$	$\vdots$

Here ϵ is the small distance between $V_{L_i}$and V_{U_i} (stepsize) and F is a function of two variables from Equation 2.68. We consider only the results that satisfy the condition $F_i(V_L, kx) * F_i(V_U, kx) < 0$.

The above numerical technique is applied to the dispersion relation of the magnetic slab (see Equation 2.39) and magnetic cylinder (Equations 2.47 and 2.48) under photospheric and coronal conditions. The results of these investigations are shown in Figures 2.4 and 2.5.

Waves propagating in a homogeneous and unstructured plasma presented in Section 2.3.1.2 are very different from the waves that can propagate in geometrically defined waveguides. First of all the fact that waves are restricted to propagate in waveguides, renders waves to be dispersive, i.e. their phase

speeds depends on the wavlength (or wavenumber) of the waves. Figures 2.4 and 2.5 reveal that fast waves are strongly dispersive (negative dispersion), while slow waves have a weak dispersion (positive dispersion). Kink modes under photospheric conditions show a somehow different behaviour. All modes will become non-dispersive for wide structures, as shown by Equation 2.63. Guided waves will also be characterised by their transversal structure and the way they perturb the symmetry axis of the waveguide. A full picture on the behaviour of these modes can be obtained by plotting the eigenvectors, in particular the components of the velocity. For illustration we will consider the cylindrical flux tube model and we plot the values of the velocity components as given by Equation 2.56 and here we focus on the characteristics of fast surface sausage, kink and fluting ($n = 2$) modes (see Figures 2.6, 2.7 and 2.8).

The characteristic speeds we employ for this simulation are $v_{Ai} = 2c_{Si}$, $c_{Se} = 1.5c_{Si}$, and $v_{Ae} = 0.5c_{Si}$. Later, in Chapter 4 we will use the combination of these three modes to study the morphology of global waves propagating in vortex tubes and apply the Proper Orthogonal Decomposition (POD) technique for mode identification.

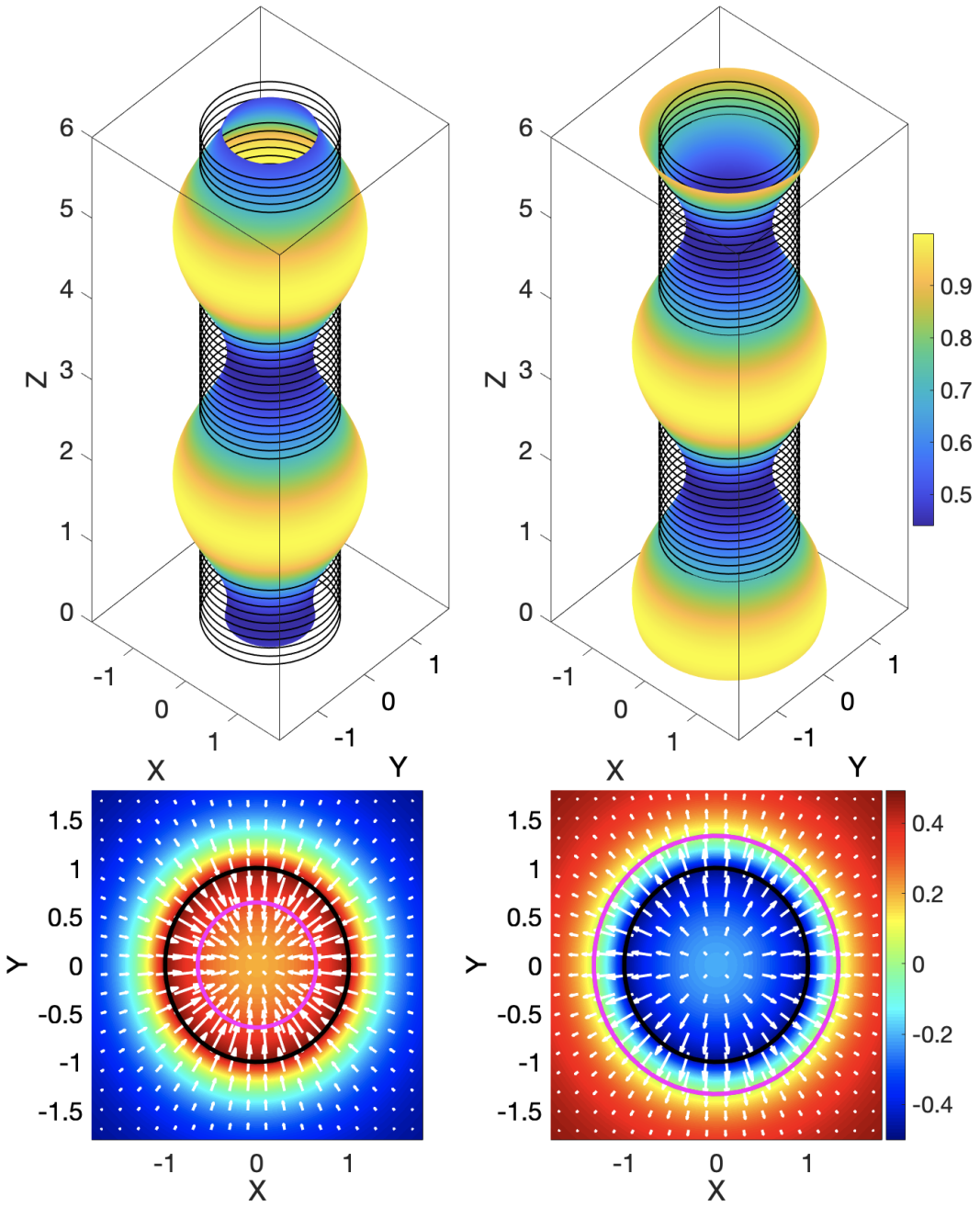

Figure 2.6: The sausage mode ($n = 0$) propagating along the magnetic cylinder. The first row is the 3D representation of the oscillating flux tube and the colormap values represent the distance between the cylinder's centre and its boundaries at each height. The second row displays the cross cut across the flux tube at $z = 0$. The white arrows describe the velocity perturbations and the colour bar shows the density perturbation. In the second row, a positive density disturbance is indicated by warmer colours, with red signifying the maximum. Negative density perturbations are displayed by cooler colours, with blue denoting the lowest. The black line shows the cross section of the unperturbed flux tube of radius 1 and the pink line denotes the contour of the flux tube in the presence of perturbations.

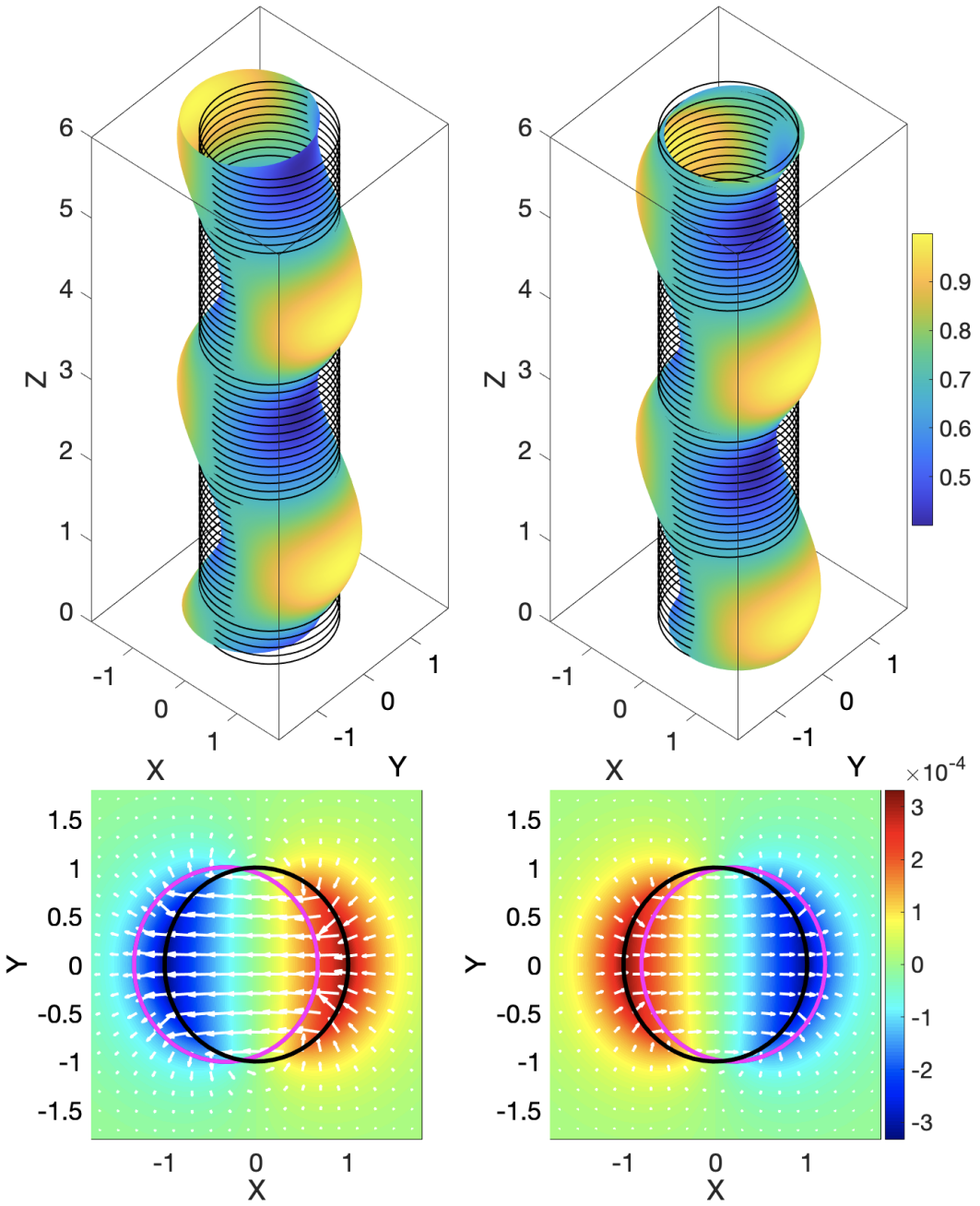

Figure 2.7: The same as Figure 2.6, but here we represent the propagation of kink modes ($n = 1$).

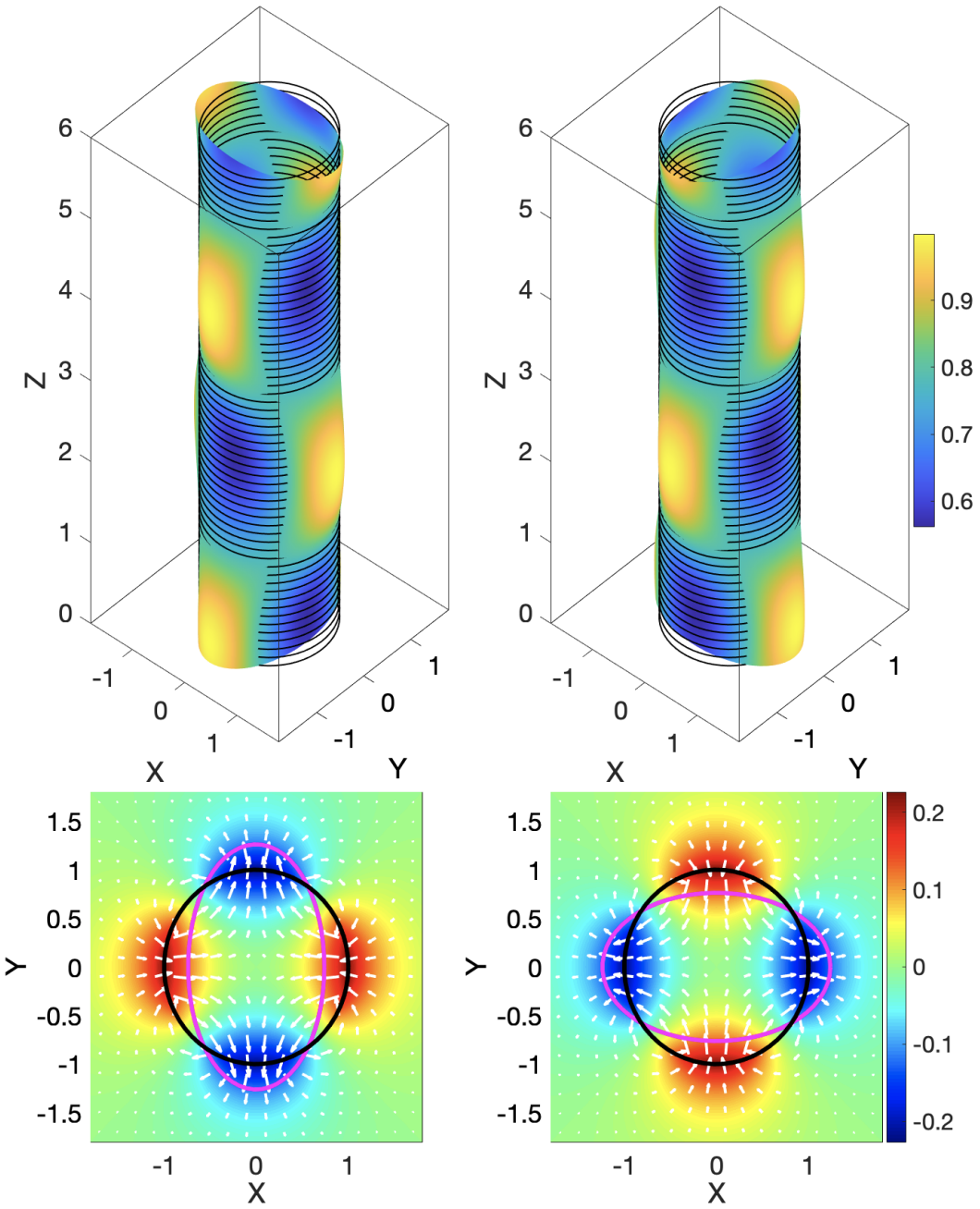

Figure 2.8: The same as Figure 2.6, but here show the propagation of the the fluting mode ($n = 2$).

CHAPTER 3

New approach for analysing dynamical processes on the surface of photospheric vortex tubes [1]

3.1 Introduction

A number of modern space- and ground-based observational facilities, e.g. SDO, Hinode, Solar Orbiter, SST, DST, DKIST allow us to obtain key information about various plasma flow and wave processes at different time and spatial scales in the solar atmosphere. This solar region is permeated by the magnetic field generated in the solar interior, and advected to the surface by convective motions. The magnetic field is not distributed uniformly, instead it accumulates in various structures differentiated by their transverse size, lifetime, location, etc. The photospheric plasma layer presents a rich spectrum of dynamics and classes of flows of all spatial and temporal scales. In particular, a key feature of photospheric plasma flows is the vortex motions. Using high-quality series of granulation images taken with the SST, Brandt et al. (1988) evidenced vortex structures which visibly dominated the motion of the granules in their neighbourhood. They found that the average lifetime of such structures is about 90 minutes. It was also suggested that such vortices, being common feature of the solar convective zone, can provide an important mechanism for the heating of stellar chromospheres and coronae by twisting the footprints of magnetic flux tubes. Later, Bonet et al. (2008), based on

[1] This Chapter is based on a research that is published in The Astrophysical Journal.

the motion of bright points determined that the vortices observed in the solar photosphere appear in regions of cooled plasma downflows and they can trace well the supergranulation and the mesogranulation. They also found that the density of vortices on the solar disk is approximately 0.9×10^{-2} vortices per Mm^2.

Various vortices in the solar atmosphere have been observed in a wide range of temporal and spatial scales, from granular (e.g. 0.1-1 Mm in diameter, Giagkiozis et al., 2018) to meso- and supergranular scales (e.g. 5-10 Mm in diameter, Bonet et al., 2010; Requerey et al., 2018; Chian et al., 2019). Depending on the analysed scale, vortices will display different lifetimes. For granular scales, Giagkiozis et al. (2018) applied Fourier Local Correlation Tracking (FLCT) (Fisher and Welsch, 2008) to intensity maps and obtained a lifetime around 16.5 s and maximum duration around 100 s. In contrast, supergranular vortices can last for a couple of hours (Requerey et al., 2018; Chian et al., 2019, 2020).

In the photosphere, the evolution of magnetic elements that co-exist with rotational motion is strongly correlated with those vortices which act to stabilize the magnetic flux (Requerey et al., 2018). Recently, Shetye et al. (2019) suggested that the chromospheric swirl is a flux tube that extends above a magnetic concentration region in the photosphere. This idea is in accordance with the scenario proposed by Wedemeyer-Böhm et al. (2012), where the chromospheric swirls and the photospheric vortices are part of the same solar vortex tube. In the chromosphere, the swirls have a lifetime around 200-300 s (Tziotziou et al., 2018) and are dominated by transverse and rotational motions (Tziotziou et al., 2019).

Solar vortex tubes can be spontaneously generated by turbulent convection. In simulations of quiet Sun regions vortices are found along intergranular lanes (Shelyag et al., 2011a; Kitiashvili et al., 2012; Moll et al., 2012; Silva et al.,

2020). They have an average lifetime of around 80 s (Silva et al., 2021) and a radius between 40 and 80 km Shelyag et al. (2013); Silva et al. (2020). Solar kinetic vortex tubes (Silva et al., 2021) act as a sink for magnetic field, creating magnetic flux tubes that expand with height (Kitiashvili et al., 2012; Moll et al., 2012; Silva et al., 2020). The concentration of magnetic flux leads to a high magnetic field tension, which can prevent the magnetic field lines to be twisted by the rotational motion (Shelyag et al., 2011b; Moll et al., 2012; Nelson et al., 2013; Silva et al., 2021). In some cases, twisted magnetic flux tubes appear close enough to flow vortices, leading to magnetic and kinetic vortex structures closely co-existing in regions with high plasma-β (Wedemeyer and Steiner, 2014; Rappazzo et al., 2019; Silva et al., 2021). The vortical motions can still trigger perturbations along magnetic lines that could lead to wave excitation, e.g. Battaglia et al. (2021a). The vorticity evolution in the magnetised solar atmosphere is mainly ruled by the magnetic field, which also influences the general shape of the vortices (Shelyag et al., 2011a). Based on the analysis of swirling strength, the part of the vorticity only linked to swirling motion (Shelyag et al., 2011b; Canivete Cuissa and Steiner, 2020) showed that the magnetic terms in the swirling equation evolution tend to cancel the hydrodynamic terms close to the solar surface, whereas the magnetic terms dominate alone the production of swirling motion in the chromosphere. The magnetic field also tends to have an important role in the plasma dynamics along the whole vortex tube, as the Lorentz force has a magnitude comparable to the pressure gradient (Silva et al., 2020; Kitiashvili et al., 2013). High-speed flow jets have also been linked to simulated vortex tubes, driven by high-pressure gradients close to the photosphere and by Lorentz force in the weakly magnetised upper solar photosphere (Kitiashvili et al., 2013). In general, the averaged radial profile of magnetic field, angular velocity, pressure gradient inside of the vortex tube at the lower chromosphere and photosphere levels

show similar behaviour (Silva et al., 2020).

There are several methods that can be used for vortex identification and analysis in fluid flows, e.g. Günther and Theisel (2018). However, in solar physics most of the previous analysis of vortices in the solar atmosphere were based on visual inspection. Automated methods were first applied in the analysis of solar vortices by Moll et al. (2012). Authors applied the vorticity strength method (Zhou et al., 1999), to identify the area dominated by vortex plasma flows in simulated quiet Sun and solar plage regions. Another vortex identification technique is the Γ-method, which is able to define both the vortex centre and boundary, and has been used to identify vortices in observational solar data (Giagkiozis et al., 2018). However, one of the stumbling blocks of the Γ-method is that it carries out the identification based on the topology of the streamlines of velocity fields, which are not an objective quantity (Haller et al., 2016). In other words, the Γ-method is not invariant under time-dependent rotations and translations of the reference frame. This may lead to false vortex detection (see, e.g. Silva et al., 2018) as well as high dependence on corrections made to remove satellite motion from observational data (Günther and Theisel, 2018). Further discussions on the importance of objectivity for vortex identification and description of flow topology can be found in (Haller et al., 2016).

The analysis of solar vortices in simulated solar atmosphere data tends to be bi-dimensional due to the limitations of the applied techniques. Silva et al. (2020) introduced a new methodology to define a 3D vortex based on the Instantaneous Vorticity Deviation (IVD), see e.g. Haller et al. (2016), allowing automated detection of boundary and centre of vortex tubes. In this chapter, we used the method of Lagrangian Averaged Vorticity Deviation (LAVD) developed by Haller et al. (2016) to identify vortex flows, namely the centre of circulation and their boundary. While the IVD implies an instantaneous field,

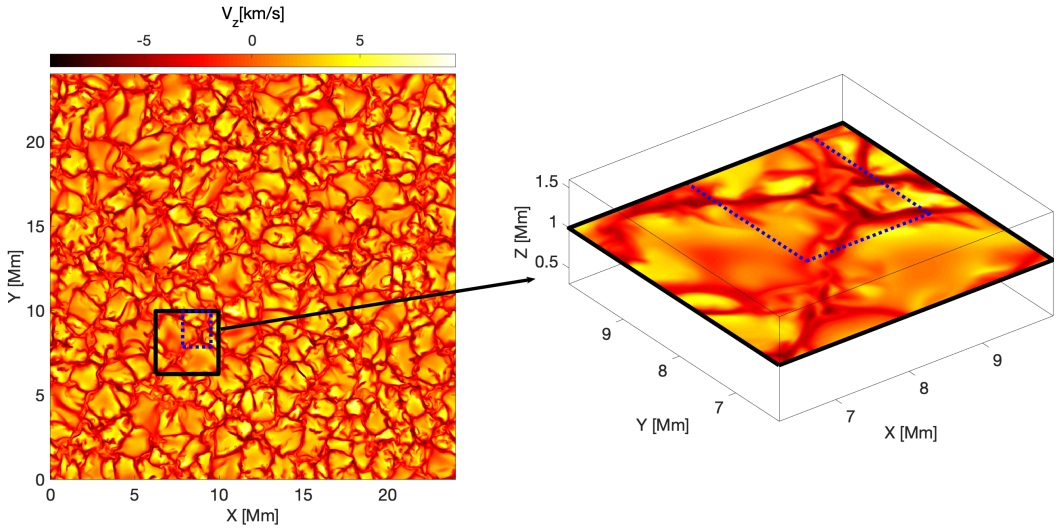

Figure 3.1: The analysed region of the simulation. Left panel: the xy-plane of the whole simulation domain at $z = 1.0$ Mm colored by the z-component of the velocity. The selected part of the domain investigated in this paper is delimited by black square. The blue-dotted square delimits the region used to plot 3D and 2D images of the domain. Right panel: 3D view of the selected part within the black square shown in the left panel.

the LAVD is calculated by advecting and following the particles. Although they are both based on vorticity deviation, they are distinct methodologies that provide the vortex boundary. The choice for the use of instantaneous or lagrangian approaches depends on the goal of the study. Here we focus on the understanding of the evolution of plasma dynamics at the vortex boundary and, therefore, LAVD field is more appropriate for the analysis, as IVD only provides the information about a given time frame and does not take into account the motion of the particles. Haller et al. (2016) compared these two methods and they found that IVD tends to under- or overestimate the size of the vortex at the initial time of the LAVD calculation. IVD also tends to detect short-lived structures, which are not as interesting as long lived ones and fails to determine part of the regions that belong to the true vortex during the time of the analysis.

The LAVD method is applied in conjunction with MURaM magneto-convection simulation data to detect and track the evolution of 3D vortex tubes in the so-

lar photosphere. Chapter 3 is organized as follow: in Section 2 we describe the numerical data, introduce the LAVD technique, explain the isosurface methodology to obtain the vortex tube and present the procedure to project the irregular vortex surface onto the envelope grid. Our analysis of the evolution of plasma variables at the vortex surface is presented in the Section 3. Finally our results are discussed and conclusions are drawn in Section 4.

3.2 Methodology

3.2.1 MURaM Simulation Data

MURaM (MPS - University of Chicago Radiative MHD, Vögler et al., 2005) is a multidimensional MHD code designed to realistically model solar magneto-convection and other related solar photospheric magnetic phenomena, such as pores (Cameron et al., 2007), sunspots (Rempel et al., 2009), and flux emergence (Cheung et al., 2007). The code has been used extensively in conjunction with simulated radiative diagnostics to explain a variety of small-scale photospheric phenomena, such as photospheric magnetic bright points (Shelyag et al., 2004), photospheric absorption line profile shapes and asymmetries (Khomenko et al., 2005; Shelyag et al., 2007), analyse flow structures in photospheric magnetic reconnection (Shelyag et al., 2018) and provide a link between photospheric reconnection events and Ellerman bombs (Nelson et al., 2013). MURaM simulations have also been used to analyse the role of torsional motions in the solar atmospheric energy balance (Shelyag et al., 2011b, 2012, 2013; Yadav et al., 2020, 2021) and in analysis of physics and structure of photospheric vortical flows (Shelyag et al., 2011a; Silva et al., 2020, 2021).

The code has been set up as follows: the size of the computational domain in Cartesian geometry is set to 24 Mm in the x and y directions and 1.6 Mm in the z direction. The spatial domain is resolved by $960 \times 960 \times 160$

grid cells in x, y, and z directions, respectively. The continuum radiation formation layer (simulated visible "solar surface") is located approximately at $z = 1$ Mm above the bottom boundary, which is made transparent for in- and outflows. Located at the temperature minimum, the upper boundary is closed and allows for the horizontal motion of plasma and magnetic field lines. The lateral boundaries of the simulation box have periodic conditions imposed. The total mass is controlled through correcting the inflow total pressure, deviation of which from the value of pressure at the previous timestep is based on the deviation of the current total mass box from the model, which results in an inflow density change (see Vögler et al., 2005, for more details). On the other hand, the upper boundary allows for horizontal motions and is located in the higher photosphere, where the density is very low. Therefore, partial reflections from the upper boundary will have only a very small influence on the lower-photospheric layers of the computational domain.

The simulation starts from a well-developed non-magnetic photospheric convection snapshot, where a uniform vertical magnetic field with the strength of 200 G is introduced. The physical reason to choose a uniform vertical magnetic field is because it is divergence and current-free and will therefore not perturb the non-magnetic convection model when it is introduced. Then, it is advected into intergranular lanes by photospheric flows, and after one granulation lifetime the initial uniformity vanishes. After the magnetic field collapses into the intergranular lanes, the magnetic field concentrations with the strength around 1.5 kG in the photosphere are formed. Then, a series of snapshots, containing state vectors of plasma parameters for each of the grid cells in the domain, are recorded with the cadence of approximately 3.6 s. The simulation run contains 120 snapshots, covering roughly 400 seconds of real physical time, corresponding to one granular turnover time.

Figure 3.1 displays the xy-view of the domain for an xy-plane placed at

$z = 1.0$ Mm and colored by the vertical component of the velocity field. Our analysis is focused on a region located between $x, y = 6.2...9.6$ Mm, indicated by the black square. This region extends from the simulated surface, $z = 1.0$ Mm, to the lower chromosphere, $z = 1.6$ Mm and comprises $150 \times 150 \times 60$ grid cells in x, y, and z directions, respectively. The square marked with blue dots is located at $x, y = 7.8...9.6$ Mm and represents the part of the domain used to produce zoom-on view of our results.

3.2.2 Vortex identification

In this section, we describe the vortex identification in three dimensions based on a sequence of time frames (119 snapshots), for the velocity field provided by the MURaM simulations. Our analysis based on the Lagrangian Averaged Vorticity Deviation (LAVD) method (see, e.g. Haller et al., 2016) has been previously applied in solar physics to identify 2D observational vortices Silva et al. (2018); Chian et al. (2019, 2020). As indicated by its name, LAVD is a Lagrangian methodology and it is based on following the particles in order to identify vorticity-dominated regions. For a plasma velocity $\mathbf{u}(\mathbf{x}(\mathbf{t}), \mathbf{t})$, we can define the vorticity as $\boldsymbol{\omega} = \nabla \times \mathbf{u}$ and, therefore, the LAVD field can be represented as

$$LAVD_{t_0}^{t_0+\tau}(\mathbf{x}_0) = \int_{t_0}^{t_0+\tau} |\boldsymbol{\omega}(\mathbf{x}(t), t) - \langle \boldsymbol{\omega}(t) \rangle| dt. \tag{3.1}$$

Here, τ is a given time interval and $\langle \boldsymbol{\omega}(t) \rangle$ is the spatial mean of the vorticity at time t. The position of flow patches, $\mathbf{x}$, is calculated by solving the advection equation,

$$\frac{d\mathbf{x}}{dt} = \mathbf{u}(\mathbf{x}, t), \tag{3.2}$$

over a grid of initial positions $\mathbf{x}_0$ placed in a horizontal xy-plane until the final positions $\mathbf{x}(t_0 + \tau)$ are reached after a finite-time duration τ. Note that

the LAVD field depends on the integration time. The average lifetime of flow vortices in simulation considered in the present paper is 80 s (Silva et al., 2021). To perform our analysis we set $\tau = 35$ s as after this time the vortex surface becomes deformed and, therefore, further analysis is difficult. This time is roughly half of the average lifetime of a vortex. We used the initial time $t = 1321.9$ s and integrated until $t = 1356.9$ s.

To construct a three-dimensional vortex tube, Haller et al. (2016) proposed a method based on the isosurface of the LAVD field. First, one identifies the outermost convex contour of LAVD surrounding a local maximum at a chosen height and then finds the isosurfaces, i.e, the set of points having equal values for the LAVD field at all the planes for which LAVD was computed. For our analysis, we have computed LAVD field for the 60 xy-planes above the simulated solar surface. The isosurface provides the 3D vortex boundary and describes the initial location for the material elements that undergo the same intrinsic dynamic rotation. The vortex boundary as defined by LAVD is a rotational Lagrangian coherent structure. Following Haller (2015), a lagrangian vortex can be described as a Lagrangian coherent structure since its boundary is a material surface separating regions with vortical and non-vortical dynamics. In other words, it remains together for the time of the analysis, being defined by the plasma flow and separates the region in the solar atmosphere where the vorticity dominates the plasma dynamics.

We allow some deviation from convexity for the vortex contour as, the vortices will most likely have cross-section deviating from convex shapes. This convexity deviation is called convex deficiency and is defined as

$$c = \frac{A_c - A_{ch}}{A_c}, \tag{3.3}$$

where A_c is the area which is enclosed by the extracted contour, and A_{ch} is

the area enclosed by its convex hull. Originally, the convexity requirement was established as a way to dismiss false detections caused by high vorticity concentration driven by shear flows. As shear regions do not present convex shapes in non-magnetized flows, the condition of a convex contour would identify only the true vortical motions. However, this requirement is not enough to dismiss wrong vortex identification in the solar atmospheric flows (see, e.g. Silva et al., 2018). Nevertheless, the convex contour also help to identify the stable vortices as the sturdy tubular vortical structures in the flow present near-circular cross-section. The convexity condition ensures that any material vortex starts out unfilamented at the initial time t_0.

The LAVD field computed at $z = 1.5$ Mm is shown in Figure 3.2 (top panel). The boundary of the identified vortices at that height are depicted by red curves. We select three particular vortices (located within black squares) to analyse further their kinematic and dynamic properties. They are labeled as R_1, R_2 and L_1, where labels R and L represent a clockwise and counter-clockwise directions of their rotation, correspondingly.

In general, the whole domain under consideration consists of more than a hundred identified vortices. In order to demonstrate the full potential of LAVD, we focused our analysis only on the vortex tubes that had the greatest vertical length. The selected R_1, R_2 and L_1 vortices spanned over a distance covering both the photosphere and bottom part of chromosphere, their lifetimes were long enough and they represented the general vortices behaviour features identified in numerical simulation. To connect rotational motion from different heights, one should optimize the detection for each vortex, that is the detection should identify the vortex surface such as it encompasses most of the vertical extension of the simulated atmosphere. This can be carried out by trying to define the LAVD contour and distinct values of convex deficiency at different height levels. The three-dimensional boundary of R_1, R_2, and L_1

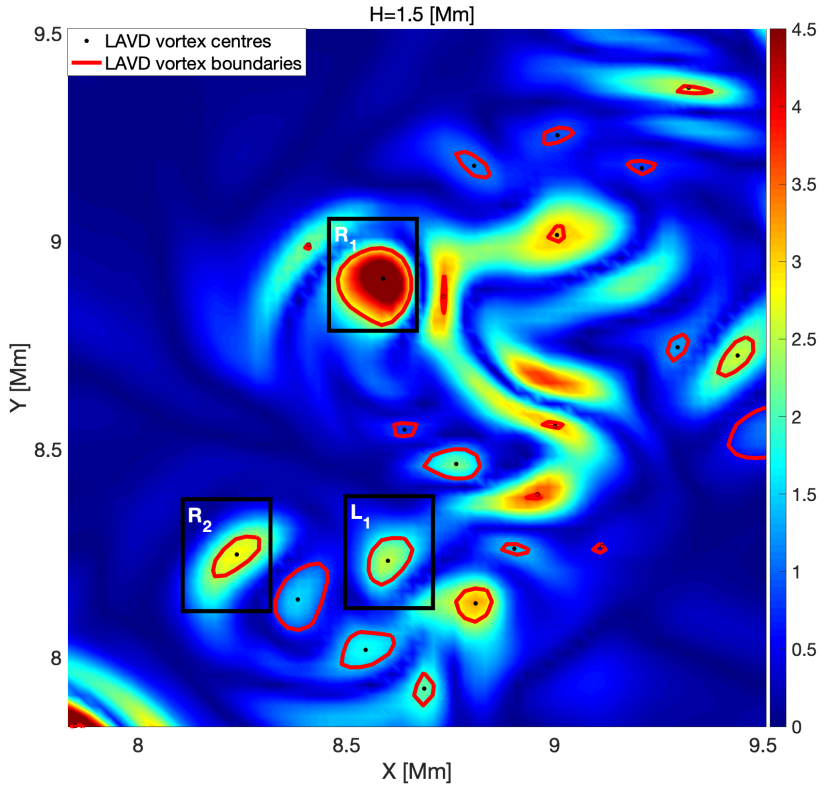

(a)

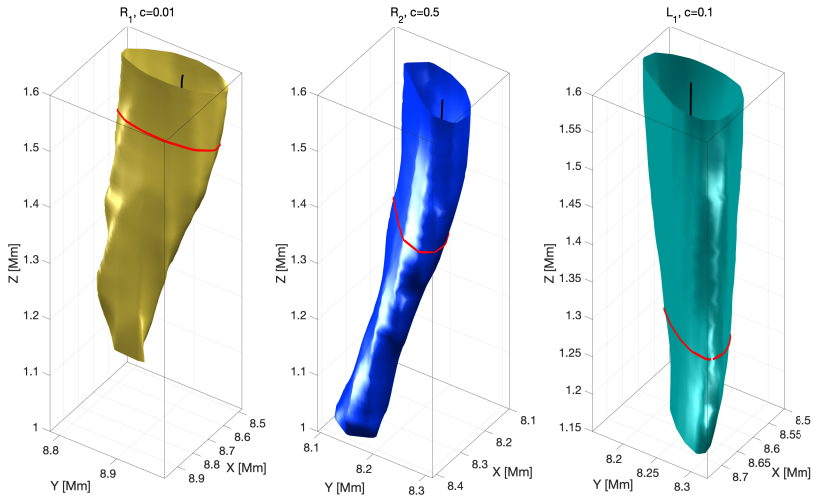

(b)

Figure 3.2: The top panel shows a two-dimensional horizontal slice of the computational domain at the height $z = 1.5$ Mm. The colours correspond to the local values of the LAVD field (see Equation 3.1). The red contours show the outermost convex boundary of the local maximum of the LAVD field. The selected vortices are located within black squares and labelled as R_1, R_2 and L_1. The bottom panels show their 3D reconstruction (shown in different colors). The cross-section, indicated as a red curve for each 3D surface, represents the selected height to plot the isosurface.

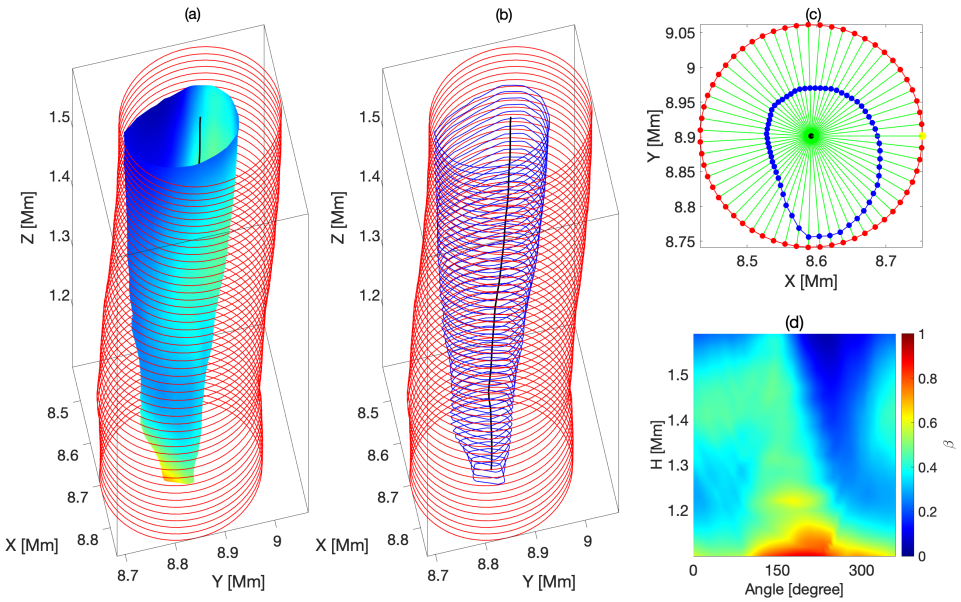

Figure 3.3: The projection technique used to create a 2D regular surface from 3D irregular shape. (a) The 3D surface displays the vortex tube colored by the plasma-β. The red circles at each height have centres which come from vortex identification and the position of these are given by the black line. The red circles have the same radius at each height. (b) The blue contours show the boundaries of the vortex. (c) The green segments represent the radii of the vortex and the circle at one particular height. The black dot indicates the centre of the vortex. The vertices of the vortex are indicated by blue dots. Red dots denote the perimeter of the circle. (d) The last panel describes the projection of the 3D vortex surface in a 2D surface coloured by the plasma-β. The corresponding video can be found on the PDG visualisations web-page.

vortices, were established from isosurfaces for the LAVD value at the outermost convex two-dimensional contour at heights of 1.57, 1.44 and 1.32 Mm, respectively. For each isosurface, a different value of convex deficiency was applied in order to maximize the area encompassed by the boundary. For the chosen vortices the associated values of convex deficiency are $c = 0.01$, 0.5, and 0.1, respectively. The center of each vortex was defined as the local maxima of the LAVD field (see e.g. Haller et al., 2016). It is shown as a black dot, see Figure 3.2(a), or as a black line, see Figure 3.2(b).

3.2.3 Vortex tube projection on a envelope grid

In this section, we introduce a new methodology to study the plasma dynamics at the surface of the vortex. Due to the complexity of spatial distribution of vortex parameters, e.g. velocity, pressure, temperature, etc. the analysis of three-dimensional vortices is difficult. One possible way is to create the stereoscopic projection of the vortex surface, i.e. mapping of the vortex surface onto a two-dimensional grid (envelope grid), as displayed in Figure 3.3. The three-dimensional view of the original surface of a selected vortex is depicted in Figure 3.3(a). Its surface is colored by the plasma-β value and co-centered with the envelope grid represented by the red circles equidistantly distributed in the vertical direction. The values of the variables at the vortex surface were determined by the "linear" and "nearest" interpolation methods implemented in the *griddedInterpolant* Matlab function. Both methods were used, but the "nearest" approach has an advantage, as this method is faster and requires the least computational memory (see Matlab library for details). Figure 3.3(b) shows both the boundary and envelop grids. The shape of the vortex boundary (blue dots) and its projection onto the envelope grid (red dots) at $z = 1.18$ Mm are shown on the panel (c) of the same Figure 3.3. The black dot indicates both, the vortex centre and the centre of the envelope grid (represented by the

red circle). The green lines connect the centre of the vortex, corresponding vertices and projected vertices in the envelope. This process is repeated for each height of the vortex to obtain the full projection of the 2D vortex surface on a 2D envelope. The result is shown in Figure 3.3(d), where we display (as an example) the distribution of the plasma-β. The vertical axis covers the full height of the vortex, while the horizontal axis covers the whole 360° around the perimeter of the lateral surface.

3.3 Results

The changes on the vortex tubes due to the flow dynamics were established by advecting the particles located at the vortex boundary and saving their position for each time frame. The time interval used for the advection is the same one applied for the LAVD computation, i.e. $t = 1321.9$ s to $t = 1356.9$ s. The temporal evolution of the vortex's shape for the analysed vortices is displayed in Figure 3.4. All the structures display the same general tapered tube shape with some deformations along their surface. Figure 3.4 indicates that, as the vortices rotate, they tend to be stretched in the vertical direction due to the existing downflows in the intergranular lanes. To estimate downdraft speed, first, the position of every particle in the vertical direction was calculated for every time snapshot and then propagated across all the advected particles. As a result, the estimated value is in the range 0.7-1.08 km s^{-1}. The downdraft speed has large values close to the bottom part of the vortex structures and it tends to zero close to the upper region as a consequence of the boundary conditions of the simulated domain (see Figure 3.5). It is clear that the vortex surface tends to present greater stretching in the lower part of its boundary.

The surfaces of all three vortices can be successfully recovered using the LAVD technique, even in the case of thin structures, such as vortex R_2. How-

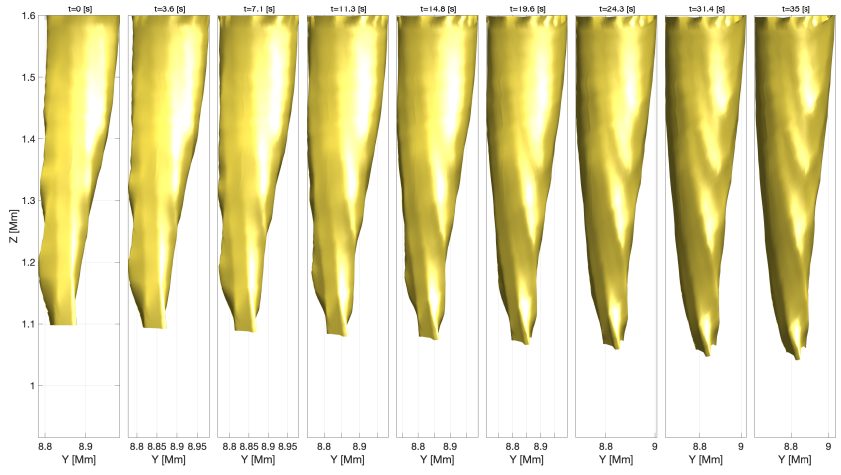

(a)

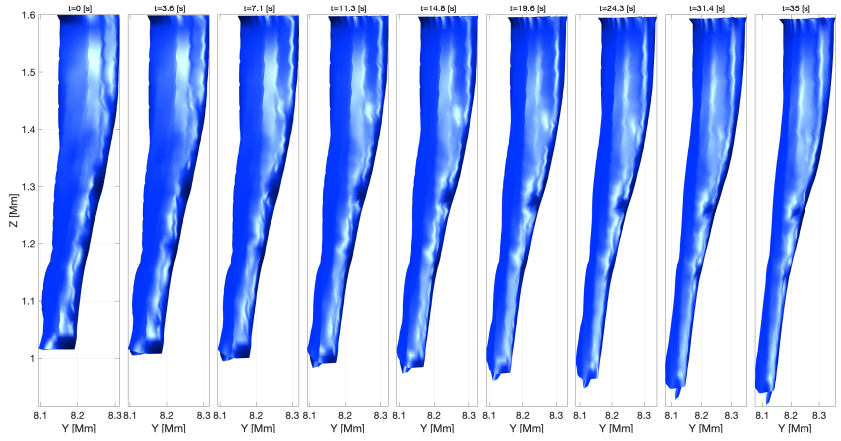

(b)

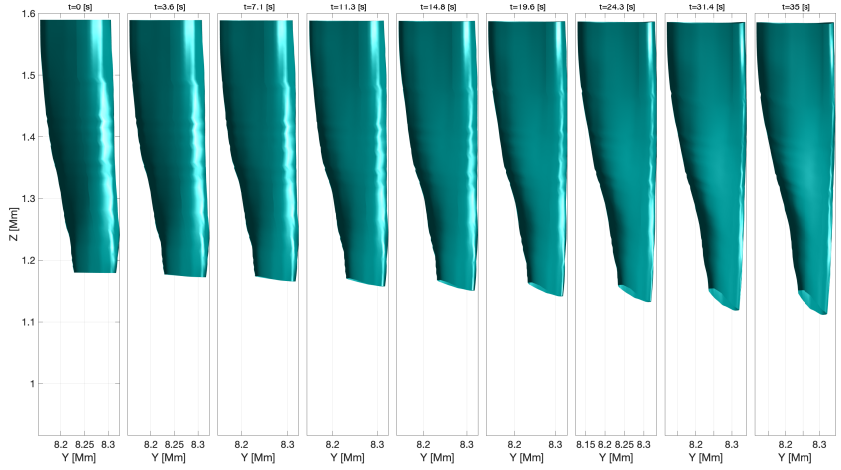

(c)

Figure 3.4: Advected vortex boundaries observed from the yz perspective. From top to bottom: material surface of the R_1, R_2 and L_1 vortices, respectively. The temporal evolution of the three vortices is shown (from left to right) as a time sequence. The different colours are used to identify the vortices.

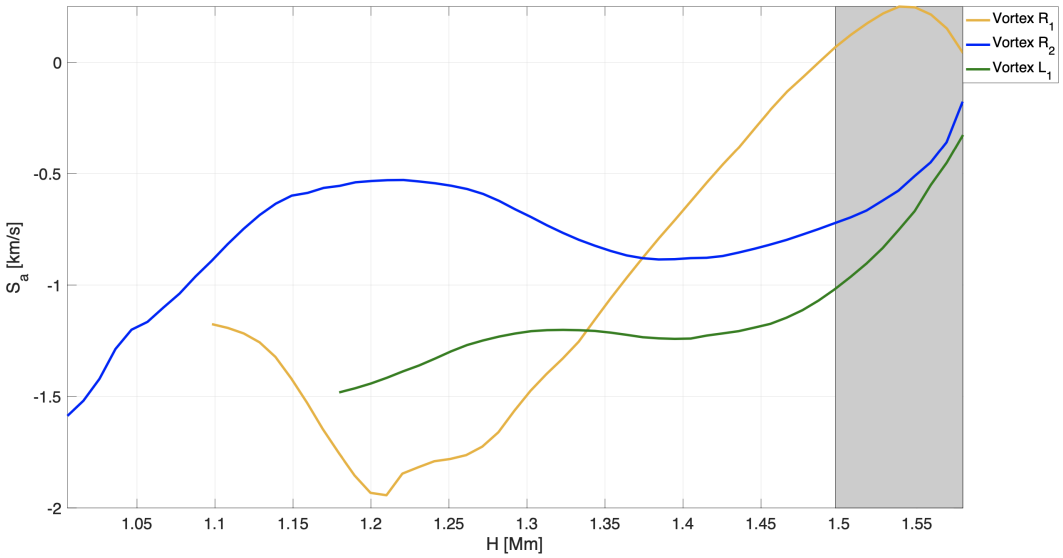

Figure 3.5: The average downdraft speed (S_a) as a function of height. The physical significance of the negative values in average speed demonstrates that the flows are in the direction of z. The range of heights that are near to the top boundary of the MURaM simulation is represented by the grey colour. The values corresponding to the three vortices are shown by distinct colours.

ever, further analysis in the case of vortex R_2 is very difficult due to the limited spatial resolution, therefore, in what follows we focus our analysis on the vortices R_1 and L_1 only. The plasma dynamics during the time interval of the analysis is described by the key plasma variables obtained from interpolation as the particles on the vortex boundary were advected. We carry out a Lagrangian analysis on the vortex evolution, i.e. we study the temporal evolution of the plasma variables at the material surface defined by the particle advection. Our study was performed for the time interval used to compute LAVD, from $t = 1321.9$ s to $t = 1356.9$ s. Figures 3.6, 3.7, 3.8 and 3.9 display the density, pressure, plasma-β, temperature, velocity and the components of the magnetic field at the R_1 and L_1 vortices surfaces. The panels (from the bottom to the top) show the variation of these physical variables on the vortices' surfaces at six different time-frames, with a regular cadence of 6 s. The vertical extent of each snapshot covers the whole height of the vortex, while the horizontal extent of each snapshot covers the whole 360° around the perimeter

of the lateral surface. In Figures 3.6 and 3.7, the results obtained for R_1 are shown in the first two columns, while the last two columns display the results obtained for the vortex L_1.

Figure 3.6 displays the Lagrangian evolution of density and pressure for the two vortices. Comparing the evolution with height and time of these two quantities, there is no considerable difference between the two vortices except for small localized variations. Over time, there is a slight change in the density and pressure gradient along the vertical direction. For regions close to the simulated surface, we see the trend to have local concentration of plasma density and pressure as a function of time, but these tend to decrease with height.

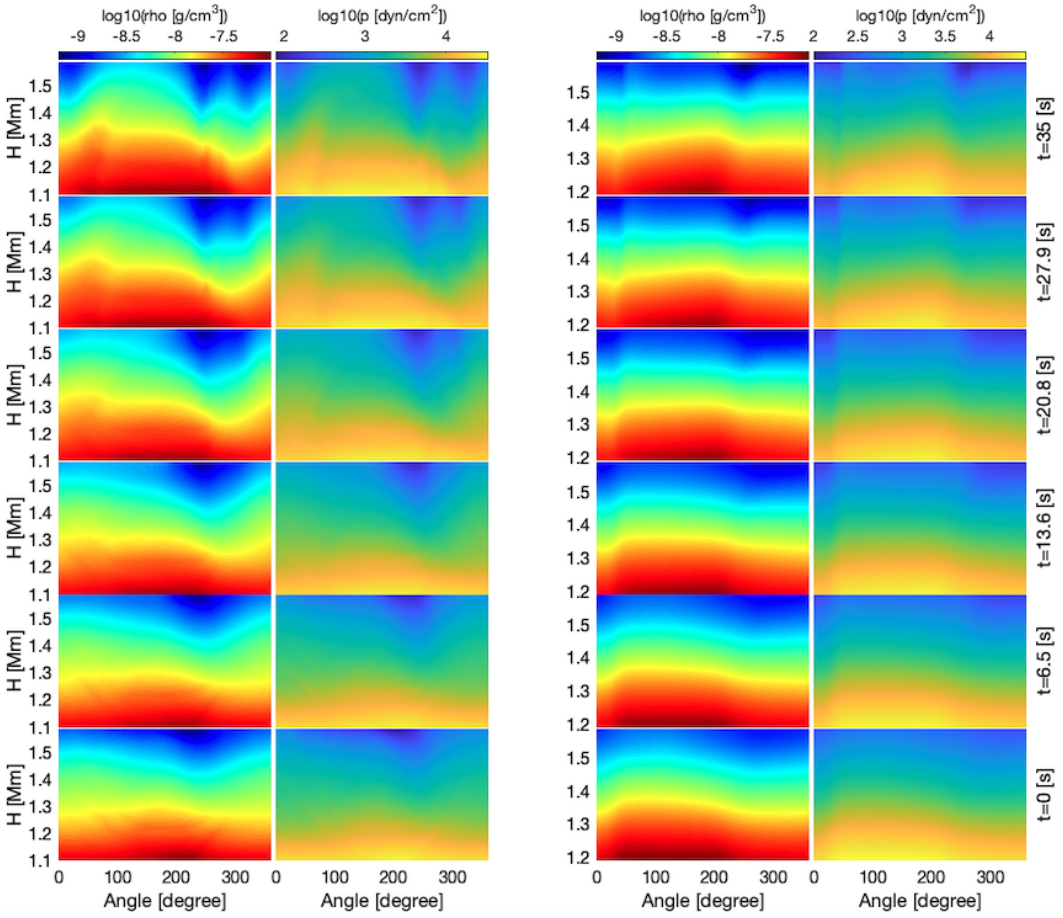

Figure 3.6: Density (rho) and pressure (p) changes with time for vortex $R1$ and $L1$, from bottom to top row. The first and second columns represent the $R1$ vortex, while the final two columns explain the $L1$ vortex.

From energetic and dynamical point of view it is essential to study the variation of the temperature and plasma-β parameter along the two vortices. The first and third column of Figure 3.7 shows the spatial and temporal evolution of temperature, measured in K. One very important result is that the temperature does not have a global behaviour, changes in this important quantity are rather localised. In general the top of the vortices are cooler than their bottom. It is also interesting to note that the surface temperature of vortex R_1 is decreasing in those regions where we have a depletion of plasma density.

The second and fourth columns of Figure 3.7 show the spatial and temporal changes in plasma-β. One important result visible in these snapshots is that the plasma-β is mostly less than one, meaning that the dynamics of the plasma is driven mainly by magnetic forces. It is also clear that during the evolution of the vortex, the value of plasma-β increases, in a similar way as the increase in temperature seen in Figure 3.7. In the case of vortex L_1 the dynamics in the bottom part of the vortex is driven mainly by pressure forces, however in time this diminishes and magnetic forces become more and more dominant.

The evolution of the three components of the velocity field indicates a stable flow configuration as displayed in Figure 3.8. This suggests that the detected vortices are stable rotating structures. The variations in the values of the horizontal velocity components suggest the presence of forces acting to accelerate or slow down the rotational plasma motion. As found in previous studies (Kitiashvili et al., 2013; Silva et al., 2020), the vortices experience both up and downflows during the time of the analysis, as indicated by the evolution of the z-component of the velocity.

Figure 3.9 shows the spatial and temporal evolution of the three components of the magnetic field. While x component of the magnetic field (B_x) shows a fairly homogeneous variation towards the bottom of both R_1 and L_1 vortices, it decreases towards the top. The B_y component shows a strong

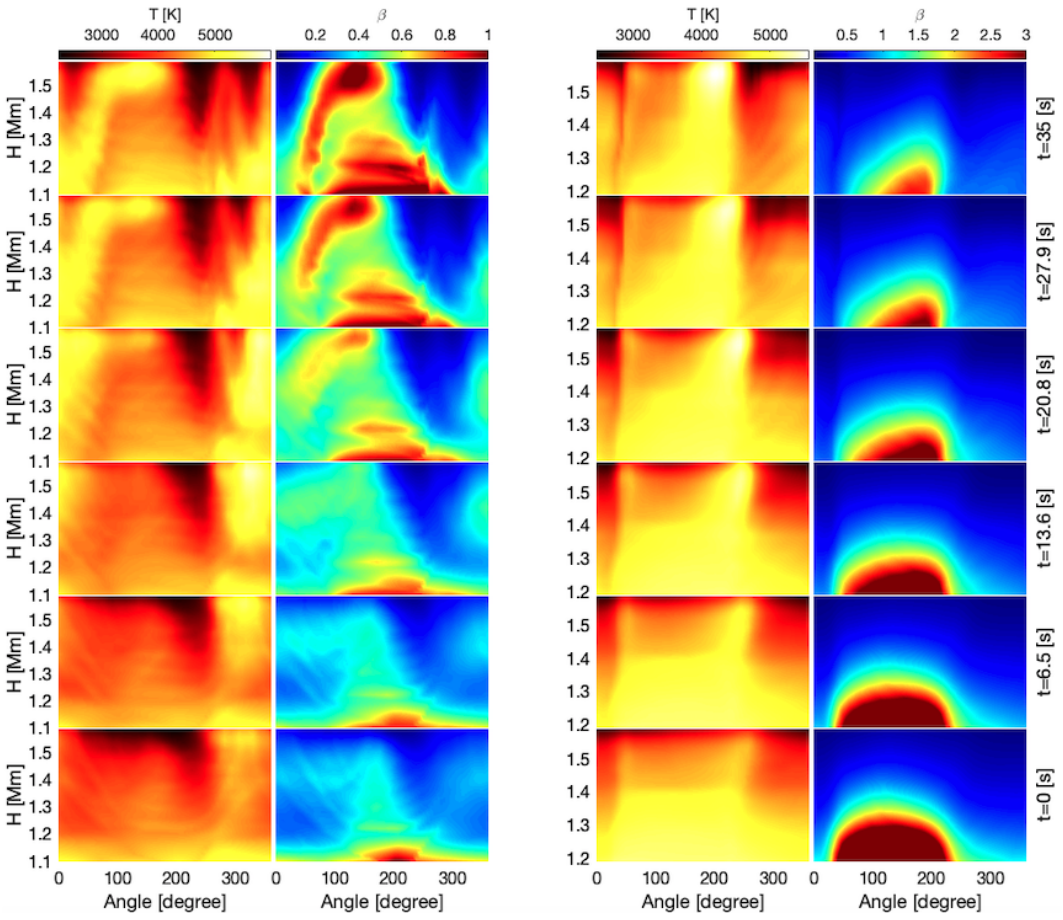

Figure 3.7: Temporal development (from bottom to top) of temperature (T) and plasma-β on the surfaces of the R_1 and L_1 vortices. The first and second columns correspond to the vortex R_1, whereas the third and fourth columns correspond to the vortex L_1.

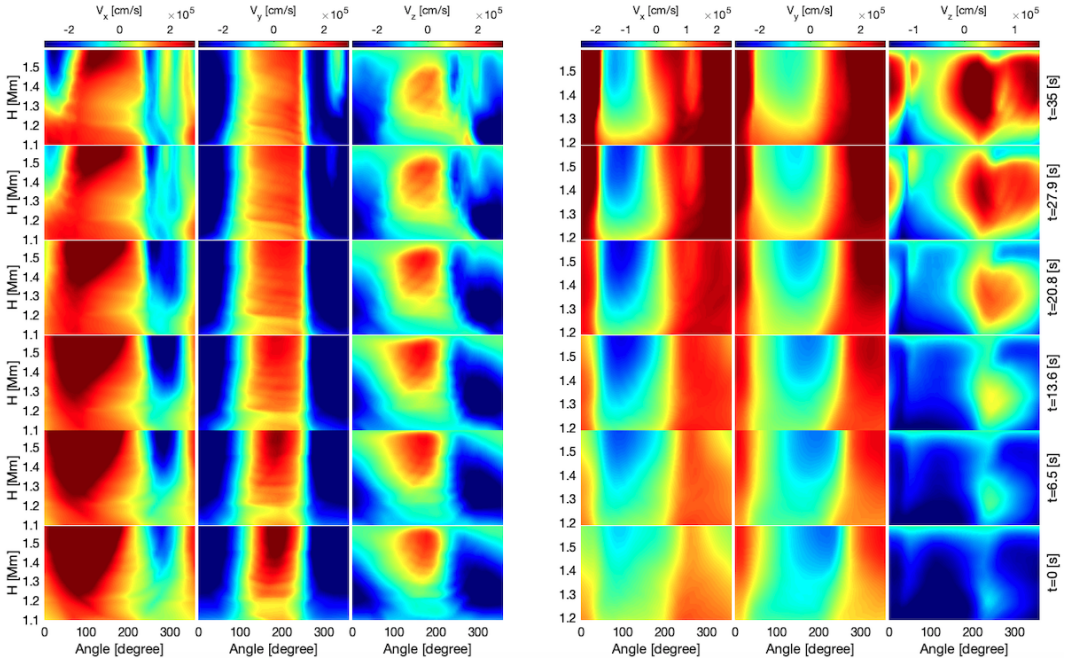

Figure 3.8: The temporal evolution of the three velocity components (V_x, V_y, and V_z) in the case of vortex R_1 and L_1. The first, second and third columns stand for the vortex R_1 and the last three columns describe the vortex L_1.

shear, however, the B_z component shows that the magnetic field decreases with height, creating strong vertical gradients. It is also clear that the vortices have predominantly vertical magnetic component, oriented upwards which increases in time, confirming the conclusion of the vortex's role as a local sink for magnetic fields. Except for the B_y component, there are no drastic changes in the orientation of the magnetic fields components at the vortices' boundary over time.

One of the most interesting aspects that help to determine the nature of the dynamics on the surface of vortices is the relative inclination of the magnetic and flow fields (see Figures 3.10 and 3.11). The magnetic field orientation is indicated by red arrows, while the direction of the flow field is given by blue arrows. The four snapshots are taken at regular time intervals, e.g. 0, 9.5, 18.4 and 35 s. In these figures the top row shows the evolution of the vortex's boundary and the directions of the two vectors fields, the bottom row shows the angle of the two vector fields measured on the surface of the

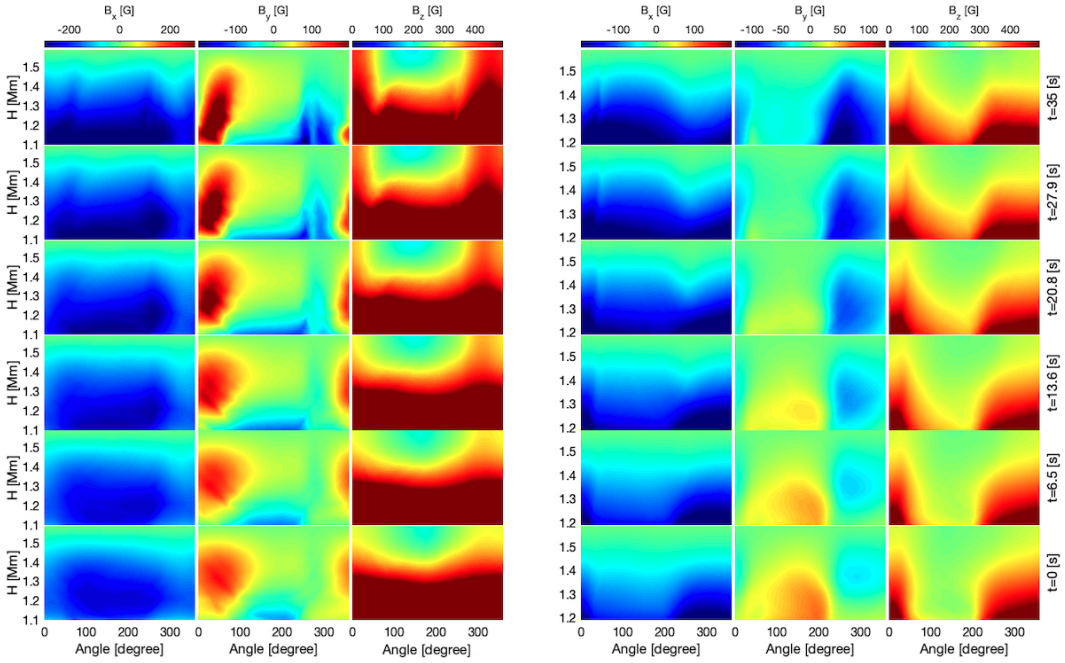

Figure 3.9: The temporal evolution of the three components of the magnetic field (B_x, B_y, and B_z) in the case of vortex R_1 (left panel) and L_1 (right panel). Since the z-component of the magnetic field is always positive, in the colour bar we use only positive values.

vortex, where the angle is shown on the colour bar, with 180° denoting an anti-parallel orientation. Initially, most of the lower part of the vortices presents magnetic and velocity fields directions practically anti-parallel. Looking at the arrows' orientation, it is clear that this tends to happen in parts of the surface with strong downflow. Over time, the relative orientation of the fields tends to change and the magnetic field is mainly aligned with the plasma flow (in regions with strong upflows). The narrow and tall regions in the two snapshots of Figure 3.10 correspond to a localised region where the two vector fields are anti-parallel and show an oscillatory pattern (with a characteristic length of about 100 km) that could be an indication of a wave propagation in an opposite direction to the magnetic field, advected downward by the flow (see also the fourth column of Figure 3.8).

The oscillatory pattern visible in Figure 3.10 is very localised. Due to the present resolution of the numerical domain, the full analysis of the nature of

these wave patterns can not be performed. We speculate that these waves might be slow magnetoacoustic waves, but further high-resolution simulations and methodology improvement are needed to clarify this point. In terms of methodology, it will require incorporation of the coordinate system with the direction along the magnetic field, and perpendicular to the vortex surface to be able to project the vector field parameters. This approach will be useful for the identification of velocity and magnetic field perturbations along and perpendicular directions to the background magnetic field and, therefore, wave identification. Furthermore, for an accurate determination we would also need information about the internal part of the vortex, an aspect that is not addressed here.

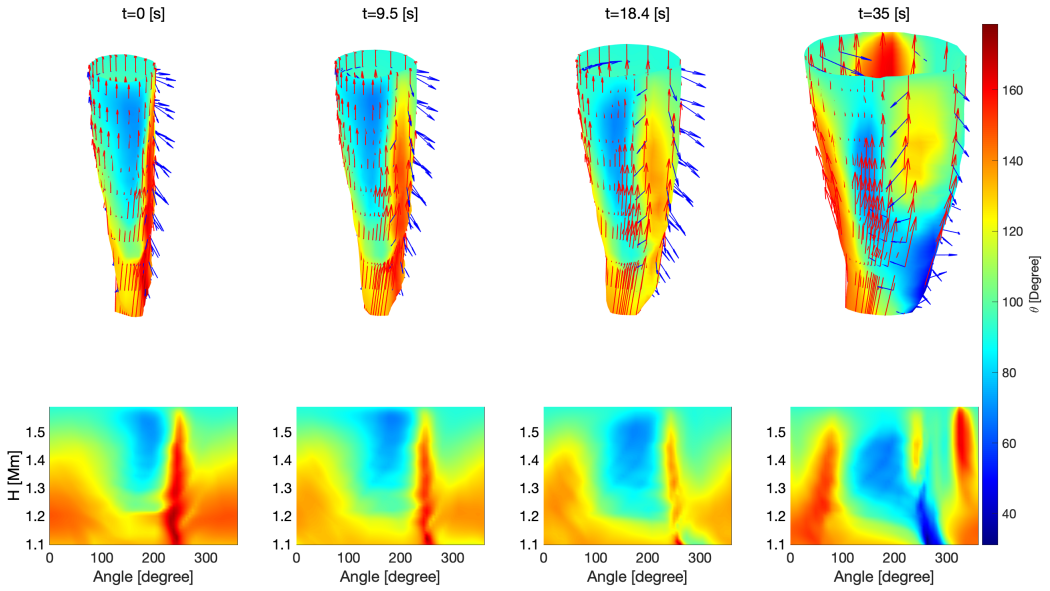

Figure 3.10: From the left to right the four snapshots of the R_1 vortex are shown (the magnetic and velocity fields indicated by the red and blue arrows, respectively). The vortex surface is coloured by the angle between the velocity field and magnetic field. The same angle is shown in the bottom row in 2D. The corresponding video can be found on the PDG visualisations web-page.

In the case of vortex L_1 at the initial time the two vector fields are anti-parallel, however, this decreases with time and the two vectors tend to be more aligned. To analyse the variation of the energy and momentum transport

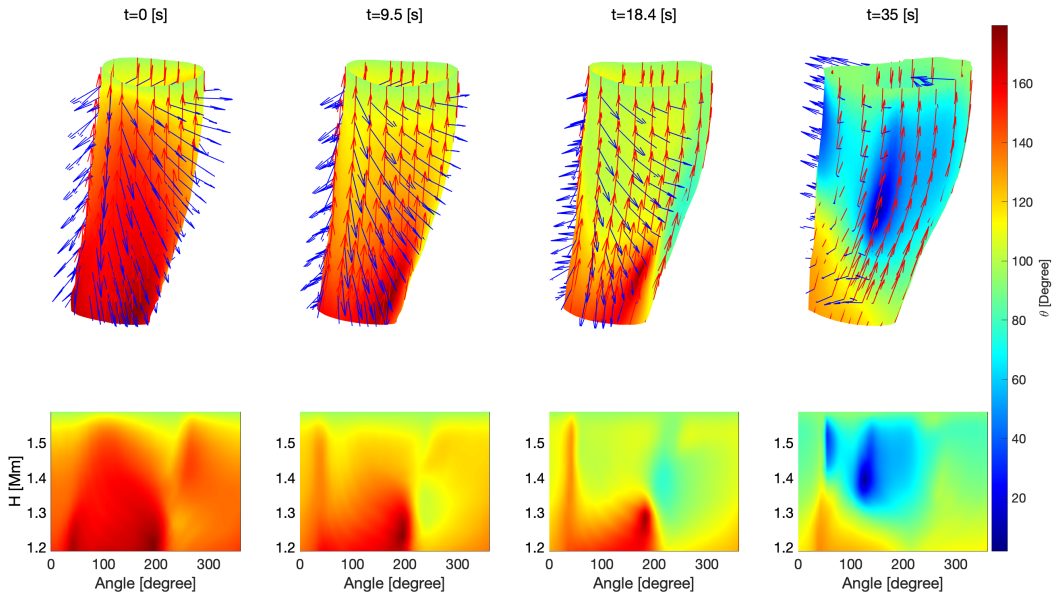

Figure 3.11: The same as Figure (3.10), but here vortex L_1 is presented. The corresponding video can be found on the PDG visualisations web-page.

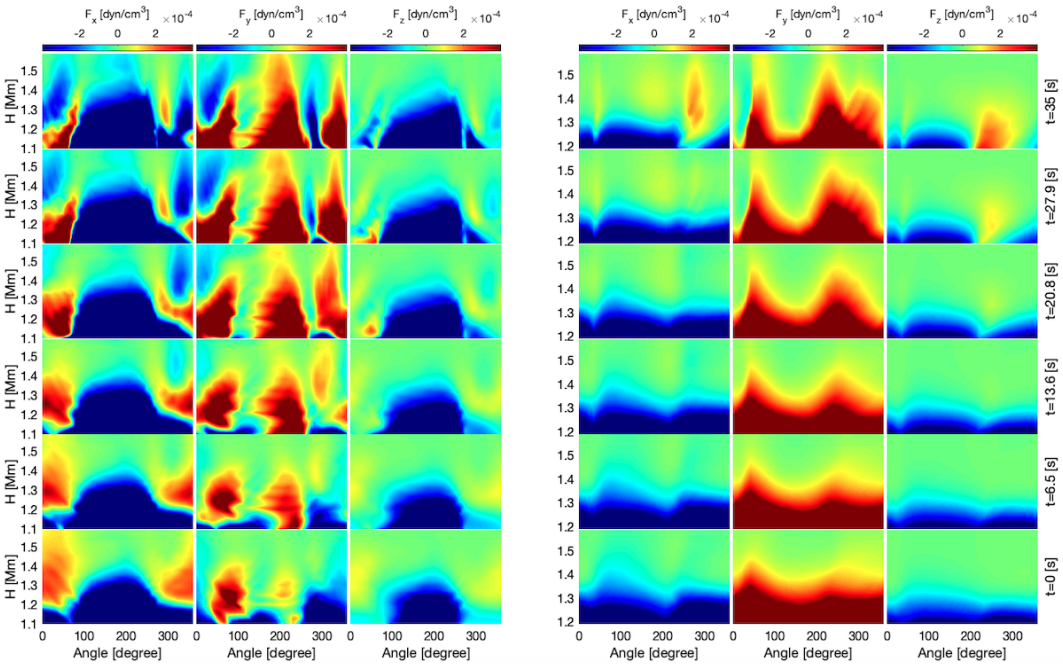

Figure 3.12: The temporal evolution of the three components of the Lorentz force (F_x, F_y, and F_z) in the case of vortex R_1 (left panel) and L_1 (right panel).

on the surface of the two vortices, the spatial and temporal evolution of the Lorentz force, pressure gradient and Poynting flux have been analysed. Figures 3.12 displays (from left to right) the components of the Lorentz force (F_x, F_y, F_z), for the vortices R_1 and L_1, respectively. This is the magnetic restoring force oriented in the perpendicular direction to the magnetic field that acts upon changes in the magnetic field (per unit volume on the fluid) and it is defined as

$$\mathbf{F} = \frac{1}{4\pi}(\nabla \times \mathbf{B}) \times \mathbf{B}. \tag{3.4}$$

The Lorentz force introduces a magnetic pressure and also a tension along the magnetic field lines. The left panel of Figure 3.12 describes the spatial and temporal evolution of the Lorentz force on the surface of the vortex R_1, while the right panel shows the same quantity, but in the case of vortex L_1. In general, the three components of Lorentz force in the two vortices demonstrate similar behaviour, with the value of the Lorentz force at the top of the analysed structures being three orders of magnitude (on average) smaller than at the bottom. The Lorentz force shows large regions where the values of its components is very small, meaning that in this region the vortex dynamics is mainly driven by hydrodynamic forces. As expected, the most dynamically changing component is the one that is in the direction of azimuthal rotation (F_y) and shows a significant increase during the lifetime of the vortex. The three components also show that for each vortex the components of the force change their direction from the lower part of the upper part of the structure. The same oscillatory pattern can also be observed in the y component of the Lorentz force in the case of vortex R_1. In order to determine the dominant force driving the dynamics of the plasma on the surface of the two vortices, we calculate the components of the ratio of the pressure gradient force and

Lorentz force as

$$C_x = -\frac{\partial p}{\partial x}/F_x, \;\; C_y = -\frac{\partial p}{\partial y}/F_y, \;\; C_z = -\frac{\partial p}{\partial z}/F_z \tag{3.5}$$

These ratios are shown in the Figure 3.13 for R_1 and L_1 vortices. The chosen colours denote physically distinct regions. Accordingly, the red colour denotes regions where the pressure forces dominate, but the two forces are oriented in the same direction, the blue colour denotes regions where the two forces are anti-parallel but the pressure force is higher than the Lorentz force. The green and yellow colours mark the regions where the Lorentz force is larger than the pressure force, but the two colours are denoting the cases when the two vectors are parallel and anti-parallel, respectively. Finally, the white and black colours denote the cases when the two forces are equal, but the their orientation is parallel and anti-parallel. The results represented in Figure 3.13 are following. First of all, on the boundary surface of the vortex the two forces are never in balance. In the case of vortex R_1 the dynamics of the plasma in the horizontal directions show a rather complex pattern, with localised regions where the role of the dominant force is changing. When compared to the results showed for the distribution of velocity (see Figure 3.8), it is clear that in the case of vortex R_1 the plasma motion is mainly driven by pressure forces and the two forces are pointing, in general, in different directions. In time, the role of pressure forces diminish. In the vertical direction, there is also the tendency of pressure gradient forces being larger than the Lorentz force. The dynamics on the surface of vortex L_1 shows similar complexity thanks to the interplay of the two forces. Comparing these results with the findings shown in Figure 3.8 (left panel), it is clear that initially the flows in the positive x direction are driven by pressure forces, while the flows in the negative direction are driven by magnetic forces. Looking at the second panel of Figure 3.13 we can

conclude that in the y direction the two forces are almost always anti-parallel and motion in the positive/negative directions are driven by magnetic/pressure forces. Finally, the motion in the vertical direction shows an interesting feature, when the alignment of the two forces is changing in time from being mainly anti-parallel, to parallel, but pressure forces dominate everywhere.

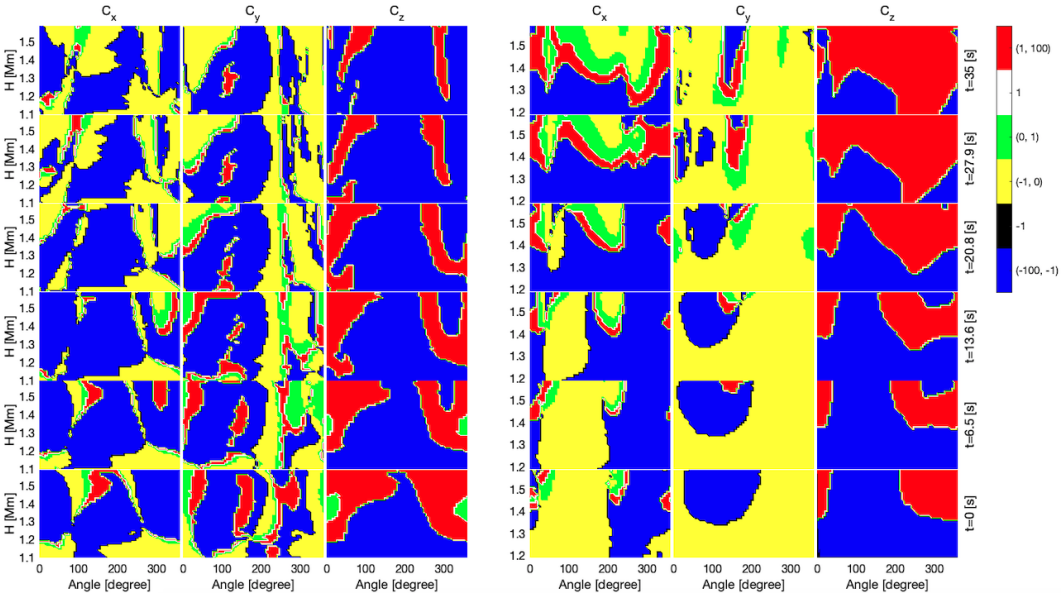

Figure 3.13: The temporal evolution of the three components of the ratio (C_x, C_y, and C_z) in the case of vortices R_1 (left panel) and L_1 (right panel).

MHD approximation of the Poynting flux is defined as the energy transferred by a wave across a unit area at any instant time and it is given by

$$\mathbf{S} = \frac{1}{4\pi}\mathbf{B} \times (\mathbf{v} \times \mathbf{B}) = \frac{1}{4\pi}\left[\mathbf{v}(\mathbf{B}\cdot\mathbf{B}) - \mathbf{B}(\mathbf{B}\cdot\mathbf{v})\right]. \tag{3.6}$$

The first term in the above equation is oriented in the direction of the velocity field, and it is proportional to the square of the magnetic field intensity. In contrast, the second term is in the same direction as the magnetic field, and it is proportional to the alignment of the magnetic and velocity fields. The evolution of the Poynting flux for the vortex R_1 is shown in the left panel of Figure 3.14 and the horizontal components show high correlation with the pattern of the plasma flow velocity shown in Figure 3.8. The fact that the

components of this vector have positive and negative values is attributed to the directions of the plasma flow, but in any case the direction of the energy flow agrees with the direction of the flow. It is interesting to note that the vertical component of the Poynting flux shows large regions where this quantity is close to zero, meaning that the electromagnetic energy is distributed mainly in the horizontal direction confirming the findings of Silva et al. (2022). In

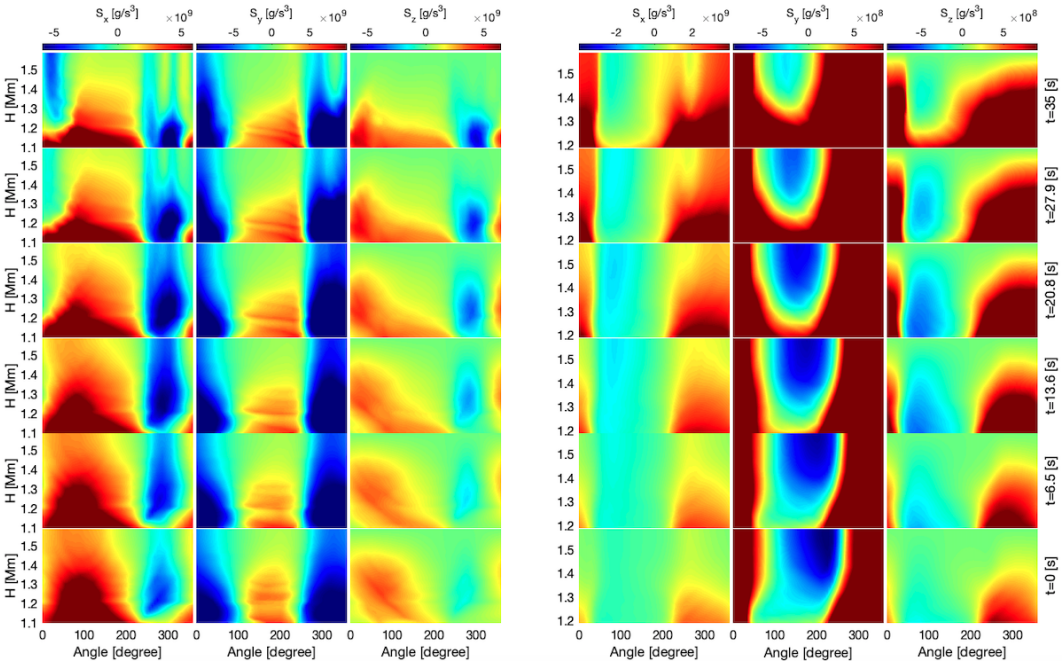

Figure 3.14: The temporal evolution of the three components of Poynting flux (S_x, S_y, and S_z) in the case of vortices R_1 (left panel) and L_1 (right panel).

the case of vortex L_1 the magnitude and the direction of the Poynting flux agrees with the direction of the plasma flow. Again, initially the Poynting flux is mainly horizontal, but in time, the vertical component increases thanks to the increase in the plasma flow seen in Figure 3.8. It is interesting to note the same periodic variation of the y component of the Poynting flux similar to the variation of the y component of the Lorentz force, and the characteristic length of these variation are similar.

3.4 Discussions and conclusions

The current study was dedicated to the analysis of physical paramaters on the surface of vortices in magnetoconvection numerical data which correspond to the dynamics in the lower part of the solar atmosphere. The comparison of radiative magnetoconvection simulations with the real observations has been reported in a number of papers, e.g. Schüssler et al. (2003); Shelyag et al. (2004); Khomenko (2005); Shelyag et al. (2007) to name but a few. Notably, Beeck et al. (2012) have compared results from a number of photospheric magneto-convection simulations produced by different codes and found that the results reliably represent the finest details of the observed solar radiation, including its temporal and spatial scales. Here, the three-dimensional vortex structure has been determined using Lagrangian analysis and the vortex boundaries were defined by means of isosurfaces of LAVD contours as previously suggested by Haller et al. (2016). Physically, the use of this technique means that all the particles on the surface boundary undergo the same intrinsic dynamic rotation. In other words, in the time interval used to compute the LAVD field, the fluid elements at the vortex boundary experience the same bulk rotation relative to the mean rigid body rotation of the fluid. The radius of the detected Lagrangian vortices increases with height, as also found for instantaneous vortex detection (Silva et al., 2020). For the selected vortices, we see the surfaces change in size while keeping their topology. In this paper, the LAVD approach was applied to a small subset of the numerical domain. Due to the fact that the procedure is automated, it may be used in large regions, too. This may be accomplished rather simply by selecting a constant convexity deficiency value and constantly searching for the LAVD isosurface that begins at the same height.

The variation of physical parameters on the surface of the examined vortices

show a very complex behaviour. The LAVD field was used to define vortex centres and their boundaries based on the fluid elements advection. The case of vortices presented in the current study, global changes are not occurring for all physical parameters. It is clear that the variation of density, pressure, particular magnetic field components are, to a very large extent, changing globally (see Figsures 3.6 and 3.9), however, the general characteristic of investigated vortices is that physical parameters describing the state of the plasma and quantities describing dynamics and energetics have a much more local character, meaning that changes occur locally (see, e.g. the variation of temperature, plasma-β, velocity and Lorentz force). The analysis of the Poynting flux components (see Figure 3.14) reveals that the energy flows are mostly present in the horizontal direction as previously discussed by Silva et al. (2022).

Due to the simultaneous presence of the oppositely oriented flows, the solar atmospheric vortices are mixing plasma predominantly in the vertical direction. The forces that drive the plasma dynamics on the vortices surfaces show a high degree of inhomogeneity (see Figure 3.13, for example). We anticipate that the increase of vertical velocity component (v_z) is related to the net force balance in the vertical direction. The pressure gradient is always pointing upwards and the gravity is always pointing downwards. Therefore, although the pressure gradient tends to dominate over the z-component of Lorentz force, from results presented in Figure 3.12 it follows that the changes in the vertical velocity are actually driven by the Lorentz force. Indeed, for both R_1 and L_1, we have deceleration and acceleration of vertical flow in regions where the Lorentz force is increasing downwards and upwards respectively. The pressure gradient dominance is expected since we are studying the vortex boundary, i.e. our analysis concerns the outermost region where the flow dynamics is more effectively affected by the vortical motions.

The structures we study also present dynamics whose driver undergoes a

transition, from being driven by kinetic forces, to a motion that is driven by magnetic forces. Therefore, the magnetic nature of the vortex, observed in previous studies (Shelyag et al., 2012; Kitiashvili et al., 2013; Silva et al., 2020), is not prevailing over the kinematic dynamics. Our results suggest the Lagrangian vortices recovered from the magneto-convection simulations do not rotate as a rigid body. This particular rotation will lead to the different angular velocities at different heights of the vortex. The analysis of the angular velocity profiles as a function of radius for the vortices identified in the magnetoconvection numerical simulations were presented in a recent investigation by Silva et al. (2020).

Future works will focus on the description of plasma and field parameters inside the magneto-convection Lagrangian vortices. Recent study by Battaglia et al. (2021b) has evidenced the propagation of Alfvén pulses inside a vortex structure. Our results suggest that we may have some signatures of wave propagation on the LAVD-identified vortex surface as periodic changes were observed for some variables (see Figures 3.12 and 3.14). Therefore, the methodology used in our paper to determine the values of physical parameters and their changes in time is suitable for the identification of the dominant physical parameters that drive the wave propagation.

CHAPTER 4

Waves on vortex surfaces

4.1 Introduction

Vortices and vortical flows in the solar photosphere are fundamentally important for the generation of magnetohydrodynamic (MHD) waves which are to propagate into the upper layers of the solar atmosphere. Vortex motions can transport the energy from photosphere into the higher upper of the solar atmosphere by means of MHD waves, where they can contribute to the heating of the solar upper regions (Fedun et al., 2004; Erdélyi and Fedun, 2007; Taroyan, 2008; Taroyan and Erdélyi, 2009; Antolin and Shibata, 2010). Vortex tubes are formed as coherent magnetic field structures in the solar atmosphere, e.g. twisted magnetic flux tubes.

Using nonlinear 3D simulations with a realistic vortex driver Fedun et al. (2011) found that the plasma structure of chromospheric magnetic flux tubes can act as a spatially dependent frequency filter for propagating torsional Alfvén waves. In addition, these authors showed that the swirly source that applied is capable of excitation of a variety of wave patterns.

From the discussion presented in Chapter 2 it is clear that magnetic structures in the solar atmosphere can support the propagation of a rich spectrum of waves. These waves can be considered as *global* waves, since the whole magnetic structure participates in the periodic motion, the magnetic structure moves as a whole. These waves are constantly observed in magnetic struc-

tures in different wavelength and they offer a unique tool for the diagnostics of plasma and magnetic field.

On the other hand, localised waves can be generated on the surface of these structures (similar to the surface waves at the interface separating water and air), however, these waves have much shorter spatial scale, making them very difficult to observe and study.

Our results discussed in Chapter 3.1 suggest that vortices may have the imprint of wave propagation on their surface, as short-lived periodic changes were observed for some variables (see, e.g. Figures 3.12 and 3.14). Although the vortices studied by us were numerically generated in a realistic solar atmosphere, the resolution of numerical data does not allow us to study these waves in great detail.

In this chapter, we will use the Proper Orthogonal Decomposition (POD) technique to identify and study the wave motion on the surfaces of the numerical vortices presented in Chapter 3. In addition, using synthetic data, we will carry out forward modelling of waves propagating along a magnetic flux tube with realistic vortex motion to recover the signature of possible waves using the same projection technique as presented in Chapter 3.

The Chapter is organized as follow: in Section 2 we introduce the Proper Orthogonal Decomposition (POD) method and apply this method to the *local* periodic changes observed on the surface of vortices studied in Chapter 3. Section 3 is devoted to the study of *global* synthetic oscillations of a vortex tube by constructing a suitable cylindrical flux tube on which we impose a rotational motion taken from the findings listed in Chapter 3. The morphology of these waves will be studied and the changes in the parameters of waves will be investigated in the present of vortical motion. Finally our results are discussed and conclusions are drawn in Section 4.

4.2 Local waves on the surface of vortices

One of the most successful methods developed for wave identification is the Proper Orthgonal Decomposition method.

Originally the method has its roots in the pioneering work by Pearson (1901), who aimed to develop a technique to be a mechanical equivalent of the principal axis theorem. The principles of these approach have been used by Lumley (1967), who developed the POD technique to identify and study coherent structures in turbulent flow-fields in fluid dynamics.

Nowadays POD is known by a number of names in the literature, such as principal component analysis (PCA) and Hotelling (or T-squared) analysis. The POD approach enables spatially orthogonal patterns to be determined from signals. Given the way the method is constructed, it recovers an equal number of modes as the number of samples in a given dataset, however, it can be easily shown that the majority of these modes are unphysical. Therefore, one of the most difficult aspects of this technique is the determination of which of the POD modes have a physical significance. On the other hand, the POD will also provide straightforward ranking criteria based on the contribution of the modes to the signal's variation. The POD was used in connection with granular flows and fluid mechanics (Murray and Ukeiley, 2007; Berry et al., 2017; Higham et al., 2017; Berry et al., 2017; Higham et al., 2020, 2021). Lately the method was used in solar physics by (Albidah et al., 2021) to identify MHD wave modes in the umbral regions of sunspots. In this study, we will apply POD method on the components of the velocity and magnetic field of MHD modes and vortices at their boundaries to identify local and global periodic changes. Before we proceed to this study we need to briefly overview the mathematics of this method for a better understanding of the results. Let us consider a set of time series (T) for a given physical parameter that can

be recovered from observation or numerical analysis (for instance the velocity field or magnetic field). Each of them has a spatial size $X \times Z$. As an example every snapshot has been reorganised to be as a column vector as shown in the matrix $D_{N\times T}$, with $N \gg T$. The matrix can be defined as

$$D_{N\times T} = \begin{pmatrix} d_{1,1} & d_{1,2} & \cdots & d_{1,T} \\ d_{2,1} & d_{2,2} & \cdots & d_{2,T} \\ \vdots & \vdots & \ddots & \vdots \\ d_{N,1} & d_{N,2} & \cdots & d_{N,T} \end{pmatrix}, \tag{4.1}$$

where $N = X \times Z$ and each column of this matrix represents the number of the snapshot, the data is now organized and ready for applying POD. One approach to find the POD decomposition of D is by using the optimum low rank approximation known as the Singular Value Decomposition (SVD) developed by (Eckart and Young, 1936). Accordingly, we write

$$D_{N\times T} = USV^* =$$

$$\begin{pmatrix} u_{1,1} & u_{1,2} & \cdots & u_{1,T} \\ u_{2,1} & u_{2,2} & \cdots & u_{2,T} \\ \vdots & \vdots & \ddots & \vdots \\ u_{N,1} & u_{N,2} & \cdots & u_{N,T} \end{pmatrix} \begin{pmatrix} s_{1,1} & 0 & \cdots & 0 \\ 0 & s_{2,2} & \cdots & 0 \\ \vdots & \vdots & \ddots & \vdots \\ 0 & 0 & \cdots & s_{T,T} \end{pmatrix} \begin{pmatrix} v_{1,1} & v_{1,2} & \cdots & v_{1,T} \\ v_{2,1} & v_{2,2} & \cdots & v_{2,T} \\ \vdots & \vdots & \ddots & \vdots \\ v_{T,1} & v_{T,2} & \cdots & v_{T,T} \end{pmatrix} \tag{4.2}$$

Here the matrix U of size $N \times T$ contains the spatial structure of the modes, each column represents one mode, and number of mode corresponds to the number of snapshot. The matrix S is a diagonal matrix which is ranked in descending order ($s_{1,1}, \geq s_{2,2} \geq \ \ldots \geq s_{T,T} \geq 0$), and explains the contribution to the total variance of the snapshot series. The matrix V of the size $T \times T$ represents the time coefficients of each mode and these represent the temporal evolution of the POD modes. Hence, the product of the $X \times Z$ two-dimensional

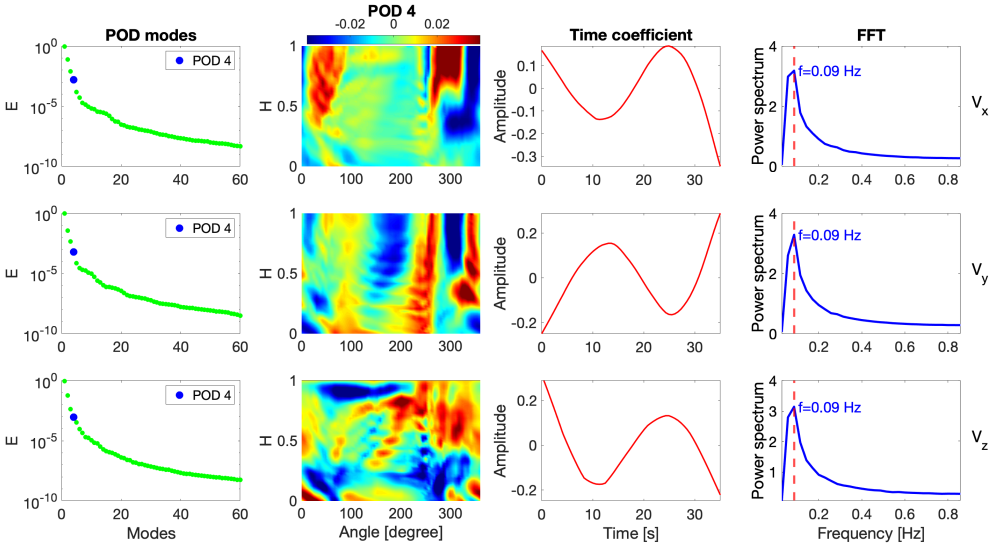

(a)

Figure 4.1: The first panel lists the power of the POD modes contributing to the signal for vortex R_1. The second column reveals the spatial structure of the POD 4 mode, the third column displays the time coefficient for the POD 4 mode. Finally, the fourth column provides the FFT for the POD 4 mode. The POD is applied on the components of the velocity.

spatially orthogonal eigenfunctions and their corresponding one-dimensional time coefficients are the spatial and temporal output of the POD analysis. These modes can be periodic or non-periodic and their amplitude can also vary with time as the POD has no restriction on the time coefficients.

The POD modes have a clear ranking in terms of their contribution to the total variance of the time series, and the ranking is given by the diagonal matrix S, with the diagonal elements λ of the matrix S. The contribution to the total variance of each POD modes is given by the vector

$$\lambda = \frac{diag(S)^2}{N-1}. \tag{4.3}$$

We consider the two vortices (R_1 and L_1) studied in detail in Chapter 3. The results of the POD decomposition for these structures are shown by Figures 4.1 and 4.2. The power distributions of the contribution to the signal of all the possible POD modes are given in the left-hand side panel. Although it

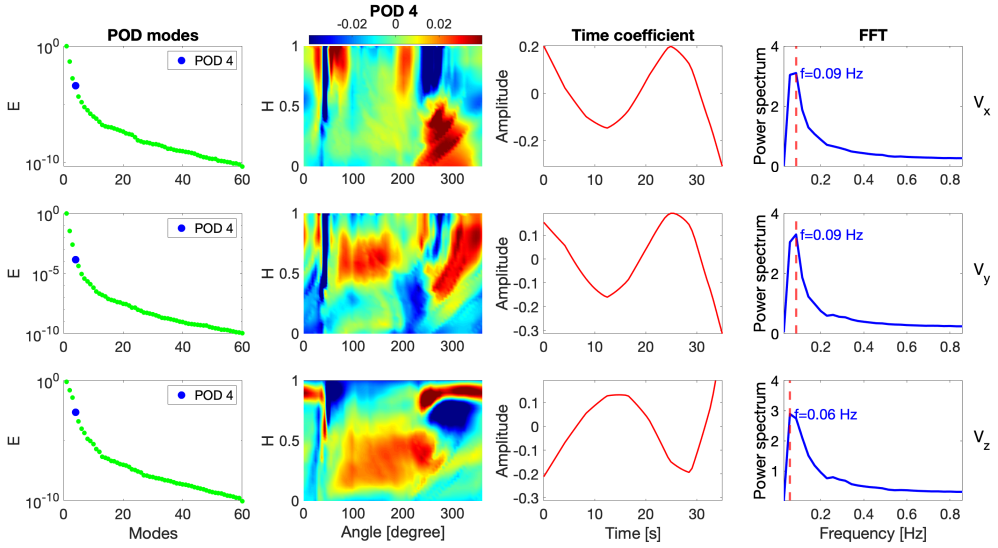

(a)

Figure 4.2: The same as in Figure 4.1, but here we present the results obtained for vortex L_1 .

does not have the highest contribution to the overall signal, we choose the POD 4 mode for both cases (vortex R_1 and L_1) because the time coefficient for each component has (at least) one period (see the third columns of Figures 4.1 and 4.2). The POD 4 mode intensity for each velocity component is shown in the second columns of Figures 4.1 and 4.2) and these indicate that the signature of wave propagation is present (periodically alternating and localised patterns) , confirming the results discussed in Chapter 3, where we found periodic changes for some variables on the surface of the vortex tube (see Figures 3.12 and 3.14). We should mention here that higher order POD modes, although presenting clear oscillatory pattern in their time coefficients, are not good candidates for our analysis because they have an even less contribution to the signal and their periodic change might be the result of the way POD decompose the original signal.

The Fast Fourier Transform (FFT) of the period changes detected on the surface of the two vortices reveals a wave propagating with a frequency of 0.09 Hz, with the frequency of the z-component of velocity for vortex L_1 having a slightly lower frequency. However, it still is not obvious what is the nature of

waves we observe. Since no earlier research has addressed how these kinds of waves can be observed, we attempt to explain how the patterns of MHD wave modes with vortex flow.

In order to better understand the nature and propagation characteristics of these waves we would need a much more detailed investigation of several vortices (including the variation of physical parameters inside their structure), a correlation analysis of periodic motions, and probably a more suitable analytical model that could describe the changes observed on the surface of vortices.

4.3 Global waves along a magnetic flux tube

In our quest to study the signature of global waves propagating along vortex tubes, first we are going to generate synthetic surface MHD waves propagating along the magnetic flux tube. The dispersion relation for these waves (Equation 2.47) has been discussed in detail earlier in Section 2.3.2.3.

The dispersion relation is solved for particular values $v_{Ai} = 2c_{Si}$, $c_{Se} = 1.5c_{Si}$, and $v_{Ae} = 0.5c_{Si}$ (typical for a photospheric magnetic structure) and the modes we will deal with are fast magnetoacoustic modes. The propagation characteristics of sausage, kink and fluting modes were shown earlier in Figures 2.6, 2.7 and 2.8, respectively. The choice of the phase speeds and wave numbers for each mode is shown in the Table 4.1.

With the help of Equations (2.49)–(2.56) we can find the value of the three components of velocity at the surface of the waveguide. Figure 4.3 depicts the pattern of the velocity field for the three MHD wave modes, as well as their combinations (right-hand panel). The surface of the flux tube is coloured to show the distance of particular points from the static symmetry axis of the tube, therefore, yellow and blue colours denote maximum and minimum distance. Next, we are going to surround the flux tube with a similar mesh grid as

Table 4.1: Summary of parameters used in connection with the cylindrical model to generate the global MHD modes propagating along the magnetic flux tube shown in Figure 4.3. Here the phase speed, V_{ph}, is given in units of kc_i and kr_a is the dimensionless wavenumber. The values of frequencies, dimensionless wavenumber and phase speeds were collected from the dispersion curves shown in Figure 2.5 and amplitudes are arbitrary values.

MHD mode	V_{ph}	kr_a	Frequency, Hz	Amplitude
Sausage, $n = 0$	1.45	1.88	0.1	2.5
Kink, $n = 1$	1.32	2.06	0.2	1.2
Fluting, $n = 2$	1.28	1.54	0.3	1.8

presented in Chapter 3 and we project the velocity components of the flux tube onto this grid. The transformation of the velocity vector between the cylindrical and Cartesian coordinate system is carried out using the transformation matrix

$$\begin{pmatrix} v_x \\ v_y \\ v_z \end{pmatrix} = \begin{pmatrix} \cos\phi & -\sin\phi & 0 \\ \sin\phi & \cos\phi & 0 \\ 0 & 0 & 1 \end{pmatrix} \begin{pmatrix} v_r \\ v_\phi \\ v_z \end{pmatrix} \tag{4.4}$$

Figure 4.4 shows the results of this projection, where the first three columns are representing the three velocity components for sausage, kink and fluting modes, while the last column describes the signature of the wave that is obtained as a result of the combination of these three waves. The combined waves contribute in equal weight to the resulting mode. The patterns of the three waves used here show typical behaviour, while the pattern obtained for the resulting modes is rather complex.

4.3.1 Vortex tube

In Chapter 3 we used magnetoconvection simulations from which we isolated and reconstructed two vortices (denoted by R_1 and L_1). These vortices were studied in great detail and the values of the velocities and magnetic fields on the lateral surface of these structures were shown by Figures 3.8 and 3.9. The

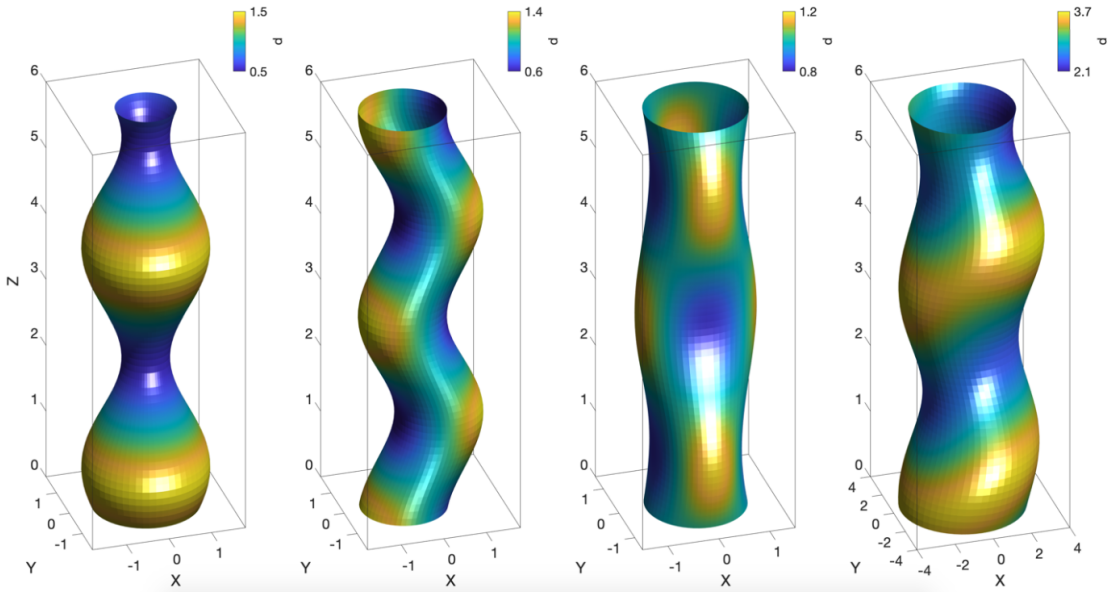

Figure 4.3: The sausage ($n = 0$), kink ($n = 1$), and fluting ($n = 2$) modes propagating along a magnetic flux tube are shown in the first three panels. The magnetic flux tube is represented within a cuboid of height 6 Mm and a horizontal sides of 4 Mm. The fourth panel shows the signature of the combined wave (the superposition of the mentioned three modes). The colour of the lateral surface of the flux tube is chosen to be proportional to the distance between the longitudinal axis of the tube and the lateral surface of the flux tube, so that yellow and blue colours represent the largest and the shortest distances, respectively.

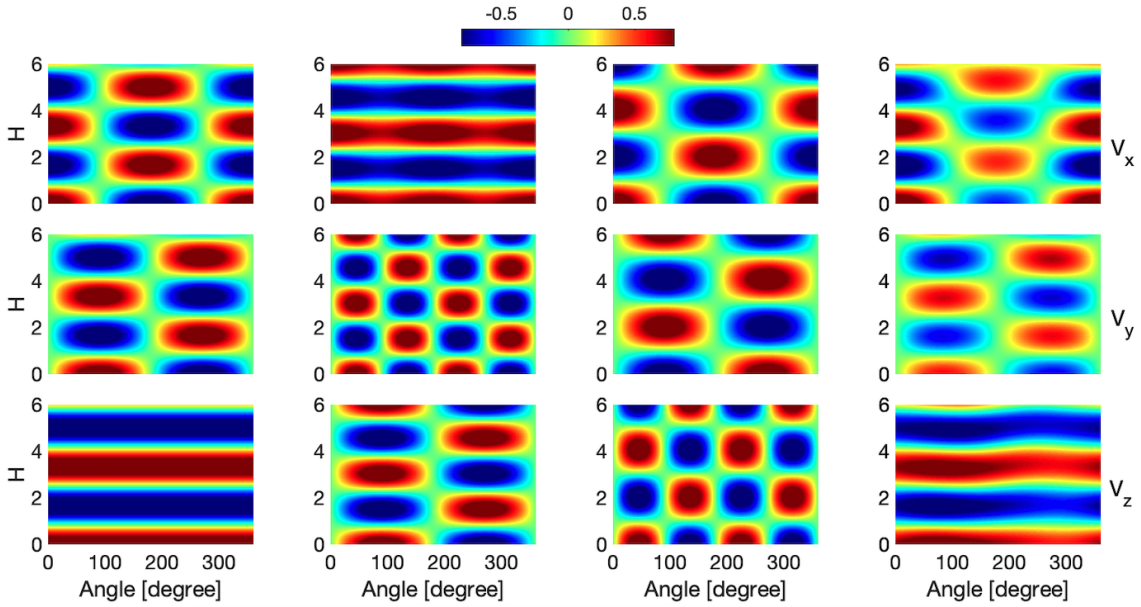

Figure 4.4: The velocity components of sausage, kink, and fluting ($n = 2$) modes projected onto a 2D mesh grid. Here the height corresponds to the height of the flux tube and the horizontal coordinate covers the whole 360° around the magnetic flux tube. The last column shows the signature of wave obtained as a combination of the three modes.

numerical dataset has been collected over an interval of 35 seconds with time cadence of 0.6 seconds, i.e. the data has 60 snapshots. Firstly, we need update the new Cartesian coordinate positions of the vortex centres and boundaries before we can begin to analyse them. The rationale for updating the new Cartesian coordinate location of vortex is to make the analysis of the MHD modes propagating along vortex tube more straightforward when they are combined.

Let us use the vortex R_1 as an illustration. Since the positions of the vortex centre and vortex boundaries are already known, we denote the coordinates of the vortex centre by x_i, y_i, and z_i in each snapshot. Similarly, we are going to denote by u_i, v_i, and w_i the Cartesian coordinate positions of the vortex boundaries for each snapshot, where $i = 1, 2, ..., N$ is the number of snapshots.

The new coordinates of the vortex centres and boundaries are updated by

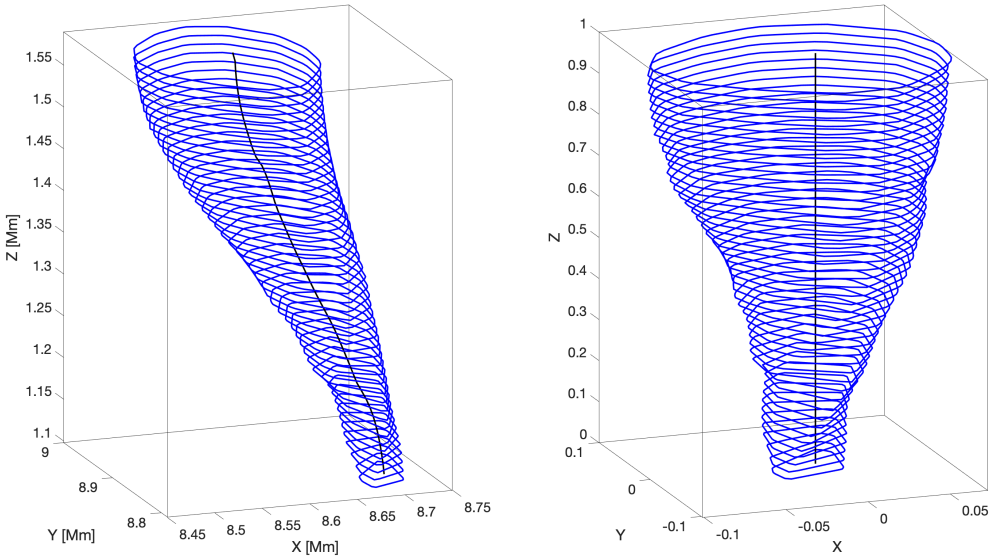

Figure 4.5: The left panel depicts the three-dimensional structure of vortex R_1; the blue line denotes the position of the vortex boundary at each snapshot, while the black line denotes the vortex centre. The right panel illustrates the same vortex, but the boundary and centre positions for each height have been subtracted from the centre positions for each height. The values along the z axis are normalised by the largest value in the z direction in the left panel.

using the definitions

$$X_i = x_i - x_{i-1}, \quad Y_i = y_i - y_{i-1}, \quad Z_i = \frac{z_i - min(z_i)}{max(z_i) - min(z_i)},$$

$$U_i = u_i - x_{i-1}, \quad V_i = v_i - y_{i-1}, \quad W_i = \frac{w_i - min(w_i)}{max(w_i) - min(w_i)}, \tag{4.5}$$

where X_i, Y_i, and Z_i denote the new Cartesian coordinate position of vortex centre, and U_i, V_i, and W_i are the new Cartesian coordinate position of vortex boundary (see Figure 4.5). The scaling presented in Equation (4.5) are introduced to make the symmetry axis of the vortex straight and centered on the origin of the coordinate system. The new quantities Z_i and W_i are necessary in order to normalise the height to be between 0 and 1. The scaling applied here are needed to make the structure and extent of the vortex tube similar to the flux tube along which waves propagate. The vortex tube constructed this way will provide the information about the rotation that will be added to the

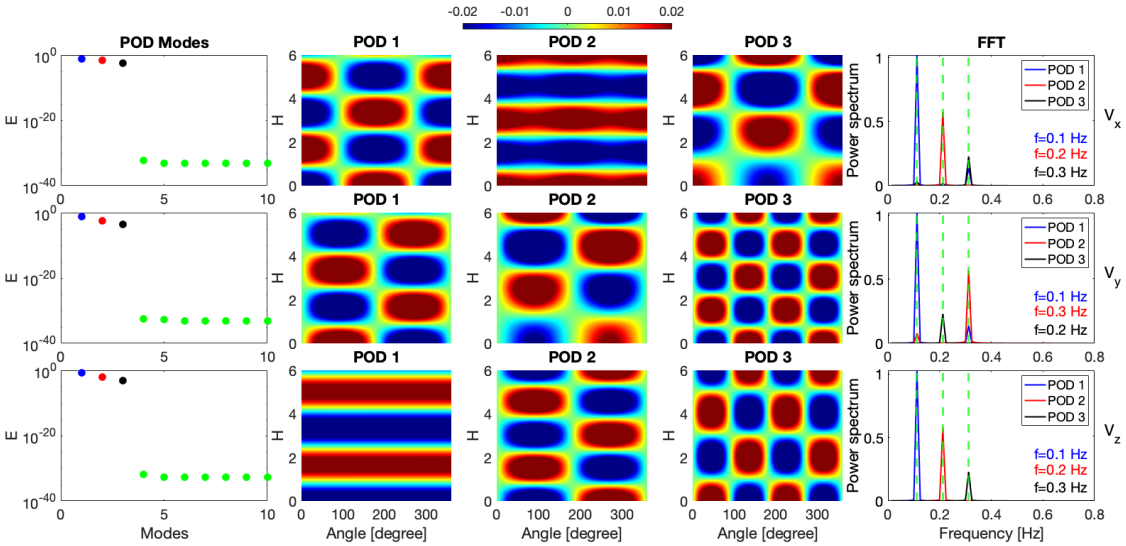

Figure 4.6: The first column shows the power of the POD modes contributing to the overall signal (here we plot only the first ten POD modes), the second, third and fourth columns show the intensity map of the first three POD modes for the three velocity components. The last column displays the Fast Fourier Transform (FFT) of the time coefficients of POD 1, POD 2 and POD3 modes. The values of the power spectrum are normalized to their maximum value.

oscillating magnetic flux tube.

4.3.2 Result

Figure 4.3 illustrates the oscillation pattern of the magnetic flux tube in the case of sausage, kink and fluting ($n = 2$) modes, as well as the mode that is constructed as a combination of the three modes. We next apply the POD technique to the time series for the combined MHD waves to them, as shown in the figure 4.6, which successfully recovers the three MHD waves. The left-hand side panel shows the power of the POD modes contributing to the signal. For simplicity we plot the power of the first ten modes, all the other POD modes have an even smaller contribution. It is clear that the three waves we combined (shown by the blue, red and black dots) have the most significant power, all the other modes recovered by POD have an insignificant contribution. The patterns shown by the POD analysis are identical with the patterns of the

three waves shown in Figure 4.4. The FFT analysis shown in the last column recovers the frequencies of the MHD waves, demonstrating the effectiveness of the POD method for mode identification.

4.3.3 Global MHD modes with vortex dynamics

With the synthetic data describing global oscillations of a flux tube and the velocity profiles recovered from the vortex tubes studied in Chapter 3, we can study the morphology of global MHD waves propagating along a vortex tube.

When the rotational motion of the vortex R_1 is superimposed on the velocity components of an oscillating flux tube, the pattern of waves will be modified and the results of the POD decomposition are shown in Figures 4.7, 4.8 and 4.9. The first column in these figures show the pattern of the three waves in a magnetic flux tube, the second column shows the velocity pattern recovered for the vortex R_1, while the last column displays the morphology of the three waves modified by the vortex motion. It is clear that the vortex motion has a dramatic influence on the pattern of waves, however, the periodic behaviour is observable. The most noticeable change is in the z-component of the velocity.

The aforementioned POD analysis is applied to the combined data and the morphology of the first five POD modes are shown in Figures 4.10, 4.11 and 4.12. The time coefficients of the POD decomposition for the three modes is shown in Figures 4.13, 4.14 and 4.15.

The time coefficients of the POD 1 mode show a clear oscillatory behavior in time, therefore the POD 1 modes in Figures 4.10, 4.11 and 4.12 they can be confidently classified as waves. As a matter of fact, the modes recovered as POD 1 modes are identical with the global mode we used for modelling and their FFT (see Figure 4.16) shows that although the morphology of these waves are slightly altered by the presence of the vortex motion, their frequency undergoes a Doppler shift.

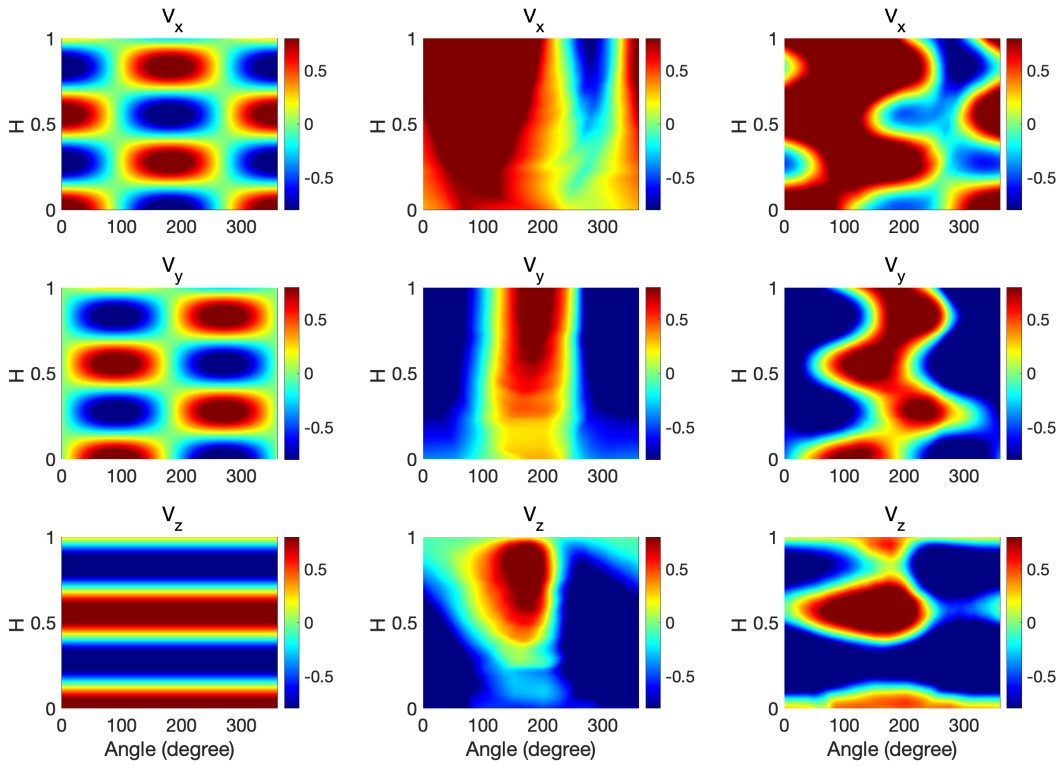

Figure 4.7: The signature of global sausage modes propagating along a magnetic flux tube in the presence of vortical motion. The first column depicts the components of the velocity field in the case of the sausage mode, the second column shows the components of the velocity field extracted from numerical simulations (here we use the vortex R_1). The final column displays the components of the combined velocity field. Each component is normalized by its maximum value of absolute value.

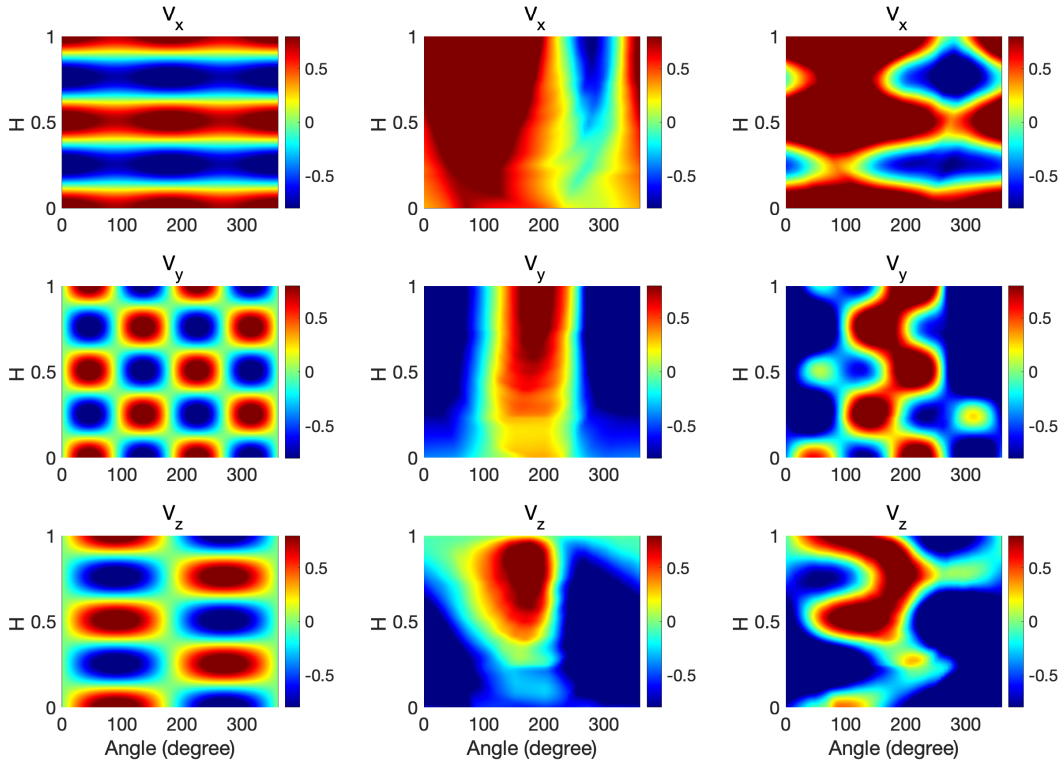

Figure 4.8: The same as Figure 4.7, but here we plot the values of the three components of velocity in the case of kink modes.

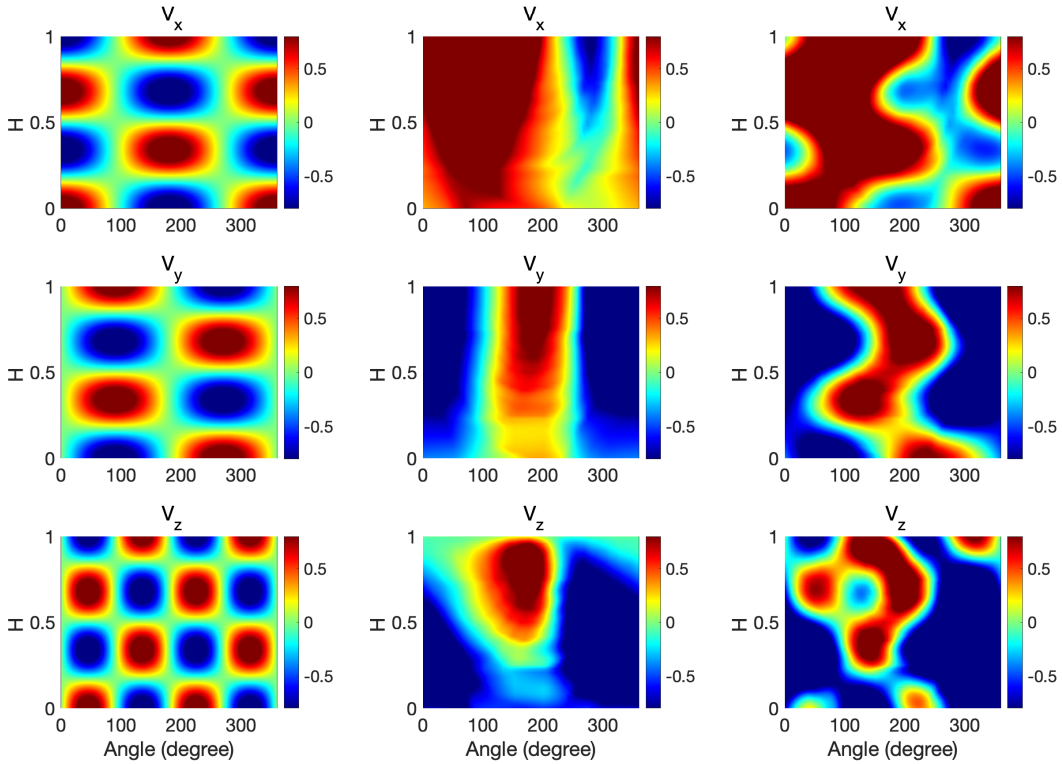

Figure 4.9: The same as Figure 4.7, but here here we plot the values of the three components of velocity in the case of fluting ($n = 2$) modes.

The time coefficients of the POD 2 modes do not show periodic change, therefore, these modes are not really waves. Indeed, comparing the second columns of these figures with the second columns of Figures 4.7, 4.8 and 4.9, it is clear that these are very similar, therefore we can conclude that this POD is due to the vortex flow.

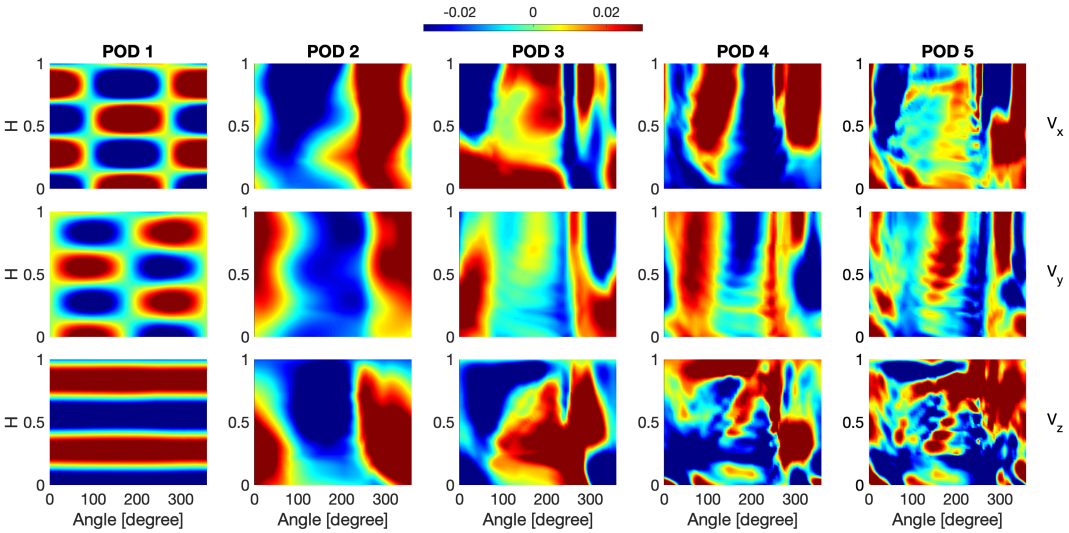

Figure 4.10: The first five POD modes in the case of fast sausage waves propagating along the vortex flux tube. The vortex motion correspond to the vortex R_1 identified and studied in Chapter 3. The rows correspond to the three velocity components.

The subsequent POD modes show that the signal is very much degenerated and the patterns shown on the last three columns of Figures 4.10, 4.11 and 4.12 resemble the applied vortex motion that is perturbed by the presence of waves. As a result, only local periodic changes can be observed, however the time coefficients of these modes do not show any periodicity.

A similar analysis with the rotational characteristics of the vortex L_1 would reveal similar results. The above analysis was performed for propagating fast waves. It is likely that the vortex tube in the presence of global slow waves would result in identical conclusions as in the case of fast waves.

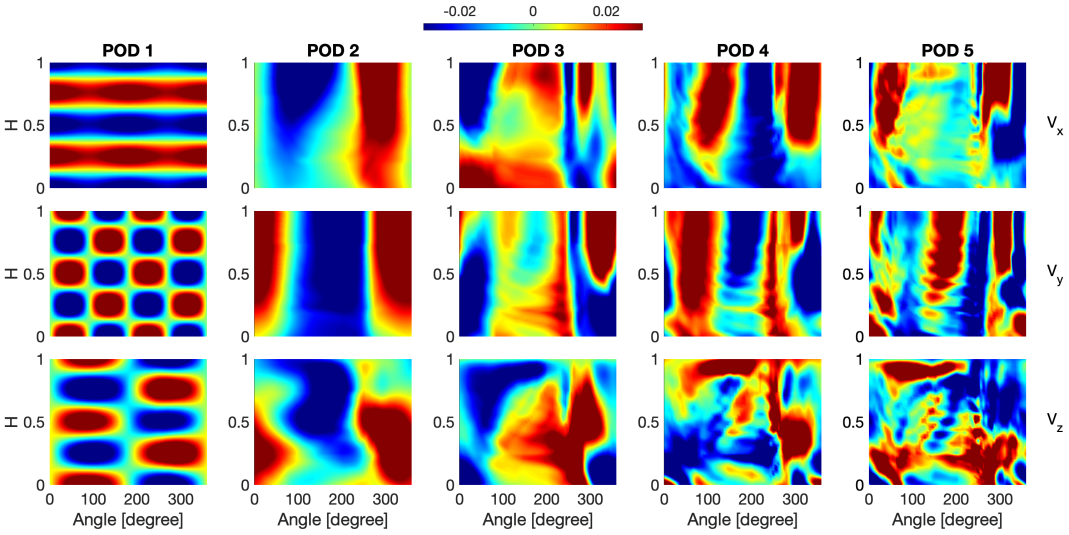

Figure 4.11: The same as Figure 4.10, but here we plot the POD decomposition of the vortex tube (based on the values of the three components of velocity) in the case of kink modes.

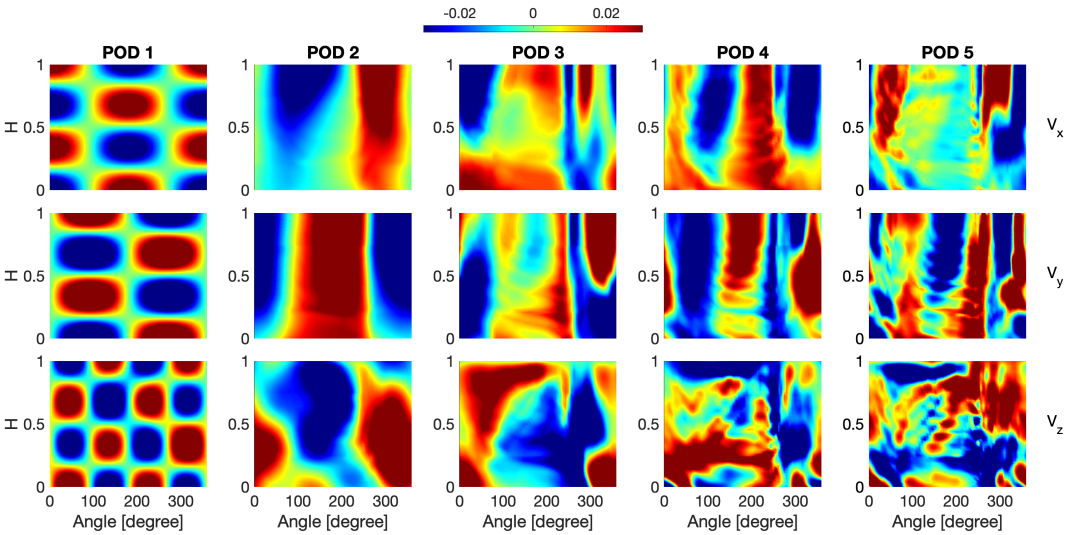

Figure 4.12: The same as Figure 4.10, but here we plot the POD decomposition of the vortex tube (based on the values of the three components of velocity) in the case of fluting ($n = 2$) modes.

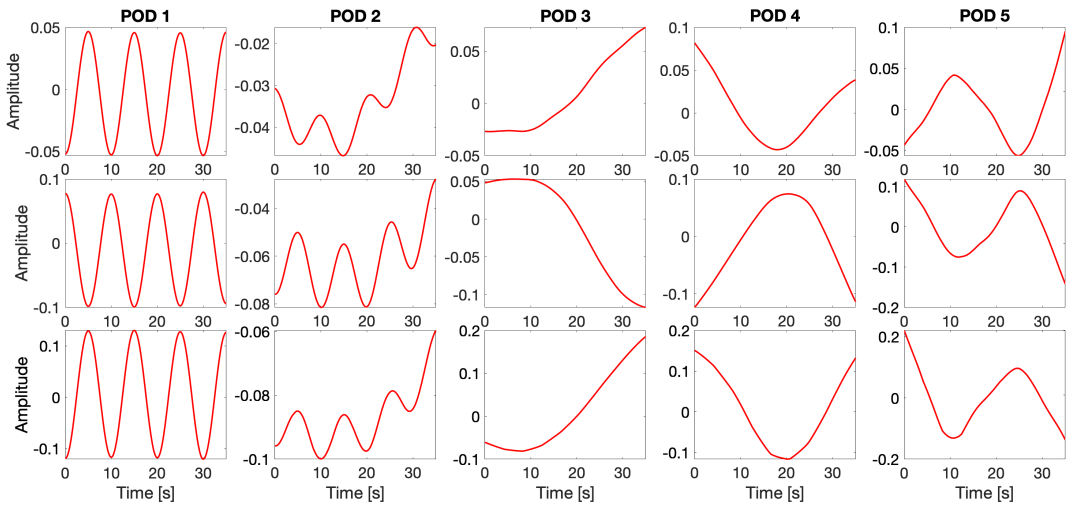

Figure 4.13: The time coefficients of the first five POD modes shown in Figure 4.10.

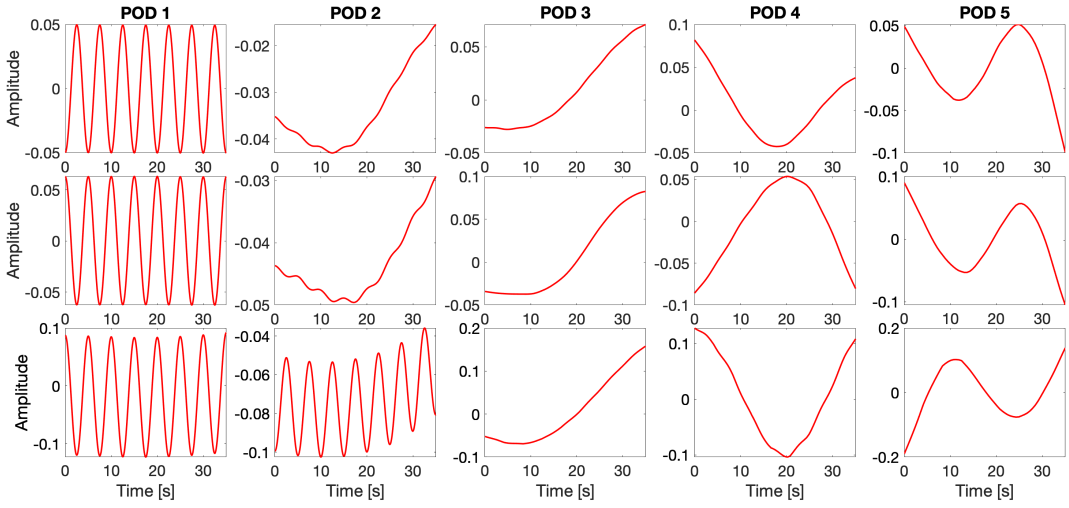

Figure 4.14: The time coefficients of the first five POD modes shown in Figure 4.11.

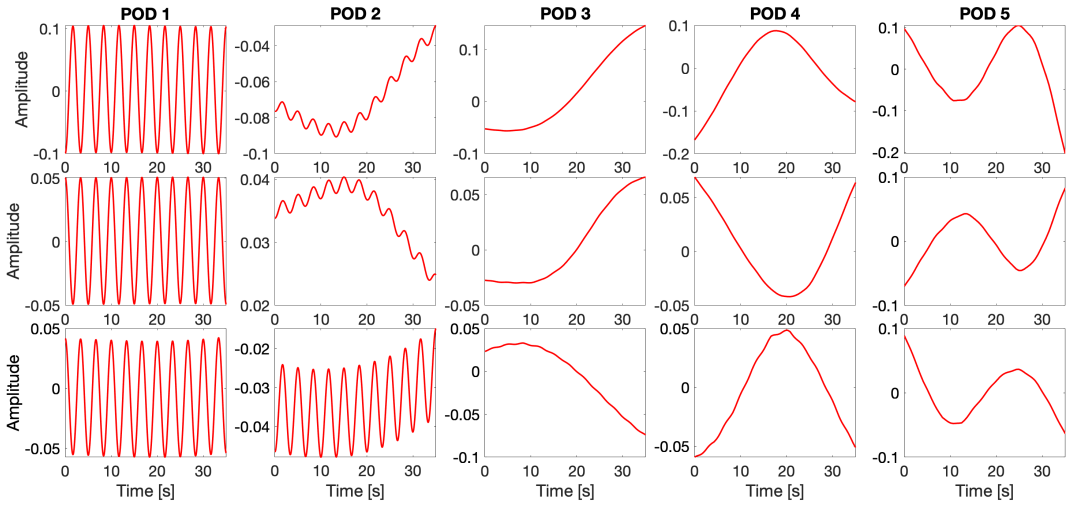

Figure 4.15: The time coefficients of the first five POD modes shown in Figure 4.12.

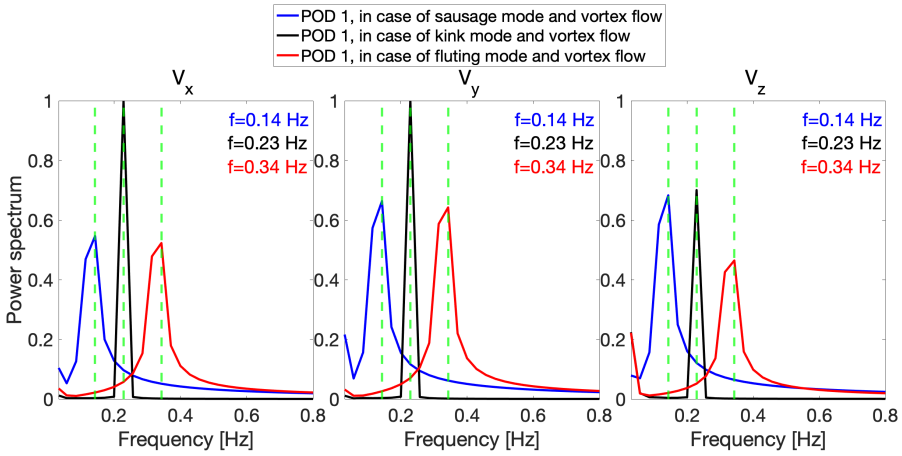

Figure 4.16: The Fast Fouerier Transform (FFT) of the time coefficients of POD 1 for each of the velocity components shown in Figures 4.10, 4.11 and 4.12 for each of the cases.

4.4 Conclusions

Vortices are ideal candidates to energy channeling from the dense solar photosphere to upper regions of the solar atmosphere, where it can be dissipated and converted into heat. This chapter discussed the possibility of wave propagation (as a mean for energy propagation) along vortex tubes.

Since such study cannot be confirmed observationally, the nature and properties of waves propagating along a vortex tube has been studied using the combination of numerical and synthetic data.

Inspired from the results presented in Chapter 3, it became clear that in the case of vortex tubes we have to distinguish between local and global waves. In the case of local waves only a limited portion of the vortex surface oscillate. The nature of these waves cannot be elucidated as we do not have enough information about the variation of plasma parameters inside the vortex. The periodicity of waves has been analysed by means of the POD decomposition. Our investigation reports on the existence of local waves with frequencies in the range of tens of mHz.

In order to analyse the morphology of global waves propagating along vortex tubes, first we created a synthetic dataset containing the properties of fast waves with different radial order (sausage, kink and fluting modes). Then, using the pattern of rotation derived from MuRAM numerical simulation of vortices presented in Chapter 3 we have imposed a vortex motion on the synthetically generated flux tube and investigated the morphology of global waves. The mode decomposition was accomplished using the same POD method, which proved to be a very reliable tool. The results show that the coupling between global waves and vortical motion did not generate new waves, the result of this coupling are the same waves as used in constructing model, however the FFT anslysis showed that their frequency under shift.

The POD applied to our synthetic data also revelead that POD is not only successful in identifying periodic patterns (waves), but also motions with no specific periodicity. In particular, the POD 2 mode recovered the signature of the vortical flow.

CHAPTER 5
Conclusions

5.1 Overview of thesis

The present summarises the research I carried out in the field of vortex identification and study in the solar photosphere. In particular, my aim was to understand the nature of physical processes responsible for vortex dynamics, the interplay of various forces that drive the dynamics on the surface of vortices, as well as the signatures of waves that could propagate on vortices, which are here modelled as simple rotating magnetic flux tubes.

5.2 Summary of results

After introducing relevant solar physics concepts, I discussed and reviewed the techniques used to identify vortices. These techniques are well known in fluid mechyanics, however, very little has been done in the field of plasma physics. As such, the research presented in this Thesis constitutes probably one of the very first attempts to isolate and study vortices in the lower solar atmospheric plasma using a Lagrangian approach. The properties of waves propagating in structured solar plasmas has also been reviewed, with special discussion on the properties of guided dispersive waves under photospheric and coronal conditions,

Chapter 3 was devoted to the investigation of physical parameters on the

surface of vortices generated using in magnetoconvection simulations that correlate to the dynamics in the lower part of the solar atmosphere. In this study, Lagrangian analysis was used to identify the three-dimensional vortex structure, and the vortex boundaries were defined by isosurfaces of LAVD contours, as previously described by Haller et al. (2016).

We can observe that the surfaces of the chosen vortices vary in size while maintaining their original structure. The fluctuation of physical parameters on the surface of the investigated vortices exhibits a very complicated behaviour. In the case of vortices detailed in this research, global alterations do not occur for all physical parameters. It is obvious that the variation of density, pressure, and specific magnetic field components are changing globally (see Figures 3.6 and 3.9), but the general characteristic of investigated vortices is that physical parameters describing the state of the plasma and quantities describing dynamics and energetics have a much more local character, implying that changes occur locally (see, for example, the variation of temperature). The examination of the Poynting flux components (see Figure 3.14) demonstrates that the energy fluxes are predominantly present in the horizontal direction, as previously found by Silva et al. (2022).

The forces that drive plasma dynamics on vortex surfaces are very inhomogeneous (see Figure 3.13, for example). We predict that the rise in the vertical velocity component (v_z) is connected to the vertical net force balance. The pressure gradient always points upwards, whereas gravity always points downwards. As a consequence, although the pressure gradient seems to dominate over the z-component of the Lorentz force, the findings shown in Figure 3.12 indicate that variations in vertical velocity are really driven by the Lorentz force. Indeed, we see slowing and acceleration of vertical flow in locations where the Lorentz force increases downwards and upwards, respectively, for both the R_1 and L_1 vortices. The pressure gradient dominance is

predicted since we are examining the vortex border, i.e. the outermost area where vortical movements have the greatest influence on flow dynamics.

Our findings indicate that the Lagrangian vortices retrieved from magnetoconvection simulations do not rotate like a rigid body. This rotation will result in varying angular velocities at various heights in the vortex. A recent study by Silva et al. (2020) provides an examination of the angular velocity profiles as a function of radius for the vortices detected in the magnetoconvection numerical simulations.

In Chapter 4 we investigated the presence and signature of local and global waves propagating along solar vortex tubes. The morphology of waves was analysed using the Proper Orthogonal Decomposition (POD) method, which turned out to be very reliable for mode identification.

First, using the data collected in Chapter 3 we analysed the propagation of local waves, i.e. waves that propagate locally on the surface of vortices. Our investigation shows that the data contains periodic signals with frequency of about 0.09 Hz, however, we cannot specify what is the nature of waves as this would require a detailed knowledge of the plasma condition and dynamics inside the vortex.

Next we used synthetic data to analyse the modifications of global wave pattern along a vortex tube. Using the theoretical results in the case of a homogeneous magnetic cylinder under photopspheric conditions, we have simulated the pattern of three waves with various radial structures (MHD sausage, kink and fluting modes). Using the velocity profiles collected for numerically simulated vortices, we have superimposed these profiles on the theoretical flux tube. Our POD analysis showed that the resultant waves preserve the nature and morphology of the constituents waves, however, their frequency is Doppler shifted. In addition to the clearly oscillatory behaviour, our POD analysis was

also able to identify the non-oscillatory pattern of flows.

5.3 Future work

The research presented in this Thesis constitutes a novel approach to study the variation of physical properties and the dynamics of vortex tubes. Our results revealed many fundamental properties of these structures, however, we are far from the comprehensive understanding on the structure, the complex evolution, and role of vortices in the solar atmosphere.

That is why the research presented in this Thesis could be continued along the following directions:

- Results presented in Chapter 3 show that we are able to extract essential information about the complex dynamics of vortices in the solar photosphere from numerical simulations. These results can lead to the research question of whether it would be possible to compare such findings to the observational results. In general, it is conceivable to compare 3D vortex surfaces reconstructed from numerical simulations with their counterparts from high-resolution observations of the solar atmosphere, but currently this is not straightforward. The main difficulty of this task is related to the reconstruction of the horizontal velocity field from photospheric intensity observations. The available local correlation tracking (LCT; November and Simon, 1988), FLCT (Fisher and Welsch, 2008), the recently developed DeepVel deep neural network (Asensio Ramos et al., 2017) and Multi-Scale Deep Learning (Ishikawa et al., 2021) aim to recover components of the flow field that are perpendicular to the line-of-sight. These methodologies have a number of limitations which may lead to a not fully accurate interpretation of the real physical plasma flows (see references provided for more details). The second problem is

related to the data sets available for the analysis. The precise vortex spatial structure can be obtained from the magnetoconvection simulations (as in the present Thesis), but observations consists of only few horizontal slices (which correspond to the integral signatures of the spectral lines formed at different heights) that can be used for analysis. Therefore, 3D reconstructions of the vortex dynamics which are based on observational data sets may imply errors that would influence the obtained results. However, it is worth mentioning that even in this case it is possible to directly compare the temporal and spatial evolution of observable and numerically simulated vortex parameters, e.g. radial dependence of velocity or magnetic field strength by taking 2D horizontal slices. The research on this aspect can be continued by combining high resolution data, machine learning and local correlation techniques to adequately construct the realistic flow field. Research in the area is currently ongoing.

- The present research can be expanded on the theoretical side, as well. In solar physics, the theory of MHD wave modes propagating in cylindrical magnetic waveguides is extensively established and relatively well understood. However, the properties and observational characteristics of MHD modes in the presence of vortex flows are still not fully understood. It is likely that in these vortex tubes the frequency of waves degenerate and the individual frequency of waves are replaced by a continuous distribution of frequencies and the governing equations become singular. Chapter 4 provides an approximate understanding of how the MHD wave mode operates by including a basic rotating flow at the boundary of the flux tube (see Figures 4.7, 4.8 and 4.9). Even this simple vortex rotation can introduce dramatic changes in the morphology of waves, making them almost unrecognisable. Future studies will need to focus on deriving

the dispersion relation of MHD waves modes with vortex flows in order to acquire the characteristics of modes. It is obvious that the study of waves' characteristics in the presence of realistic 3D vortex flows would require numerical solutions. Only such model will allow the study the real properties of waves propagating in vortex tubes and their role in energy transport into the upper solar atmosphere.

Bibliography

Albidah, A., Brevis, W., Fedun, V., Ballai, I., Jess, D., Stangalini, M., Higham, J., and Verth, G. (2021). Proper orthogonal and dynamic mode decomposition of sunspot data. *Philosophical Transactions of the Royal Society A*, 379(2190):20200181.

Aljohani, Y., Fedun, V., Ballai, I., Silva, S. S., Shelyag, S., and Verth, G. (2022). New approach for analysing dynamical processes on the surface of photospheric vortex tubes. *arXiv preprint arXiv:2202.09332*.

Allshouse, M. R. and Peacock, T. (2015). Lagrangian based methods for coherent structure detection. *Chaos: An Interdisciplinary Journal of Nonlinear Science*, 25(9):097617.

Antolin, P. and Shibata, K. (2010). The Role Of Torsional Alfvén Waves in Coronal Heating. *Astrophys. J.*, 712(1):494–510.

Arregui, I., Andries, J., Van Doorsselaere, T., Goossens, M., and Poedts, S. (2007). Mhd seismology of coronal loops using the period and damping of quasi-mode kink oscillations. *Astronomy & Astrophysics*, 463(1):333–338.

Arregui, I., Van Doorsselaere, T., Andries, J., Goossens, M., and Kimpe, D. (2005). Resonantly damped fast mhd kink modes in longitudinally stratified tubes with thick non-uniform transitional layers. *Astronomy & Astrophysics*, 441(1):361–370.

Aschwanden, M. (2006). *Physics of the solar corona: an introduction with problems and solutions*. Springer Science & Business Media.

Aschwanden, M. J., Fletcher, L., Schrijver, C. J., and Alexander, D. (1999). Coronal loop oscillations observed with the transition region and coronal explorer. *The Astrophysical Journal*, 520(2):880.

Asensio Ramos, A., Requerey, I. S., and Vitas, N. (2017). DeepVel: Deep learning for the estimation of horizontal velocities at the solar surface. *Astron. Astrophys.*, 604:A11.

Battaglia, A. F., Canivete Cuissa, J. R., Calvo, F., Bossart, A. A., and Steiner, O. (2021a). The Alfvénic nature of chromospheric swirls. *Astron. Astrophys.*, 649:A121.

Battaglia, A. F., Canivete Cuissa, J. R., Calvo, F., Bossart, A. A., and Steiner, O. (2021b). The Alfvénic nature of chromospheric swirls. *Astron. Astrophys.*, 649:A121.

Beeck, B., Collet, R., Steffen, M., Asplund, M., Cameron, R. H., Freytag, B., Hayek, W., Ludwig, H. G., and Schüssler, M. (2012). Simulations of the solar near-surface layers with the CO5BOLD, MURaM, and Stagger codes. *Astron. Astrophys.*, 539:A121.

Berry, M., Magstadt, A., and Glauser, M. (2017). Application of pod on time-resolved schlieren in supersonic multi-stream rectangular jets. *Physics of Fluids*, 29(2):020706.

Bonet, J. A., Márquez, I., Sánchez Almeida, J., Cabello, I., and Domingo, V. (2008). Convectively Driven Vortex Flows in the Sun. *Astrophys. J. Lett.*, 687(2):L131.

Bonet, J. A., Márquez, I., Sánchez Almeida, J., Palacios, J., Martínez Pillet, V., Solanki, S. K., del Toro Iniesta, J. C., Domingo, V., Berkefeld, T., Schmidt, W., Gandorfer, A., Barthol, P., and Knölker, M. (2010). SUNRISE/IMaX Observations of Convectively Driven Vortex Flows in the Sun. *Astrophys. J. Lett.*, 723(2):L139–L143.

Brandt, P. N., Scharmert, G. B., Ferguson, S., Shine, R. A., Tarbell, T. D., and Title, A. M. (1988). Vortex flow in the solar photosphere. *Nature*, 335:238–240.

Cameron, R., Schüssler, M., Vögler, A., and Zakharov, V. (2007). Radiative magnetohydrodynamic simulations of solar pores. *Astron. Astrophys.*, 474(1):261–272.

Canivete Cuissa, J. R. and Steiner, O. (2020). Vortices evolution in the solar atmosphere. A dynamical equation for the swirling strength. *Astron. Astrophys.*, 639:A118.

Chakraborty, P., Balachandar, S., and Adrian, R. J. (2005). On the relationships between local vortex identification schemes. *Journal of fluid mechanics*, 535:189–214.

Cheung, M. C. M., Schüssler, M., and Moreno-Insertis, F. (2007). Magnetic flux emergence in granular convection: radiative MHD simulations and observational signatures. *Astron. Astrophys.*, 467(2):703–719.

Chian, A. C.-L., Silva, S. S. A., Rempel, E. L., Gošić, M., Bellot Rubio, L. R., Kusano, K., Miranda, R. A., and Requerey, I. S. (2019). Supergranular turbulence in the quiet Sun: Lagrangian coherent structures. *Monthly Notices of the Royal Astronomical Society*, 488(3):3076–3088.

Chian, A. C.-L., Silva, S. S. A., Rempel, E. L., Rubio, L. R. B., Gošić, M., Kusano, K., and Park, S.-H. (2020). Lagrangian chaotic saddles and objective vortices in solar plasmas. *Phys. Rev. E*, 102:060201.

Chong, M. S., Perry, A. E., and Cantwell, B. J. (1990). A general classification of three-dimensional flow fields. *Physics of Fluids A*, 2(5):765–777.

Cowling, T. G. (1976). *Magnetohydrodynamics*.

Cowling, T. G. (1976). Magnetohydrodynamics.

Cram, L. and Wilson, P. (1975). Hydromagnetic waves in structured magnetic fields. *Solar Physics*, 41(2):313–327.

De Pontieu, B., Hansteen, V., van der Voort, L. R., van Noort, M., and Carlsson, M. (2007). High-resolution observations and modeling of dynamic fibrils. *The Astrophysical Journal*, 655(1):624.

Eckart, C. and Young, G. (1936). The approximation of one matrix by another of lower rank. *Psychometrika*, 1(3):211–218.

Edwin, P. and Roberts, B. (1983). Wave propagation in a magnetic cylinder. *Solar Physics*, 88(1-2):179–191.

Erdélyi, R. and Ballai, I. (2007). Heating of the solar and stellar coronae: a review. *Astronomische Nachrichten: Astronomical Notes*, 328(8):726–733.

Erdélyi, R. and Fedun, V. (2007). Are There Alfvén Waves in the Solar Atmosphere? *Science*, 318(5856):1572.

Farazmand, M. and Haller, G. (2016). Polar rotation angle identifies elliptic islands in unsteady dynamical systems. *Physica D: Nonlinear Phenomena*, 315:1–12.

Fedun, V., Shelyag, S., Verth, G., Mathioudakis, M., and Erdélyi, R. (2011). Mhd waves generated by high-frequency photospheric vortex motions. In *Annales Geophysicae*, volume 29, pages 1029–1035. Copernicus GmbH.

Fedun, V. N., Yukhimuk, A. K., and Voitsekhovskaya, A. D. (2004). The transformation of MHD Alfvén waves in space plasma. *Journal of Plasma Physics*, 70(6):699–707.

Fisher, G. H. and Welsch, B. T. (2008). FLCT: A Fast, Efficient Method for Performing Local Correlation Tracking. In Howe, R., Komm, R. W., Balasubramaniam, K. S., and Petrie, G. J. D., editors, *Subsurface and Atmospheric Influences on Solar Activity*, volume 383 of *Astronomical Society of the Pacific Conference Series*, page 373.

Foukal, P. (1971). Morphological relationships in the chromospheric hα fine structure. *Solar Physics*, 19(1):59–71.

Giagkiozis, I., Fedun, V., Scullion, E., Jess, D. B., and Verth, G. (2018). Vortex Flows in the Solar Atmosphere: Automated Identification and Statistical Analysis. *Astrophys. J.*, 869(2):169.

Graftieaux, L., Michard, M., and Grosjean, N. (2001). Combining PIV, POD and vortex identification algorithms for the study of unsteady turbulent swirling flows. *Measurement Science and Technology*, 12(9):1422–1429.

Günther, T., Schulze, M., and Theisel, H. (2015). Rotation invariant vortices for flow visualization. *IEEE transactions on visualization and computer graphics*, 22(1):817–826.

Gurtin, M. E. (1982). *An introduction to continuum mechanics*. Academic press.

Günther, T. and Theisel, H. (2018). The state of the art in vortex extraction. *Computer Graphics Forum*, 37(6):149–173.

Haller, G. (2001). Distinguished material surfaces and coherent structures in three-dimensional fluid flows. *Physica D: Nonlinear Phenomena*, 149(4):248–277.

Haller, G. (2005). An objective definition of a vortex. *Journal of Fluid Mechanics*, 525:1–26.

Haller, G. (2011). A variational theory of hyperbolic lagrangian coherent structures. *Physica D: Nonlinear Phenomena*, 240(7):574–598.

Haller, G. (2015). Lagrangian coherent structures. *Annual Review of Fluid Mechanics*, 47:137–162.

Haller, G., Hadjighasem, A., Farazmand, M., and Huhn, F. (2016). Defining coherent vortices objectively from the vorticity. *Journal of Fluid Mechanics*, 795:136–173.

Hart, A. B. (1956). Motions in the Sun at the photospheric level. VI. Large-scale motions in the equatorial region. *Mon. Not. Roy. Astron. Soc.*, 116:38.

Hathaway, D., Beck, J., Han, S., and Raymond, J. (2002). Radial flows in supergranules. *Solar Physics*, 205(1):25–38.

Higham, J., Brevis, W., Keylock, C., and Safarzadeh, A. (2017). Using modal decompositions to explain the sudden expansion of the mixing layer in the wake of a groyne in a shallow flow. *Advances in Water Resources*, 107:451–459.

Higham, J., Shahnam, M., and Vaidheeswaran, A. (2020). Using a proper orthogonal decomposition to elucidate features in granular flows. *Granular Matter*, 22(4):1–13.

Higham, J., Vaidheeswaran, A., Brevis, W., Nicolleau, F., and Marlow, J. (2021). Modification of modal characteristics in wakes of square cylinders with multi-scale porosity. *Physics of Fluids*, 33(4):045117.

Holmén, V. (2012). Methods for vortex identification. *Master's Theses in Mathematical Sciences*.

Hunt, J. C. R., Wray, A. A., and Moin, P. (1988). Eddies, streams, and convergence zones in turbulent flows. In *Studying Turbulence Using Numerical Simulation Databases, 2*, pages 193–208.

Hussain, A. F. (1986). Coherent structures and turbulence. *Journal of Fluid Mechanics*, 173:303–356.

Ishikawa, R. T., Nakata, M., Katsukawa, Y., Masada, Y., and Riethmüller, T. L. (2021). Multi-Scale Deep Learning for Estimating Horizontal Velocity Fields on the Solar Surface. *arXiv e-prints*, page arXiv:2111.12518.

Jeong, J. and Hussain, F. (1995). On the identification of a vortex. *Journal of fluid mechanics*, 285:69–94.

Khomenko, E. V., Shelyag, S., Solanki, S. K., and Vögler, A. (2005). Stokes diagnostics of simulations of magnetoconvection of mixed-polarity quiet-Sun regions. *Astron. Astrophys.*, 442(3):1059–1078.

Khomenko, V. M. (2005). Carbon oxides in cordierite channels: Determination of CO2 isotopic species and CO by single crystal IR spectroscopy. *American Mineralogist*, 90(11-12):1913–1917.

Kida, S. and Miura, H. (1998). Identification and analysis of vortical structures. *European Journal of Mechanics-B/Fluids*, 17(4):471–488.

Kitiashvili, I. N., Kosovichev, A. G., Lele, S. K., Mansour, N. N., and Wray, A. A. (2013). Ubiquitous solar eruptions driven by magnetized vortex tubes. *ApJ*, 770(1):37.

Kitiashvili, I. N., Kosovichev, A. G., Mansour, N. N., and Wray, A. A. (2012). DYNAMICS OF MAGNETIZED VORTEX TUBES IN THE SOLAR CHROMOSPHERE. *The Astrophysical Journal*, 751(1):L21.

Kuperus, M., Ionson, J. A., and Spicer, D. S. (1981). On the theory of coronal heating mechanisms. *Annual Review of Astronomy and Astrophysics*, 19(1):7–40.

Lang, K. R. (2000). *The Sun from space*, volume 1. Springer.

Leighton, R. B., Noyes, R. W., and Simon, G. W. (1962). Velocity Fields in the Solar Atmosphere. I. Preliminary Report. *Astrophys. J.*, 135:474.

Lighthill, M. J. (1960). Studies on magneto-hydrodynamic waves and other anisotropic wave motions. *Philosophical Transactions of the Royal Society of London. Series A, Mathematical and Physical Sciences*, 252(1014):397–430.

Lumley, J. L. (1967). The structure of inhomogeneous turbulent flows. *Atmospheric turbulence and radio wave propagation.*

Martínez-Sykora, J., De Pontieu, B., Hansteen, V., and Carlsson, M. (2015). The role of partial ionization effects in the chromosphere. *Philosophical Transactions of the Royal Society of London Series A*, 373(2042):20140268–20140268.

McWilliams, J. C. (1984). The emergence of isolated coherent vortices in turbulent flow. *Journal of Fluid Mechanics*, 146:21–43.

Moll, R., Cameron, R. H., and Schüssler, M. (2012). Vortices, shocks, and heating in the solar photosphere: effect of a magnetic field. *Astron. Astrophys.*, 541:A68.

Morton, R. J., Verth, G., Jess, D. B., Kuridze, D., Ruderman, M. S., Mathioudakis, M., and Erdélyi, R. (2012). Observations of ubiquitous compressive waves in the sun's chromosphere. *Nature Communications*, 3(1):1–8.

Murray, N. E. and Ukeiley, L. S. (2007). An application of gappy pod. *Experiments in Fluids*, 42(1):79–91.

Nakariakov, V., Ofman, L., Deluca, E., Roberts, B., and Davila, J. (1999). Trace observation of damped coronal loop oscillations: Implications for coronal heating. *Science*, 285(5429):862–864.

Nelson, C. J., Shelyag, S., Mathioudakis, M., Doyle, J. G., Madjarska, M. S., Uitenbroek, H., and Erdélyi, R. (2013). Ellerman Bombs—Evidence for Magnetic Reconnection in the Lower Solar Atmosphere. *Astrophys. J.*, 779(2):125.

Nordlund, Å. (1985). Solar convection. *Solar Physics*, 100(1):209–235.

November, L. J. and Simon, G. W. (1988). Precise Proper-Motion Measurement of Solar Granulation. *Astrophys. J.*, 333:427.

Parker, E. N. (1979). Sunspots and the physics of magnetic flux tubes. VIII. Overstability in a magnetic field in a downdraft. *Astrophys. J.*, 233(3):1005–1015.

Parnell, C. E. and De Moortel, I. (2012). A contemporary view of coronal heating. *Philosophical Transactions of the Royal Society A: Mathematical, Physical and Engineering Sciences*, 370(1970):3217–3240.

Pascoe, D. J. (2014). Numerical simulations for mhd coronal seismology. *Research in Astronomy and Astrophysics*, 14(7):805.

Peacock, T. and Dabiri, J. (2010). Introduction to focus issue: Lagrangian coherent structures.

Peacock, T., Froyland, G., and Haller, G. (2015). Introduction to focus issue: Objective detection of coherent structures.

Perry, A. E. and Chong, M. S. (1987). A description of eddying motions and flow patterns using critical-point concepts. *Annual Review of Fluid Mechanics*, 19(1):125–155.

Pietarila, A., Hirzberger, J., Zakharov, V., and Solanki, S. (2009). Bright fibrils in ca ii k. *Astronomy & Astrophysics*, 502(2):647–660.

Post, F. H., Vrolijk, B., Hauser, H., Laramee, R. S., and Doleisch, H. (2003). The state of the art in flow visualisation: Feature extraction and tracking. In *Computer Graphics Forum*, volume 22, pages 775–792. Wiley Online Library.

Priest, E. (2014). *Magnetohydrodynamics of the Sun*. Cambridge University Press.

Rappazzo, A. F., Velli, M., Dahlburg, R. B., and Einaudi, G. (2019). Magnetic Field Line Twisting by Photospheric Vortices: Energy Storage and Release. *Astrophys. J.*, 883(2):148.

Rempel, M., Schüssler, M., Cameron, R. H., and Knölker, M. (2009). Penumbral Structure and Outflows in Simulated Sunspots. *Science*, 325(5937):171.

Requerey, I. S., Cobo, B. R., Gošić, M., and Bellot Rubio, L. R. (2018). Persistent magnetic vortex flow at a supergranular vertex. *Astron. Astrophys.*, 610:A84.

Rieutord, M. and Rincon, F. (2010). The sun's supergranulation. *Living Reviews in Solar Physics*, 7(1):1–82.

Rieutord, M., Roudier, T., Rincon, F., Malherbe, J.-M., Meunier, N., Berger, T., and Frank, Z. (2010). On the power spectrum of solar surface flows. *Astronomy & Astrophysics*, 512:A4.

Roberts, B. (1981a). Wave Propagation in a Magnetically Structured Atmosphere - Part One - Surface Waves at a Magnetic Interface. *Solar Phys.*, 69(1):27–38.

Roberts, B. (1981b). Wave Propagation in a Magnetically Structured Atmosphere - Part Two - Waves in a Magnetic Slab. *Solar Phys.*, 69(1):39–56.

Roberts, B. and Webb, A. (1978). Vertical motions in an intense magnetic flux tube. *Solar Physics*, 56(1):5–35.

Roberts, B. and Webb, A. (1979). Vertical motions in an intense magnetic flux tube. *Solar Physics*, 64(1):77–92.

Schüssler, M., Shelyag, S., Berdyugina, S., Vögler, A., and Solanki, S. K. (2003). Why Solar Magnetic Flux Concentrations Are Bright in Molecular Bands. *Astrophys. J. Lett.*, 597(2):L173–L176.

Shadden, S. C. (2011). Lagrangian coherent structures. *Transport and Mixing in Laminar Flows: From Microfluidics to Oceanic Currents*, pages 59–89.

Shelyag, S., Cally, P. S., Reid, A., and Mathioudakis, M. (2013). Alfvén Waves in Simulations of Solar Photospheric Vortices. *Astrophys. J. Lett.*, 776(1):L4.

Shelyag, S., Fedun, V., Keenan, F. P., Erdélyi, R., and Mathioudakis, M. (2011a). Photospheric magnetic vortex structures. *Annales Geophysicae*, 29(5):883–887.

Shelyag, S., Keys, P., Mathioudakis, M., and Keenan, F. P. (2011b). Vorticity in the solar photosphere. *Astron. Astrophys.*, 526:A5.

Shelyag, S., Litvinenko, Y. E., Fedun, V., Verth, G., González-Avilés, J. J., and Guzmán, F. S. (2018). Flows and magnetic field structures in reconnection regions of simulations of the solar atmosphere: Do flux pile-up models work? *Astron. Astrophys.*, 620:A159.

Shelyag, S., Mathioudakis, M., and Keenan, F. P. (2012). Mechanisms for MHD Poynting Flux Generation in Simulations of Solar Photospheric Magnetoconvection. *Astrophys. J. Lett.*, 753(1):L22.

Shelyag, S., Schüssler, M., Solanki, S. K., Berdyugina, S. V., and Vögler, A. (2004). G-band spectral synthesis and diagnostics of simulated solar magneto-convection. *Astron. Astrophys.*, 427:335–343.

Shelyag, S., Schüssler, M., Solanki, S. K., and Vögler, A. (2007). Stokes diagnostics of simulated solar magneto-convection. *Astron. Astrophys.*, 469(2):731–747.

Shetye, J., Verwichte, E., Stangalini, M., Judge, P. G., Doyle, J. G., Arber, T., Scullion, E., and Wedemeyer, S. (2019). Multiwavelength High-resolution Observations of Chromospheric Swirls in the Quiet Sun. *Astrophys. J.*, 881(1):83.

Silva, S. S. A., Fedun, V., Verth, G., Rempel, E. L., and Shelyag, S. (2020). Solar Vortex Tubes: Vortex Dynamics in the Solar Atmosphere. *Astrophys. J.*, 898(2):137.

Silva, S. S. A., Murabito, M., Jafarzadeh, S., Stangliani, M., Verth, G., Ballai, I., and Fedun, V. (2022). The importance of horizontal Poynting flux in the solar photosphere. *Astrophys. J.*, In press.

Silva, S. S. A., Rempel, E. L., Pinheiro Gomes, T. F., Requerey, I. S., and Chian, A. C. L. (2018). Objective Lagrangian Vortex Detection in the Solar Photosphere. *Astrophys. J. Lett.*, 863(1):L2.

Silva, S. S. A., Verth, G., Rempel, E. L., Shelyag, S., Schiavo, L. A. C. A., and Fedun, V. (2021). Solar Vortex Tubes. II. On the Origin of Magnetic Vortices. *Astrophys. J.*, 915(1):24.

Spiegel, E. and Zahn, J.-P. (1992). The solar tachocline. *Astronomy and Astrophysics*, 265:106–114.

Spruit, H. C. (1981). Motion of magnetic flux tubes in the solar convection zone and chromosphere. *Astronomy and Astrophysics*, 98:155–160.

Spruit, H. C. (1982). Propagation Speeds and Acoustic Damping of Waves in Magnetic Flux Tubes. *Solar Phys.*, 75(1-2):3–17.

Taroyan, Y. (2008). Alfvén Instability in a Compressible Flow. , 101(24):245001.

Taroyan, Y. and Erdélyi, R. (2009). Heating Diagnostics with MHD Waves. *Space Sci. Rev.*, 149(1-4):229–254.

Truesdell, C. and Noll, W. (2004). The non-linear field theories of mechanics. In *The non-linear field theories of mechanics*, pages 1–579. Springer.

Tziotziou, K., Tsiropoula, G., and Kontogiannis, I. (2019). A persistent quiet-Sun small-scale tornado. II. Oscillations. *Astron. Astrophys.*, 623:A160.

Tziotziou, K., Tsiropoula, G., Kontogiannis, I., Scullion, E., and Doyle, J. G. (2018). A persistent quiet-Sun small-scale tornado. I. Characteristics and dynamics. *Astron. Astrophys.*, 618:A51.

Vernazza, J. E., Avrett, E. H., and Loeser, R. (1981). Structure of the solar chromosphere. iii-models of the euv brightness components of the quiet-sun. *The Astrophysical Journal Supplement Series*, 45:635–725.

Vögler, A., Shelyag, S., Schüssler, M., Cattaneo, F., Emonet, T., and Linde, T. (2005). Simulations of magneto-convection in the solar photosphere. Equations, methods, and results of the MURaM code. *Astron. Astrophys.*, 429:335–351.

Webb, G. (1980). Existence and asymptotic behavior for a strongly damped nonlinear wave equation. *Canadian Journal of Mathematics*, 32(3):631–643.

Wedemeyer, S., Bastian, T., Brajša, R., Hudson, H., Fleishman, G., Loukitcheva, M., Fleck, B., Kontar, E. P., De Pontieu, B., Yagoubov, P., et al. (2016). Solar science with the atacama large millimeter/submillimeter array—a new view of our sun. *Space Science Reviews*, 200(1-4):1–73.

Wedemeyer, S. and Steiner, O. (2014). On the plasma flow inside magnetic tornadoes on the sun. *Publications of the Astronomical Society of Japan*, 66(SP1).

Wedemeyer, S. and Steiner, O. (2014). On the plasma flow inside magnetic tornadoes on the Sun. *Pub. Astron. Soc. Japan*, 66:S10.

Wedemeyer-Böhm, S., Lagg, A., and Nordlund, Å. (2009). Coupling from the photosphere to the chromosphere and the corona. *Space Science Reviews*, 144(1-4):317–350.

Wedemeyer-Böhm, S., Scullion, E., Steiner, O., Rouppe van der Voort, L., de La Cruz Rodriguez, J., Fedun, V., and Erdélyi, R. (2012). Magnetic tornadoes as energy channels into the solar corona. *Nature*, 486(7404):505–508.

Wedemeyer-Böhm, S., Scullion, E., Steiner, O., van der Voort, L. R., de La Cruz Rodriguez, J., Fedun, V., and Erdélyi, R. (2012). Magnetic tornadoes as energy channels into the solar corona. *Nature*, 486(7404):505–508.

Wedemeyer-Böhm, S. and van der Voort, L. R. (2009). Small-scale swirl events in the quiet sun chromosphere. *Astronomy & Astrophysics*, 507(1):L9–L12.

Wentzel, D. (1979). Hydromagnetic surface waves on cylindrical fluxtubes. *Astronomy and Astrophysics*, 76:20–23.

Wilson, P. R. (1979). Wave propagation in a magnetic flux sheath in the presence of a velocity field. *Astrophys. J.*, 230:194–203.

Yadav, N., Cameron, R. H., and Solanki, S. K. (2020). Simulations show that vortex flows could heat the chromosphere in solar plage. *The Astrophysical Journal Letters*, 894(2):L17.

Yadav, N., Cameron, R. H., and Solanki, S. K. (2020). Simulations Show that Vortex Flows Could Heat the Chromosphere in Solar Plage. *Astrophys. J. Lett.*, 894(2):L17.

Yadav, N., Cameron, R. H., and Solanki, S. K. (2021). Vortex flow properties in simulations of solar plage region: Evidence for their role in chromospheric heating. *Astronomy & Astrophysics*, 645:A3.

Yadav, N., Cameron, R. H., and Solanki, S. K. (2021). Vortex flow properties in simulations of solar plage region: Evidence for their role in chromospheric heating. *Astron. Astrophys.*, 645:A3.

Zhou, J., Adrian, R. J., Balachandar, S., and Kendall, T. M. (1999). Mechanisms for generating coherent packets of hairpin vortices in channel flow. *Journal of Fluid Mechanics*, 387(1):353–396.

Zirker, J. B. (1993). Coronal heating. *Solar physics*, 148(1):43–60.